Lidar Signal-to-Noise Ratio Improvements:

Considerations and Techniques

By

YASSER Y. HASSEBO

A dissertation submitted to the Graduate Faculty in Engineering
in partial fulfillment of the requirements for the degree of

DOCTOR OF PHILOSOPHY

THE CITY UNIVERSITY OF NEW YORK

2007

UMI Number: 3283198

Copyright 2007 by
Hassebo, Yasser Y.

All rights reserved.

UMI®

UMI Microform 3283198
Copyright 2007 by ProQuest Information and Learning Company.
All rights reserved. This microform edition is protected against
unauthorized copying under Title 17, United States Code.

ProQuest Information and Learning Company
300 North Zeeb Road
P.O. Box 1346
Ann Arbor, MI 48106-1346

© 2007
YASSER Y. HASSEBO
All Rights Reserved

Lidar Signal-to-Noise Ratio Improvements: Considerations and Techniques

A dissertation

By

YASSER Y. HASSEBO

Submitted to the Graduate Faculty in Engineering in partial fulfillment of the requirements for the degree of Doctor of Philosophy

This manuscript has been read and accepted by the Graduate Faculty in Engineering in satisfaction of the requirements for the degree of Doctor of Philosophy.

Approved as to style and content by:

_____Date: 04/24/2007
Dr. Samir Ahmed
Herbert Kayser Professor of EE, CCNY
(Chair of Examining Committee)

_____Date: 04/27/2007
Dean Mumtaz K. Kassir
Executive Officer

Dr. Barry Gross
Professor, Electrical Engineering Department, CUNY

Dr. Fred Moshary
Professor, Deputy Chair of Electrical Engineering Department, CUNY

Dr. Mohamed Ali
Professor, Electrical Engineering Department, CUNY

Dr. Jacek Chowdhary
Professor, Columbia University
NASA Goddard Institute for Space Studies

2007

Major Subject: Electrical Engineering

The City University of New York

ABSTRACT

Lidar Signal-to-Noise Ratio Improvements: Considerations and Techniques

(2007)

Yasser Youssef Hassebo

B.Sc. of Electrical Engineering, Menoufia University, Egypt
M.E. of Electrical Engineering, the City College of the City University of New York
M.Phil of Engineering, the City University of New York

Chair of Advisory Committee: Prof. Samir Ahmed
Herbert Kayser Professor of Electrical Engineering, CUNY

ABSTRACT

The primary objective of this study is to improve lidar signal-to-noise ratio (SNR) and hence extend attainable lidar ranges through reduction of the sky background noise (BGP), which dominates other sources of noise in daytime operations. This is particularly important for Raman lidar techniques where the Raman backscattered signal of interest is relatively weak compared with the elastic backscatter lidars.

Two approaches for reduction of sky background noise are considered:

1. Improvements in lidar SNR by optimization of the design of the lidar receiver were examined by a series of simulations. This part of the research concentrated on biaxial lidar systems, where overlap between laser beam and receiver field of view (FOV) is an important aspect of noise considerations. The first optimized design evolved is a wedge shaped aperture. While this design has the virtue of greatly reducing background light, it is difficult to implement practically, requiring both changes in area and position with lidar range. A second more practical approach,

which preserves some of the advantages of the wedge design, was also evolved. This uses a smaller area circular aperture optimally located in the image plane for desired ranges. Simulated numerical results for a biaxial lidar have shown that the best receiver parameters selection is one using a small circular aperture (field stop) with a small telescope focal length *f*, to ensure the minimum FOV that accepts all return signals over the entire lidar range while at the same time minimizing detected BGP and hence maximizing lidar SNR and attainable lidar ranges. The improvement in lidar SNR was up to 18 %.

2. A polarization selection technique was implemented to reduce sky background signal for linearly polarized monostatic elastic backscatter lidar measurements. The technique takes advantage of naturally occurring polarization properties in scattered sky light, and then ensures that both the lidar transmitter and receiver track and minimize detected sky background noise while maintaining maximum lidar signal throughput. Measurements, carried at 532 nm, show as much as a factor of $\sqrt{10}$ improvement in SNR and the attainable lidar range up to 34% over conventional un-polarized schemes. For vertically pointing lidars, the largest improvements are limited to the early morning and late afternoon hours, while for lidars scanning azimuthally and in elevation at angles other than vertical, significant improvements are achievable over more extended time periods. Observed changes in SNR improvements were also related to relative humidity and modification of underlying aerosol microphysics.

A second, distinct objective of this research was to utilize multiwavelength lidar techniques to separate plume and cloud particles. Choice of the study location and time for this work was driven mainly by the availability of satellite data collected by NASA

INTEX-NA and NOAA NEAQS experiment over New York City on July 21, 2004 in support of MODIS imagery. The lidar results identify smoke plumes over New York City and validate the plume source origin location using NOAA-HYSPLIT back trajectory analysis. Surface measurements, at the time, from in-situ particle counters are presented and show no enhanced PM2.5 loading. This result is supported by lidar measurements, which confirm that nearly all of the aerosol plumes are located above the normal aerosol boundary layer showing that satellite measurements are often incomplete and are not sufficient for assessing surface air quality.

DEDICATIONS

This dissertation is dedicated to my beloved

Father and mother

Brothers and sister

Whom have been supporting me in the entire journey to the end

In grateful appreciation

And

To my pretty daughter, Maryam

A lovely girl with hopefully, lofty goals, and to her mother

ACKNOWLEDGEMENTS

I greatly would like to express my sincere appreciation and thankful to almighty God, Allah

Then, secondly, I am grateful to my mentor, Professor Samir Ahmed (Director of the Optical Remote Sensing Laboratory at CCNY), for his supervision and support during my graduate studies and research at The City University of New York. His creativity and distinctive aspects of thoughts kept me focus on the whole picture and inspired me to remarkable topics in research. I enjoyed and learned much from the interesting technical discussions I had with him, which I believe will definitely benefit me throughout my future. Thank you for your supervision on both the technical and the personal levels

As part of the Optical Remote Sensing Lab team, I would like to acknowledge help and guidance from Professors Gross and Moshary in many aspects of this work

My gratitude also to NOAA-CREST for supporting me as a member of NOAA family

I would like to thank and acknowledge my other examining committee members: Prof. Mohamed Ali (CCNY), and Dr. Jacek Chowadhry (NASA Goddard Institute for Space Studies/ Columbia University) for their time and useful comments on my research

Special appreciation is to my parents Youssef Hassebo and F. El-Hefnawy, my brothers Ayman, Hassan, and Ahmed and my sister Eman for their love and encouragement. I could not have completed this dissertation without them

This work was supported under contract from NOAA # NA17AE1625.

TABLE OF CONTENTS

Chapter **Page**

ABSTRACT ..... **iv**

DEDICATIONS ..... **vii**

ACKNOWLEDGEMENTS ..... **viii**

TABLE OF CONTENTS ..... **ix**

TABLE OF FIGURES ..... **xii**

LIST OF TABLES ..... **xvi**

NOMENCLATURE ..... **xvii**

ACRONYMS ..... **xx**

1 INTRODUCTION **1**

1.1 LIDAR BACKGROUND **1**
1.1.1 Lidar Historical Background **1**
1.1.2 What is a Lidar **2**
1.2 HOW DOES LIDAR WORK? **4**
1.3 LIDAR CLASSIFICATIONS **5**
1.3.1 Types of Lidar Returns **6**
1.3.1.1 Rayleigh Scattering Lidar: 6
1.3.1.2 Mie Backscatter Lidars 8
1.3.1.3 Raman (Inelastic Backscattering) Lidars: 9
1.3.1.4 DIfferential Absorption Lidar (DIAL): 10
1.3.1.5 Doppler Lidars 11
1.3.1.6 Resonance Fluorescence Lidars 12
1.3.2 Lidar Wavelengths **13**
1.3.2.1 Elastic Lidar: 13
1.3.2.2 Inelastic Backscattering Lidar: 16
1.3.2.3 Multiple Wavelength Lidar 18
1.3.2.4 Femto-second White Light Lidar: 19
1.3.3 Purposes of Lidar Measurements **20**
1.3.3.1 Aerosol Lidar: 20
1.3.3.2 Cloud Lidar: 22
1.3.3.3 Velocity Lidar: 25
1.3.4 Lidar Types Based on Platform **26**
1.3.4.1 Ground-based Lidar: 26
1.3.4.2 Air-borne Lidar 26
1.3.4.3 Space-based Lidar: 27
1.3.5 Lidar Configurations **27**
1.3.5.1 Monostatic Lidar 27
1.3.5.2 Monostatic Coaxial Lidar 28
1.3.5.3 Monostatic Biaxial Lidar 29
1.3.5.4 Bi-static Configuration 29

Chapter **Page**

2 THE RESEARCH OBJECTIVES 31

2.1 THESIS OBJECTIVES 31
2.2 BASIC LIDAR AND SYSTEM ASSUMPTIONS FOR THESIS WORK 34
2.3 THESIS OUTLINE 36

3 THE CUNY LIDARS AND LIDAR EQUATION 39

3.1 EXPERIMENTAL APPROACH: CUNY LIDARS SPECIFICATIONS 39
3.1.1 Stationary Rayleigh /Mie-Raman Lidar 40
3.1.2 Mobile Rayleigh -Mie Lidar 43
3.2 RETRIEVAL OF LIDAR RETURNS 46
3.2.1 Solving Lidar Equation (Retrieval Method) 49

4 LIDAR RECEIVER DESIGN PARAMETERS: IMPACTS AND SELECTION 56

4.1 GEOMETRIC FACTOR EFFECT IN LIDAR 57
4.1.1 Geometric Form Factor Definition 58
4.1.2 Procedures and Calculations 63
4.1.3 Results 64
1.1.3.1 Results without Corrections 64
1.1.3.2 Results with Corrections (New Position, Circular Apertures) 66
1.1.3.3 Results with Corrections (Wedge-like Shape Apertures) 68
4.1.4 Conclusion 69
4.2 THE HE IMPACT OF RECEIVER APERTURE DESIGN AND TELESCOPE PROPERTIES ON LIDAR SNR IMPROVEMENTS 71
4.2.1 Problem Description and Analysis 73
4.2.2 Results 76
4.2.3 Telescope Selection 78
4.2.4 Conclusions 81
4.3 DETECTORS NOISE CONSIDERATIONS 82
4.3.1 The photocathode SNR 86
4.3.2 The SNR for the PMT (anode current) 86
4.3.3 The SNR for the APD (Avalanche Photodiode) 87
4.3.4 Detectors Selection 87

5 POLARIZATION DISCRIMINATION TECHNIQUE TO MAXIMIZE LIDAR SIGNAL-TO-NOISE RATIO FOR DAYLIGHT OPERATIONS 89

5.1 INTRODUCTION 90
5.2 EXPERIMENTAL APPROACH AND SYSTEM GEOMETRY 93
5.3 RESULTS 96
5.3.1 Lidar data 96
5.4 SNR IMPROVEMENT WITH RESPECT TO SOLAR ZENITH ANGLE 101
5.5 EFFECT OF VARIABLE PRECIPITABLE WATER VAPOR ON SNR 103
5.6 DISCUSSION AND ANALYSIS 104
5.6.1 Symmetric data set 106
5.6.2 Asymmetric data set 108
5.7 SNR IMPROVEMENT AZIMUTHALLY DEPENDENCE 112

Chapter **Page**

5.8 MULTIPLE SCATTERING EFFECTS 117
5.8.1 Magnitude of SNR Improvement Factor 117
5.8.2 Polarization Plane Orientation and SNR Improvement 119
5.9 SCANNING LIDARS 121
5.10 CONCLUSIONS AND SUMMARY 122

6 LIDAR MEASURMENTS AT CCNY: SUPPORT OF THE NOAA-NEAQS AND NASA-INTEX-NA EXPERIMENTS 124

6.1 INTRODUCTION 124
6.2 RESULTS 128
6.3 HYSPLIT BACK-TRAJECTORIES 136
6.4 PM2.5 SURFACE MEASUREMENTS. 137
6.5 CONCLUSIONS 140

7 CONCLUSIONS 141

RECOMMENDED FUTURE WORK 144

Y. HASSEBO PUBLICATIONS, CONFERENCE PROCEEDINGS AND PRESENTATIONS 145

REFERENCES 147

VITA 153

TABLE OF FIGURES

Page

Figure 1.1 Essential elements of a lidar system.....2

Figure 1.2 CCNY lidar retrieval for $S_a(R)$ ration, June 30, 2004 14

Figure 1.3 New York City aerosol PBL, Aug 11, 2005 21

Figure 1.4 CCNY lidar data shows cloud base, thickness, and structure, Jan 25, 2006. 23

Figure 1.5 CCNY Lidar backscattering signals show thin cloud at 11km, Jan 10, 2006. 25

Figure 1.6 Field of view arrangements for lidar laser beam and detector optics.....28

Figure 3.1 Schematic diagram of the multi-wavelength Mie-Raman stationary lidar.....40

Figure 3.2 Licel data acquisition: 5 channels 42

Figure 3.3 Licel connections 42

Figure 3.4 CCNY schematic diagram of the multi-wavelength Mie lidar (mobile system).....43

Figure 3.5: Example of integrated optical depth, using Fernald method, as function of S_a.....55

Figure 4.1 Overlap area calculation.....62

Figure 4.2 Schematic diagram of elastic biaxial lidar 62

Figure 4.3 The monostatic biaxial lidar, schematic diagram shows laser beam, telescope, , and sounding trace images for ranges of R_{min}, R_{max} 64

Figure 4.4 The overlap area between circular aperture with radius of 1mm vs. the object images of range R_{min}= 10 m to R_{max}=50 km (a) Short range (10-500 m) images: No overlap (b) (500-800 m) range images: Just started to overlap at 800 m (c) Range (2-20 km): Partial collection (d) Range (20 – 50 km): Almost complete collection.....65

Figure 4.5 The GF of range R_{min}= 10 m to R_{max}=50 km, comparison between the original round aperture of 1mm radius at the origin and a new round aperture that accommodates the entire image. (a) Short range (10-500 m) (b) Range of (500-800 m).....66

Page

Figure 4.6 The GF of range R_{min}= 10 m to R_{max}=50 km, comparison between the original round aperture of 1mm radius at the origin and a new round one that accommodates the entire image. (a) Middle range (2-20 km) (b) High range of (20 – 50 km) 67

Figure 4.7 Optimal GF using new wedge-like shape apertures of various ranges, CCNY lidar 68

Figure 4.8 The monostatic biaxial lidar, schematic diagram shows laser beam, telescope, , and sounding trace images for ranges of R_{min}, R_{max} 74

Figure 4.9 Biaxial lidar: overlapping between effective FOV of receiver telescope (diameter of t_o) and laser beam (initial diameter L_o) and aperture diameter D_o.....74

Figure 4.10 Lidar images for range 500m-5km. The green images (images $_L$) for 4 m telescope focal length and the blue images (images $_S$) for telescope with 1.7m focal length. The commonplace aperture (D_o=2 mm) placed at the telescope focal point, D_L is a round aperture to accommodate (images $_L$) and D_S is a round aperture to accommodate (images $_S$).....77

Figure 4.11 Lidar images for range 5km-25km. The green images (images $_L$) for 4 m telescope focal length and the blue images (images $_S$) for telescope with 1.7m focal length. The commonplace aperture (D_o=2 mm) placed at the telescope focal point, D_L is a round aperture to accommodate (images $_L$) and D_S is a round aperture to accommodate (images $_S$). 77

Figure 4.12 The Photomultiplier Tube (PMT) schematic diagram (Hamamatsu).....83

Figure 4.13 Photomultiplier Tube (PMT) connection 83

Figure 5.1 Sky background suppression geometry for a vertical pointing lidar: θ_s is the solar zenith angle (equal to the scattering angle for this geometry) ϕ_s is the solar azimuth angle; and OAB is the solar scattering plane.....92

Figure 5.2 Schematic diagram of polarization experiment set up for elastic biaxial monostatic lidar (mobile lidar system).....95

Figure 5.3 Comparison of max P_b verses min P_b lidar signals at 6:29 PM 96

Figure 5.4 Comparison of max max P_b (N_{Max}) verses min P_b (N_{Min}) lidar signals at 3 PM (EST) on 07 October 2004: Range 35 km, Lidar signal in linear scale 97

Page

Figure 5.5 Comparison of max P_b (N_{Max}) verses min P_b (N_{Min}) lidar signals at noon (EST) on 07 October 2004: Range 35 km, Lidar signal in linear scale, two signals are overlapped.....98

Figure 5.6 Comparison of experimental return signals at 6:29 PM, 3 PM and noon 99

Figure 5.7 Experimental range dependent SNR for maximum and minimum polarization orientations....101

Figure 5.8 G_{imp} in detection wavelength of 532 nm verses local time on 19 February 2005 102

Figure 5.9 G_{imp} in detection wavelength of 532 nm verses solar zenith angle 102

Figure 5.10 Gimp in detection wavelength of 532 nm verses solar zenith angle 103

Figure 5.11 PWV (cm) loading verses local time on 19 February 2005 and 23 February 2005 104

Figure 5.12 Theoretical model agrees with experimental measurements: 19 February 2005 Rayleigh scattering alone is also shown.....107

Figure 5.13 Relative humidity, RH, verses local time of New York City on 23 February 2005.....110

Figure 5.14 The particle equivalent radius ratio r/ r_o verses relative humidity, RH, at different equivalent radius, r_o, in the dry state (RH = 0), and for two aerosol models at 20º C temperature. 110

Figure 5.15 Theoretical model: 23 February 2005 111

Figure 5.16 Theoretical model agrees with experimental measurements: 23 February 2005 112

Figure 5.17 Comparison between solar azimuth angle and angle of polarization rotation needed to achieve minimum P_b: 14 April 2005 113

Figure 5.18 The scattering angle θ_{sc} between the solar and lidar directions for the scanning lidar geometry as function of lidar zenith angle and time of day showing periods where SNR improvement can be significant. The vertical lidar result is also plotted to contrast the time periods.....115

Figure 5.19 Multiple scattering models $\tau_{aer} = 0.5$ showing the minimum noise is parallel to the scattering plane irregardless of OD, $\Delta\phi$ is the azimuth angle difference between the scattering and the polarization planes.....116

Page

Figure 5.20 Variation of Improvement factor as function of scattering angle and optical depth using radiative transfer theory 119

Figure 6.1 Aerosol Backscatter processed with CCNY algorithm, S ratio from 10-100.....128

Figure 6.2 Smoke Plumes from MODIS satellite.....129

Figure 6.3: July 21 Integrated optical depth (OD), using Fernald method, as function of Sa ratio (OD~0.4 at 532 nm, OD ~0.65 at 355 nm).....130

Figure 6.4 Optical Depth Comparisons to validate choice of extinction to backscatter ratio for 532nm Sa~80. 130

Figure 6.5 Lidar extinction profiles showing existence of plumes.....131

Figure 6.6 Angstrom Coefficient using 355-532nm lidar channels for weak plume at 9:30 AM EST. 132

Figure 6.7 Angstrom Coefficient using 355-532nm lidar channels for weak plume at 10:10 AM EST. ...133

Figure 6.8 July 22 Backscatter of thin hydrated clouds.....134

Figure 6.9 July 22 Backscatter of thin hydrated clouds.....135

Figure 6.10 Hysplit Back-trajectories showing source of smoke plumes.....136

Figure 6.11 Rainfall Hysplit Back-trajectories for two vertical plumes at 1500 UTC (11EST) seen by our lidar. Track to northwest Canadian fires 137

Figure 6.12 PM2.5, Corresponding surface air quality measurements- NYS DEC, NYC 138

Figure 6.13 CO, Corresponding surface air quality measurements- NYS DEC, NYC 139

LIST OF TABLES

Page

Table 1-1 Different aerosol types and the corresponding aerosol lidar ratio $S_a(R)$ 14

Table 1-2 Lidar classification and related research 30

Table 3-1 Stationary lidar system specification 41

Table 3-2 Mobile lidar system specification 44

Table 3-3 Different aerosol types and the corresponding aerosol lidar ratio $S_a(R)$ 54

Table 4-1 Wedge-like shape diaphragms most excellent selection: Position, dimensions, and shape due to different ranges for the mobile monostatic biaxial lidar at the CCNY.....70

Table 4-2 Image size vs. telescope focal length for different lidar range. Effective FOV (ϕ_{eff}) is shown no big different in the higher range for a variety of *f*. Normalized ϕ_{eff} with respect to ϕ_{eff} of (f = 4m) is also shown. 80

Table 4-3 Detectors selection improved SNR. Main PMTs characteristics of CCNY lidars: both previous and current systems are shown. (Hamamatsu) 88

Table 5-1 Lidar system specifications.....94

Table 5-2 Comparison of experimental results to verify shot noise operation ($\Delta R = \sqrt{R}$).....100

Table 5-3 Dynamic mode parameters of bimodal aerosol distribution from MODIS aerosol model.....118

NOMENCLATURE

$\xi(R)$	Overlap function
λ	Wavelength
λ_L	Laser Wavelength
$\beta(R)$	Backscatter coefficient
$\alpha\ (R)$	Extinction coefficient
$S_a = \alpha_a(R)/\beta_a(R)$	Aerosol lidar ratio (a = for aerosol)
R	Target range
τ	Optical depth
θ	Incidence angle
P_r *and* P_t	Received and transmitted power
FOV	Field of View
GF	Geometric form Factor
λ_{ON}	On-line wavelength
λ_{OFF}	Off-line wavelength
$N_x(R)$	The gas number density
$\Delta\sigma = \sigma(\lambda_{ON}) - \sigma(\lambda_{OFF})$	Differential absorption cross section of the molecular species of interest in the DIAL
σ_D	Doppler broadened line
κ_B	Boltzmann constant, $\kappa_{\mathbf{B}} = 103806 \times 10^{-16}\, erg.\deg^{-1}$
T	Temperature
δ_S	Degree of depolarization of spherical particles
δ_{NS}	Degree of depolarization of non-spherical particles
θ_s	Scattering angle
r_p	Particle radius
$B(T)$	Planck function
V	The oscillator frequency
c	The speed of light

τ_m	Molecules optical thickness
f	Telescope focal length
P_b *or BGP*	Background noise power
$P(\lambda_L, R)$	Total scatter laser power received from a range R at wavelength of λ_L
A_o/R^2	Solid angle of the receiver optics
$A_o = \pi * t_o^2$	The area of the telescope primary mirror
t_o	Effective radius of telescope mirror
$\xi(\lambda)$	The receiver's spectral transmitter factor
$\tau_L = t_1 + t_2$	Laser pulse rectangular duration
I:	The laser beam intensity
$d\sigma(\lambda,\theta)/d\Omega$	The backscatter cross section
$\sigma(\lambda)$	Extinction cross section
$\left(S_m = \frac{\alpha_m(R)}{\beta_m(R)}\right)$	Molecular extinction to backscatter ratio
$c\tau_L$	Laser pulse length
$\overline{P} \equiv PR^2$	The range corrected backscattered power.
$AMR \equiv \frac{\beta_a(R_{\max})}{\beta_m(R_{\max})}$	Aerosol backscattering to molecular backscattering coefficients
$T(R)$	Atmospheric transmission
$L(R) = \sqrt{L_0 + \theta^2 R^2}$	The laser beam radius at rang of R
L_0	The laser output aperture radius
θ_L	The laser's half divergence angle
$t_T(R) = t_0 + \phi R$	FOV cross section radius of the receiver optics at rang R
ϕ_r	Receiver optics half opening angle
ψ	Azimuthally angle from a vertical plane passing through the axis.
$F(R, r, \psi)$	Laser irradiance distribution function
Γ	The overlap area function
$d = b_o + R\delta$	Distance between the laser and telescope optical axes at altitude R
δ	Angle between the telescope and laser axes. In our system $\delta = 0$
E_{det}/E_{scat}	Energy transferred to the photodetector to the energy reaching the telescope primary mirror
D_o	The field stop diameter

$i_d = \frac{e\langle n_e^d \rangle}{\tau_d}$	the mean photocathode noise
$\langle n_e^d \rangle$	The mean number of photocathode electrons created in the interval τ_d in the absent of light
i_J	Johnson (thermal) noise current
e	The electronic charge
$E_b^T(\lambda) = E_b^N(\lambda) + v_\eta E_b^L(\lambda_L)$	The total background
$E_b^N(\lambda)$	The natural background
$E_b^L(\lambda_L)$	The laser scatters background
i_n	The shot noise
i_b	The equivalent background current
I_n	The noise current at anode
$I_s = G\xi_e i_s$	The anode signal current
G:	The dynode chain gain (10^5 - 10^7)
G_{imp}	SNR improvement factor
$\tilde{\omega}$	Single-scatter albedo
S_i	scattering function for each polarization
Q_e	Mie extinction efficiency
$q = 2\pi a / \lambda$	Normalized size parameter
$P_b^{\max}$, $P_b^{\min}$	Maximum noise, and the minimum noise
a_w	Water activity of a soluble aerosol at radius $r\,(\mu m)$
ρ	The particle density relative to that of water
$m_w(a_w)$	The mass of condensed water
m_o	The dry particle mass
σ	The surface tension on the wet surface
V_w	The specific volume of water

ACRONYMS

ABL	Atmospheric Boundary Layer
A/D	Analog to Digital Converter
AMR	Aerosol backscattering to molecular backscattering coefficients
AOD	Aerosol optical depth
APD	Avalanche photodiodes
BC	Boundary Conditions
BGP	Sky background noise power
CALIPSO	Cloud-Aerosol Lidar and Infrared Pathfinder Satellite Observations
CCNY	The City College of New York
CLR's	Coherent LASER RADARS
CPL	Cloud Physics Lidar
CREST	Cooperative Remote Sensing Center
CUNY	The City University of New York
CW	Continuous Wave
DAS	*D*ifferential *A*bsorption and *S*cattering
DIAL	DIfferential Absorption Lidar
DOAS	Differential Optical Absorption Spectrometer
EM	Electromagnetic Radiation
ENVISAT	Environnemental Satellite (ESA)
ERS	ESA Remote Sensing Satellite
ESA	European Space Agency
EST	Eastern Standard Time
FSL	Forecast Systems Laboratory
FTIR	Fourier Transform Infrared spectroscopy
GIS	Geographical Information System
GLOBE	GLObal Backscatter Experiment
GPS	Global Positioning System
HH	Horizontal like-polarization
HSRL	High Spectra Resolution Lidar ()
HV	Horizontal-vertical cross-polarization
IF	Interference Filters

IR	Infrared radiation
MPL	Micro-pulse lidar
LADAR	LAser Detection And Ranging
LaRC	Langley Research Center
LASER	Light Amplification by Stimulated Emission of Radiation
LIDAR	LIght Detection And Ranging (LASER RADAR = Optical RADAR)
LITE	LIDAR In-space Technology Experiment
LOS	Line Of Sight
NASA	National Aeronautics and Space Administration
NASDA	National Space Development Agency of Japan
ND	Neutral Density filters
NERC	Natural Environment Research Council
NIES	Japanese National Institute for Environmental Studies
NLR	Noncoherent Laser Radar
NOAA	National Oceanic and Atmospheric Agency
PC	Photon Counting
PBL	Planetary boundary layer (lowest 1-2 km of the atmosphere)
PDL	Polarization Diversity Lidar
PMT	Photo Multipliers Tubes
PSCs	polar stratospheric clouds
PWV	Precipitable water vapor
RADAR	RAdio Detection And Ranging
REALM	Regional East Atmospheric Lidar Mesonet
RH	Relative Humidity
SAR	Synthetic Aperture Radar
SHG	Second Harmonic Generation
SNR	Signal-to-Noise Ratio
SPARCLE	SPAce Readiness Coherent Lidar Experiment
THG	Third Harmonic Generation
TOTE/VOTE	NASA Tropical Ozone Transport Experiment/ Vortex Ozone Transport Experiment
TW	Tera-watt
UV	Ultraviolet radiation
Vis	Visible radiation

1 INTRODUCTION

1.1 Lidar Background

1.1.1 Lidar Historical Background

After World War II the first *LI*ght *D*etection *A*nd *R*anging (lidar) system was invented (Jones 1949). The source was a flash light between aluminum electrodes with high voltage amplitude transmitter, and the receiver optics were two mirrors. A photoelectrical cell was used as a detector. During daylight, this system had been used to measure cloud base heights up to 5.5 km. At that time the acronym *lidar* didn't exit (Middleton 1953). The real revolution of lidar began with the invention of the laser (light amplification by stimulated emission of radiation) in 1960. Using laser as a source of light in a lidar system is referred to as "*Laser Radar, or Ladar, or Lidar*". Lidar operates in wide band region of the electromagnetic spectrum; ultraviolet (225 nm- 400 nm), visible (400 nm-700 nm), and infrared radiation (700 nm- 1200 nm). Lidar systems are used as ground based stations (stationary or mobile), or can be carried on platforms such as airplanes or balloons (in-situ operations), or on satellites. National Oceanic and Atmospheric Agency (NOAA) and National Aeronautics and Space Administration (NASA) aircraft and satellites are the most famous lidar platforms in the United States of America. Some other platforms are employed around the world by groups such as the European Space Agency (ESA), the Japanese National Institute for Environmental Studies (NIES), and the National Space Development Agency of Japan (NASDA).

1.1.2 What is a Lidar

*LI*ght *D*etection *A*nd *R*anging (lidar) is an optical remote sensing system for probing the earth's atmosphere through Laser transmitter and elastic and/or inelastic scattering techniques. Most of the remote sensing lidar systems consist of three functional subsystems, as shown in (Figure 1.1), which vary in the details based on the particular applications. These subsystems are:

[1] Transmission subsystem

[2] Receiver subsystem

[3] Electronics subsystem

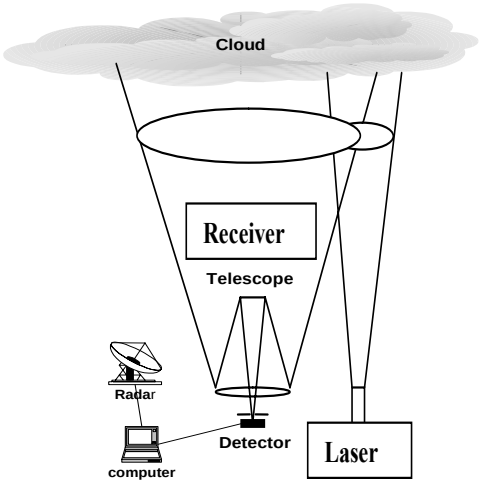

Figure 1.1 Essential elements of a lidar system

In the **transmission** subsystem, a laser (pulsed or continuous wave (CW)) is used as a light source. More than one laser can be used according to lidar type and objective of the measurements. Laser pulses, in the ideal case, are very short pulses with narrow bandwidth, high repetition rate, very high peak power, and are propagated with a small

degree of divergence. The laser pulse is transmitted through transmission optics to the atmospheric object of interest. The essential function of the output optics is to improve the output laser beam properties and/or control the outgoing beam polarization. Elements such as lenses and mirrors are used to improve the beam collimation; beam expansion is used to reduce the beam divergence and the area density of the laser pulse. Fiber optic cable, filters, and cover shields or housings serve the dual purpose of preventing the receiver detectors from saturation from any unwanted transmitted radiations and of protecting the user's eyes against any injury. Wave length selective devices is also used such as harmonic generator to create the second, the third and even the fourth harmonic. Polarizer is used to control the transmitted beam polarization and finally polarization measurement equipments. I used in this work two types of pulsed laser, Q-Switched (an optical on-off switch) Nd: YAG (Continuum Infinity 40-100) and Q-Switched Nd: YAG (Surelite)

A Receiver subsystem consists of an optical telescope to gather and focus the backscattering radiations and receiver optics to provide the detector (*P*hoto*M*ultiplier *T*ube (PMT) or *A*valanche *P*hoto *D*iode (APD)) with desirable collimated or/and focused strong polarized signal. Components such as mirrors, collimated lenses, aperture (field stop), ND (*N*eutral *D*ensity) filters, and *I*nterference *F*ilters (IF) are to provide special filtering against sky background radiations, analyzers (polarization selection components) are needed to select the necessary polarizations based on the applications and/or to discriminate against the unwanted background noise (as shown in chapter 7), and electro-optical elements that convert light energy to electrical energy (detectors). There are two basic types of detectors for lidar systems; the photomultiplier tube (PMT), and the

avalanche photo diode (APD). In addition to the optics mounts and the manually operation aids, automated alignment capabilities for lidar long-term unattended operations are needed.

Electronic subsystem consists of data acquisition (mostly, multiple channels), displaying unites, *A*nalog to *D*igital (A/D) signals conversions, radar and radar circuit, control system especially for our polarization discrimination technique which I presented in this dissertation (Chapter 7) to track the azimuth angles to improve the SNR. In addition, software (Labview and Matlab) is needed for signal processing purposes, as well some hardware such as platforms (van for a ground based mobile lidar, airplane or balloon for in-situ airborne lidar and satellite for higher altitude space-based scanning lidar), a temperature control unit, orientation stability elements, storage units and some additional equipment depending on lidar's type and measurement objective.

1.2 How Does Lidar Work?

Using the well known fact that the laser energy of optical frequencies is highly monochromatic and coherent, and the revolution of developing the Q-Switching by McClung and Hellwarth on 1962, (McClung 1962), laser has the capability of producing pulses with very short duration, narrow bandwidth, very high peak energy, propagating into the atmosphere with small divergence degree. This prompted the development of backscattering techniques for environment and/or atmosphere compositions and structure, (aerosol, ozone, cloud plumes, smoke plumes, dust, water vapor and greenhouse gases (carbon dioxide for example), temperature profile, wind speed, gravity waves, etc.), distributions, concentrations and measurements. These measurement techniques are to

some extent analogous to radar, except using light waves as an alternative to radio waves. Consequently, scientists denote lidar as laser radar. The essential idea of lidar operations and measurements is based on the shape of the detected backscattering lidar signals with wavelength of (λ) if the transmitted laser beam of wavelength λ_L is scattering back from distance R. This backscattering shape depends on the properties of the lidar characteristics and the atmosphere specifications. The transmitted lidar signal can be absorbed, scattered, and shifted, or its polarization can be changed by the atmosphere compositions and scattered in all the directions with some signals scattered back to the lidar receiver. Two parameters, in the lidar return equation, relate the lidar detected signal power and the atmospheric specifications. These parameters are the extinction and scattering coefficients, $\alpha\ (\lambda, R)$, $\beta\ (\lambda, R)$ respectively. By solving the lidar equation for those coefficients one can determine various atmospheric properties. An example of these determination processes, which based on the lidar type and the physical process used in the measurements, have been introduced in chapter 3 of this thesis.

1.3 Lidar Classifications

The kind of physical processes (Rayleigh, Mie, elastic and inelastic backscattering, absorption, florescence , etc.), the types of the laser employed (Die, and ND:YAG), the objective of the lidar measurements (aerosols and cloud properties, temperature, ozone, humidity and water vapor, wind and turbulence, etc.), the atmospheric parameters that can lidar measure (atmospheric density, gaseous pollutants, atmospheric temperature profiles), the wavelength that been used in the measurements (ultraviolet (UV), infrared (IR), and visible), the lidar configurations (monostatic, biaxial, coaxial, vertically pointed and scanning lidars and bi-static), the measurement mode (analogue, digital and/or both),

the platform type (stationary in laboratories, mobiles in vehicles, in situ (balloon and aircraft), and satellite), number of wavelength (single, and multiple wavelengths) are some ways to classify lidar systems. In the following section anticipate brief descriptions of various types of lidar, focusing mainly on those types of our research interest.

1.3.1 Types of Lidar Returns

If light is directed towards another direction because of interaction with matter without loss of energy (but losing intensity) the fundamental physical process is called *scattering* of light. The light scattering occurs at all wavelengths in the whole electromagnetic spectrum and in all directions. Since lidars sense only the scattering radiations in the backward direction (scattering angle $\theta_s = \pi$ for monostatic vertically pointed lidar), we call them lidar *backscattering* radiations or signals. In terms of lidar return signals, I classify lidar into the following types (Rayleigh, Mie, Raman, DIAL, Doppler, and florescence lidars):

1.3.1.1 Rayleigh Scattering Lidar:

In 1871, Lord Rayleigh discovered a significant physical law of light scattering with a variety of applications. The most famous applications of this discovery are the blue sky and the sky light partial polarization explanations. Rayleigh scattering is elastic (no wavelength shift) scattering from atmospheric molecules (particle radius is much smaller compared with the incident radiation wavelength i.e. $r_p << \lambda$): sum of Cabannes (sum of coherent, isotopic, polarized scattering, which approximately 96% of the scattering) and rotational- Raman S and S' branch scattering which only 4% of the scattering

proceedings. Based on the Rayleigh-Jeans law, [the Planck radiance is linearly proportional to the temperature, $B(T) \approx (2\kappa_{\mathbf{B}} v^2 / c^2)(T)$, where *B(T)* is the Planck function, $\kappa_{\mathbf{B}}$ is the Boltzmann constant $\kappa_{\mathbf{B}} = 103806 \times 10^{-16} erg.\deg^{-1}$, v is the oscillator frequency, c the speed of light, and T the absolute temperature] (Liou 2002), we can use the Rayleigh lidar technique to derive the atmospheric temperature profile above the aerosol free region (*R >30 km*). In other words, molecular scattering (Rayleigh scattering or aerosol-free scattering) is proportional to the atmospheric density, and the atmospheric temperature profile can be easily derived from the atmospheric density in the range above the aerosol layers (above 30 km to below 80 km). Unfortunately, above 80 km temperature measurements require a powerful transmitter laser (up to 20 W) and receiver telescope (up to 4 m aperture) which are difficult for mobile or airborne platforms (Fhjii and Fukuchi 2005). Finally, assuming the atmosphere consists only of molecules and outside the gaseous absorption bands of the atmosphere, the atmosphere optical thickness can be approximated by

$\tau_m = 0.008569\lambda^{-4}(1 + 0.0113\lambda^{-2} + 0.00013\lambda^{-4})$ where λ is measured in micrometers.

Rayleigh scattering strongly depends on the wavelength of the transmitted light (λ^{-4}) which explains the blue color of the sky, where the scattering efficiency is proportional to λ^{-4}, i.e. rapid increase in the scattering efficiency with decreasing λ. This behavior leads to more scatter in blue than red light of the air molecules.

1.3.1.2 Mie Backscatter Lidars

For particle radius (r_p) larger than $\lambda / 2\pi$, (i.e., $r_p > \lambda / 2\pi$, where λ is wavelength of radiation), Rayleigh scattering is not applicable but Mie scattering applies (Mie 1908; Measures 1984; Liou 2002). Mie scattering is elastic scattering which is suitable for detection of large spherical and non-spherical (Barber 1975), (Wiscombe 1980) aerosol and cloud particles mainly in the troposphere. The backscattering signals from aerosol or molecules and the absorption from molecules are very strong in the lower part of the atmosphere (below 30 km), which is enough to determine various properties about the atmosphere. Micrometer-sized aerosol and clouds are great indicators of atmosphere boundary phenomena where they show strong backscattering interaction. By Mie scattering theory, the optical properties of water droplets can be evaluated for any wavelength in the electromagnetic spectrum (from solar to microwave) (Deirmendjian 1969). Clouds covered about 50% of the earth (Liou 2002). Clouds also have an important impact on the global warming disaster when clouds trap the outgoing terrestrial radiation and produce a greenhouse gaseous effect. Mie backscattering lidar measures backscattered radiation from aerosol and cloud particles and their polarization as well (Mie 1908; Liou 2002)). Its performance is similar to radar manner. A laser pulse of energy is transmitted, interacted with different objects and then backscattered (scattering angle =180°) to the receiver detector. The detected backscattering signals are interrelated with some properties of that object (even with low concentrations or small change in concentrations of dust or aerosol objects). Mie scattering follows *(λ^{-0} to λ^{-2})*, i.e., it is not significantly dependent on the wavelength.

1.3.1.3 Raman (Inelastic Backscattering) Lidars:

Raman scattering is inelastic scattering with cross section up to three times smaller than the Rayleigh cross section in magnitude. A Raman scattered signal is shifted in frequency from the incident light (Raman-shifted frequency). The Raman scattering coefficient is proportional to the atmospheric density when the air molecule (nitrogen or oxygen) is used as Raman materials (Fhjii and Fukuchi 2005). Generally speaking, Raman lidar measure intensity at shifted wavelength (Stephens 1994) and it detects selected species by monitoring the wavelength-shifted molecular return produced by vibration Raman scattering from the chosen molecules. Raman lidar originally, was developed for NASA Tropical Ozone Transport Experiment/ Vortex Ozone Transport Experiment (TOTE/VOTE) for methane (CH_4) and Ozone measurements (Heaps 1996). Also it has been used to correct the microwave temperature profile in the stratosphere (Heaps 1997).Typically; inelastic scattering (such as Raman) is very weak; therefore the daytime measurement is difficult due to the strong background solar radiation. This restricts Raman lidar measurements to nighttime use where background solar radiation is absent.

On the other hand, Raman lidar is a powerful remote sensing tool used to measure and trace constituents where elastic lidar can not identify the gas species (Fhjii and Fukuchi 2005). Raman-Mie Lidar technique is also used to determine the extinction and the backscattering coefficients assuming the knowledge of air pressure (Ansmann 1992). In this thesis I introduced, in chapter 7, a new polarization technique to improve lidar Signal-to-Noise Ratio (SNR) by reducing the background noise during the daytime measurements. This will help for successful diurnal operation of Raman lidar.

1.3.1.4 DIfferential Absorption Lidar (DIAL):

*D*ifferential *A*bsorption and *S*cattering (DAS) is a good combination for detecting a good resolution of water vapor in the atmosphere using the H_2O absorption line at 690 nm (Schotland 1966; Measures 1984). DAS technique is one of the best methods for detecting constituents for long-range monitoring based on a comparison between the atmospheric backscattering signals from two adjacent wavelengths that are absorbed differently by the gas of interest (Measures. R. M. 1972). The closest wavelength to the absorption line of the molecule of interest (i.e., strongly absorbing spectral location due to the presence of an absorbing gas) is usually called on-line and denoted as (λ_{ON}) and the other laser wavelength is called off-line and denoted as (λ_{OFF}). *DI*fferential *A*bsorption *L*idar (DIAL) technique is a unique method to measure and trace gaseous concentrations in the *P*lanetry *B*oundary *L*ayer (Welton, Campble et al.) (Welton, Campble et al.) in three dimensional mode (3D) using of the DAS principal. The gas number density $N_x(R)$ can be derived from the differential absorption cross section of the molecular species of interest ($\Delta\sigma = \sigma(\lambda_{ON}) - \sigma(\lambda_{OFF})$) in the DIAL equation (Fhjii and Fukuchi 2005)

$$N_x(R) = \frac{1}{2\Delta\sigma}\frac{d}{dR}\ln\frac{P(R,\lambda_{OFF})}{P(R,\lambda_{ON})} \quad \textbf{(1.1)}$$

Where $P(R,\lambda_{ON})$ and $P(R,\lambda_{OFF})$ the power backscattered signal received from distance R for both wavelengths. Special careful must be taken into account when selecting the adjacent wavelengths, where the different between the two wavelengths is preferred to be

less than 1 cm $^{-1}$, otherwise another two terms must be considered in the DIAL equation. DIAL, as a range resolved remote sensing technique, can detect lots of pollutants and greenhouse gases (H_2O, SO_2, O_3, CO, CO_2, NO, NO_2, CH_4, etc.) which play a big role in climate change and the earth's radiative budget. DIAL is possible in the UV (200 to 450 nm), the visible, and the near IR (1 to 5 micrometer), and in the mid-IR (5-11 micrometer). For example to measure Ozone as a green house gas with fatal direct effect on human health particularly in the troposphere, DIAL can be used in two appropriate bands; UV band (at 256 nm) and the mid-IR band (960 to 1070 cm $^{-1}$). DIAL operations advantages are successful both day and night, detecting gases and aerosol profiles simultaneously, and ground based, airborne, and space based operations as well.

1.3.1.5 Doppler Lidars

Atmospheric laser Doppler velocimetry including measurements of tornados, storms, wind, turbulence, global wind cycles, and the atmosphere temperature are some of the most important remote sensing techniques (Measures 1984). Doppler broadening is due to the Doppler shift associated with the thermal motion of radiating (absorbing) species in the mesopause region such as Na, K, Li, Ca, and Fe (Measures 1984). Furthermore, the atmospheric temperature can be detected by measuring the Doppler broadening and the measured global wind pattern can be determined by measuring the Doppler shift of laser-induced florescence from atmospheric metals atoms such as Na in the middle and upper atmosphere (Bills 1991; She and Yu 1994). The use of Doppler broadening of the structure of Na D_2 line (by narrowband lidar) technique to determine the range resolved high resolution temperature profile of the mesopause region (75-115 km, is also called

MLT for Mesosphere and Lower Thermosphere) and was proposed by Gibson et al. in 1979. The principle idea is that the absorption line will be broadened because of the Doppler Effect for a single Na atom. Doppler broadened line is given by $\sigma_D = \sqrt{\frac{\kappa_B T}{M\lambda_0^2}}$, where M is the mass of a single Na atom, κ_B is the Boltzmann constant, λ_0 is the mean Na D_2 transition wavelength, and T is the temperature. As shown the Doppler broadened σ_D is a function of temperature. Therefore if we measure σ_D line-width, we can derive the temperature of the Na atoms in the mesopause which equal to the surrounding atmosphere temperature where Na atom is in equilibrium condition in the mesopause region (Fhjii and Fukuchi 2005).

1.3.1.6 Resonance Fluorescence Lidars

A Rayleigh lidar signal is useless above ~ 85 km, because of the low atmospheric density above that altitude. The backscattering cross section of Resonance fluorescence lidars is about 10^{14} times higher than Rayleigh backscattering cross-section for the same transmitter and receiver specifications, thus Resonance fluorescence lidars can be used in the upper atmosphere measurements. Resonance fluorescence lidars are measuring intensity at shifted wavelength using of Doppler technique (Bills 1991; She and Yu 1994) or Boltzmann technique (Gelbwachs 1994). Fluorescence lidar is used to measure metallic species in the upper layer of the atmosphere (~90km) such as, Na, K, Li (Jegou, M.Chanin et al. 1980), Ca and Fe (Granier, J. P. Jegou et al. 1989; Gardner, C. S. et al. 1993) and/or volcanic stratospheric aerosol, polar stratospheric clouds (PSCs), gravity waves, and stratospheric ozone layer. This lidar has high sensitivity and accuracy. It is

also, used to determination of wind, temperature, and study of thermal structure and complex atmospheric dynamics.

1.3.2 Lidar Wavelengths

1.3.2.1 Elastic Lidar:

An elastic scattering is defined as light scattering with no apparent wavelength shift or change with the incident wavelength. Elastic backscatter lidar operation, as one of the most popular lidar systems, is based on the elastic scattering physical process and it is detecting the total atmospheric backscatter of molecular and particle together without separation. Therefore, elastic backscattering lidar is the sum of Rayleigh and Mie scatterings. The main disadvantage of elastic lidar is the difficulty of separating Mie form Rayleigh signals. More details explain how to overcome this disadvantage are given in the following subsection.

1) It is difficult to determine accurately the volume extinction coefficient of the particles or aerosol, where we can not separate Mie form Rayleigh signals. In this case, we have to assume the particle lidar ratio, $S_a(R)$, where $S_a(R) = \frac{\alpha_a(R)}{\beta_a(R)}$, to solve the lidar equation for the aerosol extinction coefficient ($\alpha_a(R)$). This assumption is impossible to estimate reliably; since the aerosol lidar ratio $S_a(R)$ varies strongly with the altitude ($S_a(R)$ varies between 20 and 100) due to the relative humidity increment with the altitude (S ratio depends on chemical, physical and morphological properties of the particles which are relative humidity dependent). As shown in Table 1-1 (Kovalev and

Eichinger 2004), big variations of aerosol typical lidar ratio for different aerosol types have been determine at 532 nm wavelength using Raman lidar. Figure 1.2 shows a lidar return signal on June 30, 2004 at the CCNY site. The figure also shows an example of the aerosol lidar ratio $S_a(R)$ retrieval between 20 and 100.

Table 1-1 Different aerosol types and the corresponding aerosol lidar ratio $S_a(R)$

Aerosol (particle) types	**Aerosol lidar ratio $S_a(R)$ (sr)**
Marine Particle	20-35
Saharan dust	50-80
Less absorbing urban particles	35-70
Absorbing particles from biomass burning	70-100

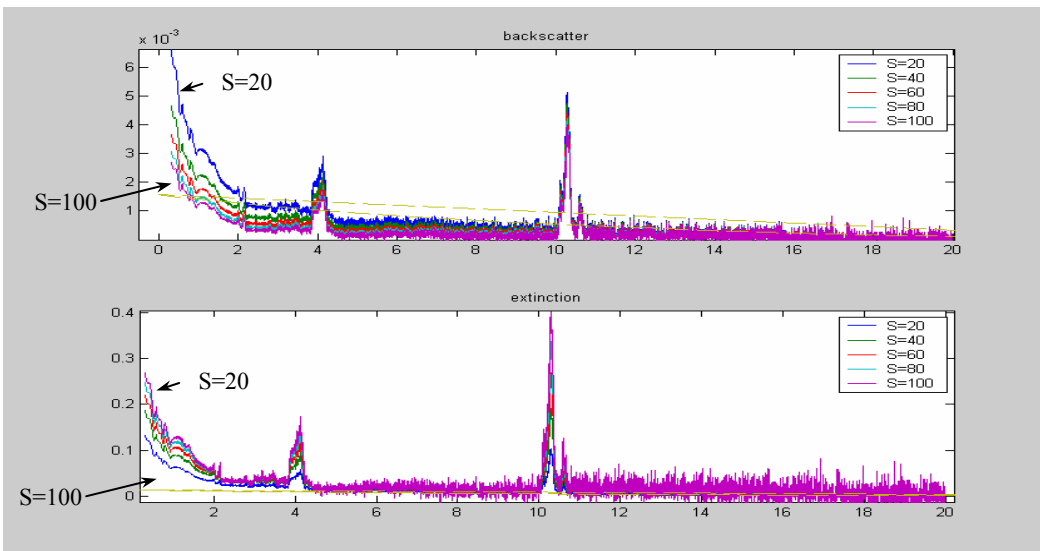

Figure 1.2 CCNY lidar retrieval for $S_a(R)$ ration, June 30, 2004

To determine the aerosol lidar ratio $S_a(R)$, we can use Raman lidar and High Spectra Resolution Lidar (HSRL) to get the extinction profile for particle then $S_a(R)$ or use sun-

photometer observatory which obtains the optical depth then seeking a solution by back integration. More details are given below.

a) Using Raman lidar and High Spectra Resolution Lidar (HSRL) to determine the extinction profile for particle and the particle backscatter coefficient can be obtained directly as well. These two lidars detect a separate backscatter signals from particle and molecular.

b) Using Sun-photometer observatory to obtain the optical depth (integration over the extinction coefficient profile) for both aerosol and molecule. This solution fixes the reference boundary condition at the top of the lidar range ($R_{\max}$, where the particle backscatter coefficient $\beta_a(R_{\max})$ is negligible compared to the known molecular backscatter value) and seeks a solution by back integration (Klett 1981) that is more stable than the corresponding forward solution. Therefore, given the following data set $\{S_a, \beta_a(R_{\max})\}$, the lidar signal can be inverted to obtain both $\beta_a(R), \alpha_a(R)$. Therefore, an estimate of the data set $\{S_a, \beta_a(R_{\max})\}$ is required and the approach we use to analyze the lidar signals and estimate the optical coefficient error is outlined below.

- A set of reasonable ratios $C \equiv \frac{\beta_a(R_{\max})}{\beta_m(R_{\max})}$ and a set of reasonable aerosol ratios $S_{\min} < S_a < S_{\max}$ are generated. It should be noted that above the boundary layer, the aerosol concentration decreases substantially and the ratio can usually be bounded by some small number less than one with tighter constraints obtained by increasing the lidar range.
- The aerosol profiles $\beta_a(R), \alpha_a(R)$ for each set of parameters, is calculated.

- For each parameter set, the optical depth over the entire lidar range including the molecular contribution above the lidar range

$$\tau_L(S,C) = \int_0^{R_{\max}} (\alpha_a(R') + \alpha_m(R'))\, dR' + \int_{R_{\max}}^{\infty} \alpha_m(R')\, dR' \qquad \text{is calculated.}$$

- The admissible profiles are those that simultaneously satisfy the constraints $C_{\min} \le C \le C_{\max}$ and $\tau_{\min} \le \tau_L \le \tau_{\max}$ estimated from **sun-photometry** measurements.
- For each range *R*, a histogram can be constructed for both optical coefficients providing a reasonable estimate of both the aerosol extinction and backscatter profiles for each range.

For more details see Chapter 7, where I introduced the ground based lidar in supporting of -NEAQS and NASA-INTEX-NA experiments.

Finally, elastic scattering is unable to identify the gas species but can be detect and measure particles and clouds (Fhjii and Fukuchi 2005). The experimental results, in this work, were provided by elastic backscatter lidars.

1.3.2.2 Inelastic Backscattering Lidar:

The transmitted wavelength is different than the detected wavelength on inelastic lidars. An example of inelastic lidar is Raman Lidar. A Raman signal is very weak; therefore Raman lidar operations are restricted to the nighttime due to the background solar radiations during the daytime. Three ways to avoid this problem, they are: first is running Raman lidar within the solar-blind region (230-300 nm), the second of them is applying narrow-bandpass filter or Fabry-Perot interferometer, and the third method is operating

Raman lidar in the visible band of the spectra, during the daytime, and deduct the background solar radiation noise.

1) The first method is running Raman lidar within the solar-blind region (230-300 nm), where the ozone layer in the stratosphere (20-30 km) absorbs the lethal solar radiation in this spectral interval. Consequently, lidar can be operated diurnally in the solar-blind region without getting affected by the solar background noise. However, the main drawback of running lidar in this region is the attenuation of the transmitted and the return signal by the stratospheric ozone. Another drawback is the eye hazard issue. Using this technique, in 1980th, there were some attempts to measure water vapor and temperature using multiwavelength in the solar-blind region (Renaut 1980; Petri 1982).

2) The second method is applying a narrow-bandpass filter or Fabry-Perot interferometer (Kovalev 2004). But the flitter will attenuate the signal strength as well. This is considered the main disadvantage of this method.

3) In this thesis a practical strong solution has been proposed and proven. The principal idea is to operate Raman lidar in the visible band (607 nm for N_2, 407 nm for water vapor, and 403 nm for liquid water vapor) of the spectra and deduct the background solar radiation noise, simultaneously during the daytime optimally. This objective can be accomplished by the following techniques:

a) Using a polarization discrimination technique to discriminate between the sky background radiation noise and the backscattering signal (see chapter 7). This improved the lidar Signal-to-Noise Ration (SNR) up to 300 %, and the attainable lidar range up to 34%. This can be approached using two polarizations

at the transmitter and the receiver optics (Hassebo, B. Gross et al. 2005; Hassebo, Barry M. Gross et al. 2005; Hassebo, B. Gross et al. 2006).

b) Design a receiver diaphragm to accommodate the return signal and cut the unwanted background signal. This design included the aperture's (field stop) shape and position with respect to the telescope focal length (Hassebo, R. Agishev et al. 2004) as shown in Chapter 4.

1.3.2.3 Multiple Wavelength Lidar

When the lidar transmitter was a single wavelength laser, the lidar is called single wavelength lidar. However, the lidar is referred to as a multiple wavelength lidar if it is transmitting more than one wavelength into the atmosphere. All transmitted light into the atmosphere with wavelength shorter than 300 nm is absorbed by ozone and oxygen (solar-blind region). Wavelengths shorter than 300 nm are fatal wavelengths. So the minimum wavelength for elastic lidar is approximately 300 nm. The commonly used wavelengths in lidar operations are near infrared (1064 nm), visible (532 nm), and ultraviolet (335 nm) for backscatter lidars, and (607 nm) for N2, (407 nm) for water vapor, and (403 nm) for liquid water vapor. The multiple wavelength backscatter lidar can be used to distinguish between fine particles (emitted from fog, combustion, plume and burning smoke) and big particles such as water vapor or clouds. This can be achieved using angstrom coefficient as shown in Chapter 7 (Hassebo, Y. Zhao et al. 2005).

Another example for multiple wavelength backscatter lidar is the DIfferential Absorption Lidar (DIAL). DIAL is used to measure concentrations of chemical

species such as ozone, water vapor, pollutants in the atmosphere. A DIAL lidar uses two different laser wavelengths which are selected so that one of the wavelengths is absorbed strongly by the molecule of interest while the other wavelength is not. The difference in intensity of the two return signals can be used to deduce the concentration of the molecule being investigated**.**

1.3.2.4 Femto-second White Light Lidar:

Extremely high optical power (tera-watt) can be created from femto-second (1 fsec $=10^{-15}$ sec) laser pulse with 1mj energy. That is Femto-second white light lidar. Fsec-lidar is used to detect and analyze aerosol size and aerosol phase (measuring the depolarization), water vapor, and for better understanding of forecasting, snow and rain in the era of global warming and climate change. The inaccessibility to 3-D analysis disadvantage of Differential Optical Absorption Spectrometer (DOAS) and Fourier Transform Infrared spectroscopy (FTIR) have been covered by Femto-second white light lidar. At the same time it has the multi-component analysis capability of DOAS and FTIR by using a wide band light spectrum (from UV to IR), i.e., visible (Wöste, Wedekind et al. 1997; Rodriguez, R. Sauerbrey et al. 2002). A good example of fsec-lidar system, based on the well-known chirp pulse amplification (CPA) technique, can provide 350 mJ pulse with 70 fsec duration, peak power of 5 TW at wavelength of 800 nm (Fhjii and Fukuchi 2005).

1.3.3 Purposes of Lidar Measurements

1.3.3.1 Aerosol Lidar:

The atmosphere contains not only molecules but also particulates and aerosols including clouds, fog, haze, plumes, ice crystals, and dust. The aerosol is varied in radius; from a few nanometers to several micrometers. The bigger the aerosol size the more complex the calculations of their scattering properties. Aerosol concentration varies considerably with time, type, height, and location (Stephens 1994). Aerosols absorb and scatter solar radiation (all aerosols show such degree of absorption the ultraviolet and visible bands) and provide cloud condensation sites (Charleon 1995). Aerosol absorption degree indicates the aerosol type. Atmospheric aerosol altitude, size, distribution and transportation are major global uncertainties due to their effects on controlling the earth's planet climate stability and global warming issues. In addition of the impact of aerosol in the atmospheric global climate change (Charlson, J. Langner et al. 1991; Charlson, S. E. Schwartz et al. 1992) it also affects human health with diseases such as lung cancer, bronchitis, and asthma. These have been essential motivations to study aerosol properties and transportation. Lidars have been successfully applied to study stratospheric aerosols mainly sulfuric-acid/water droplet (Zuev V., V. Burlakov et al. 1998), tropospheric mixture aerosols of natural (interplanetary dust particle and marine) and of anthropogenic (sulfate and soot particles) (Barnaba F and Gobbi 2001) and climate gases such as stratospheric ozone (Douglass L. R., M.R. Schoeberl et al. 2000) as well as for analyzing the clouds properties (Stein, Wedekind et al. 1999). Aerosol sources can origin from nitrate particles, sea-salt particles, and volcanic ashes and rubble. Aerosol particle sizes were categorized as aitken, large, and giant particles (Junge 1955), where

- Dry radii < 0.1 μm, Aitken particles
- Dry radii 0.1 μm< r < 1 μm, large particles
- Dry radii r > 1 μm, giant particles

Aerosol concentration decreases with increasing altitude. 80% of the aerosols condense in the lowest two kilometers of the troposphere (i.e., within the planetary boundary layer (PBL)) as shown in Fig 1.3, for New York City on August 11, 2005.

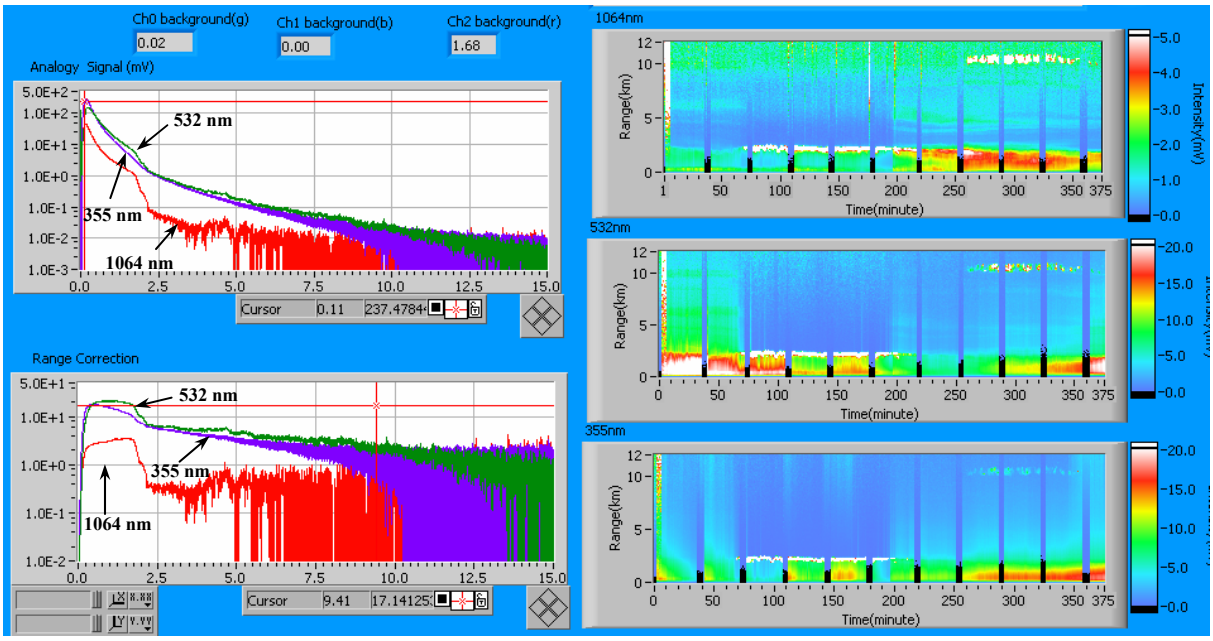

Figure 1.3 New York City aerosol PBL, Aug 11, 2005

The extinction profile is considered a very good indicator (in the cloud free case) of aerosol concentration. A principle of measuring aerosol is using the wavelength between 300-1100 nm to determine the particle extinction and backscattering profiles. A good example for lidar, that has been used to monitor aerosol without attendance, is Micro-Pulse Lidar (MPL) (Spinhirne 1991; Spinhirne 1993; Welton, Campble et al. 2001).

Several agencies around the world have been assigned special aerosol closure experiments to study the impact of the anthropogenic aerosol on our health, life, air quality, climate change, and earth's radiation budget. Some of these agencies are U.S. National Aeronautics and Space Administration (NASA), European Space Agency (ESA), Japanese National Institute for Environmental Studies (NIES), and National Space Development Agency of Japan (NASDA). Aerosol loading represents a major uncertainty in DIAL ozone measurements in the PBL. The aerosol life time is approximately several days to week, and it can be removed from the atmosphere through wet (rain, cloud) or dry depositions. Finally, High Spectral Resolution Lidar (HSRL) can be used as well to measure aerosol scattering cross section, optical depth, and backscatter phase function in the atmosphere by separating the Doppler-broadened molecular backscatter return from the un-broadened aerosol return. The molecular signal is then used as a calibration target which is available at each point in the lidar profile.

1.3.3.2 Cloud Lidar:

Cloud particle radius is larger than 1 μm (between about 2 to around 30 μm). Which is bigger than the lidar wavelength (300- 1100 nm), therefore lidars cannot measure the cloud size distribution (Fhjii and Fukuchi 2005). However, lidars can detect the cloud base, thickness, and its vertical profile where the lidar return signal from the cloud is very strong because cloud behaves as obstruction in the laser propagation path.

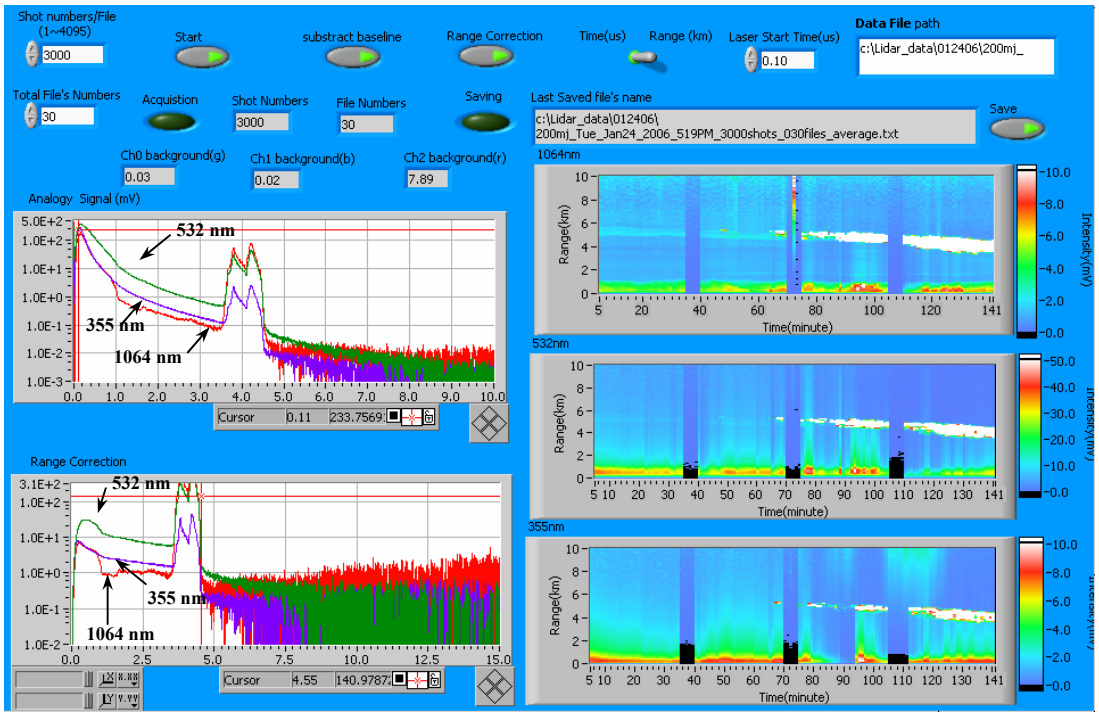

Figure 1.4 CCNY lidar data shows cloud base, thickness, and structure, Jan 25, 2006.

As shown in Fig 1.4, using three wavelengths of 355, 532, 1064 nm, the CCNY stationary lidar detected clouds vertical structure between 3.5 to 4.5 km height, and the planetary boundary layer (Welton, Campble et al.) on January 25, 2006.

Clouds cover approximately 50% of the earth (Liou 2002). Based on the altitude (i.e., temperature) clouds are formed in liquid or solid (crystal) phases. Clouds and their interaction with aerosol and their impact on local and global climate change encouraged NASA to create various projects to monitor and study clouds distribution, thickness, transportation, and observe transitional form of clouds or combination of several forms and varieties. Cloud-Aerosol Lidar and Infrared Pathfinder Satellite Observations (CALIPSO), Micro-pulse lidar (MPL), and Polarization Diversity Lidar (PDL is a lidar with two channels to detect two polarizations (Fhjii, 2005; Sassen, 1994) are famous lidars to

measure and detect clouds. Measuring cloud phase is based on Mie scattering theory, the backscattering from non-spherical (e.g., crystal phase) particles changes the polarization strongly, but the spherical (water droplets) particles do not (Sassen, K. et al. 1992; Sassen 1994). Both spherical and non-spherical cloud particles have a degree of depolarization ($\delta = I_{\perp} / I_{||}$) due to the multiple scattering effects, where $I_{\perp}, I_{||}$ are respectively the perpendicular and the parallel intensity components for the incident light. But non-spherical cloud particles degree of depolarization is greater than spherical particles depolarization ($\delta_{NS} \rangle \delta_{S}$). Polarization lidars are used to differentiate between cloud liquid and sold phases.

Fig 1.5, shows thin cloud signals that were provided by Hassebo et al. on January 10, 2006 using elastic Mie scattering stationary lidar at the CCNY site (longitude 73.94 W, latitude 40.83 N), at 355, 532, and 1064 nm wavelengths). The Figure also shows that the visible signal is penetrating the thin cloud successfully to higher altitude but the UV and IR signals failed due to their weakness. Comparing the thin cloud signal (Fig 1.5) with Fig 1.4 (thick cloud signal) we noted that, as a result of laser rapid attenuation while it is penetrating the cloud, in the thin cloud case the visible beam had a sufficient intensity to open a channel with high optical transparency to a higher altitude. In contrast, in Fig 1.4 the cloud was thick enough to prevent the laser beams from increasing their depth of penetration into the layer beyond the cloud. That explains the useless noisy (UV and IR) signals after the cloud ceiling (R= 4.5 km, and R= 11.5 km) in both cases, and for visible signal in the heavy cloud case even when the altitude is low (4.5 km). We noted also the PBL was shown clearly in both cases where the aerosol loading in New York City is always high.

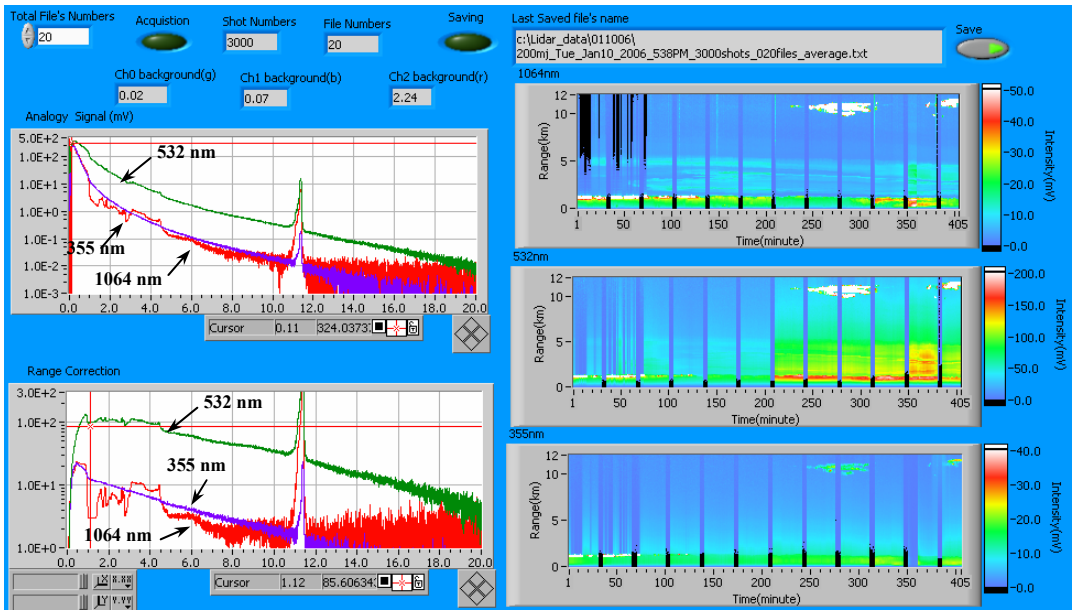

Figure 1.5 CCNY Lidar backscattering signals show thin cloud at 11km, Jan 10, 2006.

1.3.3.3 Velocity Lidar:

Doppler lidar can be used to provide the velocity of a target. When the light transmitted from the lidar hits a target moving towards or away from the lidar, the wavelength of the light reflected/scattered off the target will be changed slightly. This is known as a Doppler shift, hence Doppler lidar. If the target is moving away from the lidar, the returned beam will have a longer wavelength (sometimes referred to as a red shift). In other hand, if the target is moving towards the lidar the return light will be at a shorter wavelength (blue shifted). The target can be either a hard target or an atmospheric target. Thus the same idea is used to measure the wind velocity where, the atmosphere contains many microscopic dust and aerosol particles (atmospheric target) which are carried by the wind.

1.3.4 Lidar Types Based on Platform

1.3.4.1 Ground-based Lidar:

The PBL is the most important layer to study in the earth's atmosphere. Ground-based lidar (stationary in laboratories and mobiles in vehicles stations) is providing us with continuous, stable, and high resolution measurements of almost most of the lower atmosphere parameters. Ground-based lidar has made an important contribution in correcting the satellite data and complete the missing parts from the satellite images. A good example in chapter 7 of this thesis shows how the ground-based lidar signature is supporting the satellite operations to discriminate between cloud (big particle) and smoke plume (fine particle) and to determine the plumes height and thickness which the satellite cannot provide. The main drawback of ground-based lidar is the limitation of running during the bad weather (rain or snow) and the air control regulations issues.

1.3.4.2 Air-borne Lidar

Due to the uncertainty in validation of some remote sensing methodologies, particularly to detect cloud and measure its properties, from ground-based lidar stations, the in situ probes are useful techniques. Also the inaccessibility of the object of interest from the ground-based or space-based systems is the other reason to use air-borne lidars. The air-borne lidar platforms are air-craft, balloon, and helicopter. Applications of using air-borne lidars are to measure aerosol, clouds, temperature profile, metals in the mesopause, ozone in the stratosphere, wind, PSCs, H_2O, and on land, water depth, submarine track,

oil slicks, etc (Fhjii and Fukuchi 2005). One of the disadvantages of these platforms is the vibration problem.

1.3.4.3 Space-based Lidar:

The ground–based lidar provides a one spot at a unique moment measurement on the earth surface. The air-borne lidars are limited in one country or specific region as well as restricted by the weather or some times politic circumstances. The merit of the space-based lidar is to give global and/or continental images of the earth's atmosphere properties, structure, and activities. Certainly, space-based lidar needs very sophisticated, extremely expensive equipment, especially for remotely control the unattended operations and adaptive optics issue. In additional to the extremely important understanding of global scale phenomena (H_2O and carbon cycles, climate change, global warming, etc.) we have gained, we can reach an inaccessible areas by air-borne and/or ground-based stations such as oceans, north and south poles.

1.3.5 Lidar Configurations

Essentially, there are two basic configurations for lidar systems; monostatic and bi-static configurations.

1.3.5.1 Monostatic Lidar

Monostatic configuration is the typical configuration for modern systems. It is employed with pulsed laser source providing very good vertical resolution and beam collimation compared with the bi-static configuration. In this case, the transmitter and

receiver are at the same location, (see Fig. 1.6). Monostatic systems can be classified into two categories, coaxial systems and biaxial systems. Finally, the first used a monostatic system was in 1938.

1.3.5.2 Monostatic Coaxial Lidar

In the coaxial configuration the transmitter laser beam axis is coincident with the receiver's telescope Field Of View (FOV), i.e., coaxially as shown in Figure 1.6 (a). The main disadvantages in the coaxial lidar systems are the detector saturation problem that is occur once the lidar laser beam is shot, the unwanted signal that is detected from reflection of the transmitted light at the transmitter optics in the top of the receiver telescope, and the portion of the images - for short range - that are blocked by the secondary mirror.

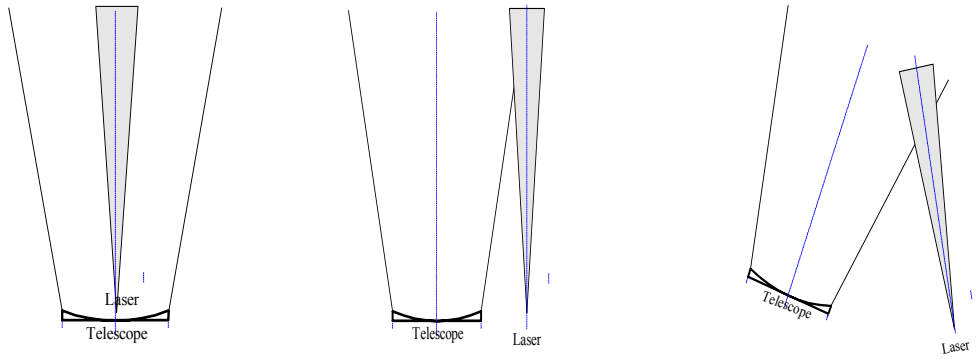

(a) Monostatic coaxial (b) Monostatic biaxial (c) Bi-static

Figure 1.6 Field of view arrangements for lidar laser beam and detector optics

1.3.5.3 Monostatic Biaxial Lidar

In the biaxial arrangement the transmitter and receiver are located adjacent to each other. Under this circumstance the laser beam field of view will intersect with the receiver telescope VOF beyond specific range *R*. This range can be predetermined based on the distance between the laser FOV and telescope FOV axes. In fact, this configuration is quite useful in preventing the receiver photomultiplier (PMT) detectors saturation from the near-filed laser radiations (coaxial lidar disadvantage). However, in a biaxial lidar system, the detected signals are negatively affected by the geometrical form factor (GF) at shorter range. This effect makes near field measurements impossible (Measures 1984). We proposed two techniques in this work to overcome the geometrical form factor problems (Hassebo, R. Agishev et al. 2004).

1.3.5.4 Bi-static Configuration

Bi-static lidar configuration is involving a considerable separation between the laser transmitter and the receiver subsystems. However, the usefulness of this configuration was originally used in supporting lidar with continuous wave (cw) laser source to overcome the prevention of measuring of the height variation of the density caused by cw laser (Fhjii and Fukuchi 2005). Currently, this arrangement is rarely used (Measures 1984).

As a summary of some lidar physical processes, their corresponding applications and objective of measurements are given in Table 1-2.

Table 1-2 Lidar classification and related research

Lidar Type Based On					
Process	**Wavelength**	**Objective**	**Platform**	**Configurations**	**Other**
Rayleigh Doppler	Elastic	Wind	Ground-based	Monostatic	Stratosphere Mesopause
Backscatter	inelastic	Cloud	Air-borne	Monostatic	Troposphere
Mie Backscatter Raman	single WL Multiple WL	Aerosol H_2O	Ground-based Space-based	Monostatic (Biaxial and Coaxial)	Troposphere Stratosphere
Raman	DIAL Raman DIAL	Ozone Humidity gaseous	Ground-based	Monostatic	Troposphere
Fluorescence		Wind /Heat flux	Air-borne	Monostatic	mesosphere

2 THE RESEARCH OBJECTIVES

2.1 Thesis Objectives

The primary objective of this study is to improve lidar signal-to-noise ratio (SNR) and hence extend attainable lidar ranges through reduction of the sky background noise (BGP), which dominates other sources of noise in daytime operations. This is particularly important for Raman lidar techniques where the Raman backscattered signal of interest is relatively weak compared with the elastic backscatter lidars. The background noise during daytime operations (mainly the solar radiations) can be reduced by applying different techniques and taking into account some lidar design considerations. These design techniques and considerations are applicable in any lidar type including ground base, airborne, and satellite lidars. The new design will be primarily used as an additional input to the advanced lidar systems in the City College of the City University of New York (CCNY/CUNY) operated by NOAA-CREST center and the remote sensing laboratory. Two approaches for reduction of sky background noise are considered:

1. Improvements in lidar SNR by optimization of the design of the lidar receiver were examined by a series of simulations. In this part of the research, I concentrated on biaxial lidar systems, where overlap between laser beam and receiver field of view (FOV) is an important aspect of noise considerations. The first optimized design evolved is a wedge shaped aperture (field stop). The implemented design is adaptive and range dependant. While this design has the virtue of greatly reducing background

light, it is difficult to implement practically, requiring both changes in area and position with lidar range. A second more practical approach, which preserves some of the advantages of the wedge design, was also evolved. This uses a smaller area circular aperture optimally located in the image plane for desired ranges and match to the receiver telescope parameters. Simulated numerical results for a biaxial lidar have shown that the best receiver parameters selection is one using a small circular aperture (field stop) with a small telescope focal length *f*, to ensure the minimum FOV that accepts all return signals over the entire lidar range while at the same time minimizing detected BGP and hence maximizing lidar SNR and attainable lidar ranges. The improvement in lidar SNR was up to 18 % with equivalent improvement in the required averaging time by 3.2%

2. A second approach for reduction of sky background noise, in this thesis, was to assess the impact and potential of a polarization selection technique to reduce sky background signal for linearly polarized monostatic elastic backscatter lidar measurements. Taking advantage of naturally occurring polarization properties in scattered sky light, a polarization discrimination technique was devised in which both the lidar transmitter and receiver track and minimize detected sky background noise while maintaining maximum lidar signal throughput. Lidar elastic backscatter measurements, carried out continuously during daylight hours at 532 nm, show that as much as a factor of $\sqrt{10}$ improvement in signal-to-noise ratio and the attainable lidar range up to 34% over conventional un-polarized schemes can be achieved. For vertically pointing lidars, the largest improvements, are limited to the early morning and late afternoon hours, while for lidars scanning azimuthally and in elevation at

angles other than vertical, significant improvements are achievable over more extended time periods with the specific times and improvement factors depending on the specific angle between the lidar and solar axes. In extensive field experiments, it was found that diurnal variations in SNR improvement sometimes show asymmetry with solar angle, which can be attributed to changes in observed relative humidity that modifies the underlying aerosol microphysics and observed optical depth.

A Second objective of this work was to utilize multiwavelength lidar techniques to separate plume and cloud particles. In addition, we discussed the measurements and analysis undertaken by our lidar systems in support of the NOAA-NEAQS and NASA-INTEX-NA experiments. To focus discussions, results which identify smoke plumes occurring over NYC on July 21 in support of MODIS imagery and validate the source using NOAA-HYSPLIT back trajectory analysis to originate the smoke plumes were shown. Much effort has been applied to obtaining larger continuous lidar data blocks to support both the NASA INTEX-NA and NOAA NEAQS experiment which is designed to study the transport of intercontinental chemical and aerosol transport. A description of the lidar system capabilities and processing algorithms used to process simultaneous backscatter lidar data with Aeronet CIMEL optical depth is presented. Finally, surface measurements from in-situ particle counters are presented which show no enhanced PM2.5 loading. This result is supported by lidar measurements, which confirm that nearly all of the aerosol plumes are located above the normal aerosol boundary layer (Jegou, M.Chanin et al.) showing that satellite measurements are often incomplete and is not useful to assess surface air quality.

2.2 Basic Lidar and System Assumptions for Thesis Work

The presented research study in this thesis is based on the following lidar parameters, hypothesis and assumptions:

- My experimental results were carried out with monostatic (coaxial in the lab and biaxial in the vehicle) elastic (Mie and Rayleigh) scattering lidars, for which the wavelength of backscattered observation is the same as that of the laser
- The lidars used were multi-wavelength lidars operating in the UV at 355, Vis. at 532, and IR at 1064 nm
- The atmospheric medium is assumed to be homogeneous over the range of overlap of the receiver field of view (FOV) and the laser beam i.e., $\xi(R)$ can be treated as a delta function, where the probability $\xi(R)$ is unity where the FOV of receiver optics overlaps the laser beam and zero elsewhere
- All experimental results have been taken during the daytime operations at the CCNY site, USA (longitude 73.94 W, latitude 40.83 N)
- The distribution of the laser irradiance across the target plane is assumed to be uniform over the area of illumination.
- The obstruction due to the telescope itself id not taken into account (the lidar systems used Cassegrainian or Newtonian Telescopes have some built in obstructions to the return signals)

- The laser propagation axis is assumed to be parallel to the receiver (telescope) optical axis. i.e., $\delta = 0$ in both lidars (coaxial and biaxial). Where $\delta = 0$ is the angle between the telescope and laser axes
- In the polarization studies, the single scattering regime was assumed
- The optical vertical axis is the z-axis, and the ground level axis is the x-axis, where the locations of the telescope primary mirror and the transmitted laser beam are at z =0 and x=0.
- A homogeneous aerosol approximation is used in which the aerosol extinction to backscatter ratio, $S_a = \alpha_a(R)/\beta_a(R)$ is a constant to determine the particle extinction coefficient.
- To calculate the particles extinction coefficient the lidar reference point was taken at the top of the lidar range ($R_{\max}$, where the particle backscatter coefficient $\beta_{aer}(R_{\max})$ is negligible compared to the known molecular backscatter value).
- In the polarization discrimination technique, clear sky conditions were assumed.
- The mean value of the photomultiplier tube (PMT) output power (P_d) was assumed to be proportional to the background power (BGP) (i.e., $\langle p_d \rangle \alpha BGP$), i.e., the detector operates in the shot noise limiting regime.

2.3 Thesis Outline

Chapter 1 covers the introduction. **Chapter 2** presents the research objectives. In **chapter 3,** the City University of New York lidar systems have been described in detail. These two systems were used to produce the experimental results. At the end of chapter 3, the lidar equation is discussed in detail for elastic and inelastic lidars. A general solution of the lidar equation is introduced.

Chapter 4 contains a description and scientific background of the geometric form factor and the overlap function between the receiver Field of View (FOV) and the transmitted laser beam and their effects on lidar measurements. Lidar simulations of a design to implement an efficient receiver aperture shape to reduce the background noise of biaxial lidar systems are presented. Numerical estimates are also given. I extend and simplified the implementation design for more practical applications, based on the telescope specifications in the end of **chapter 4**. A review of previous relevant research and its contribution to the problem of interest is presented. Also in chapter 4, the director noise considerations and their effects on lidar SNR were discussed.

In chapter 5, the potential and range of application and limiting factors of a polarization selection technique, recently devised by us are examined. The technique takes advantage of naturally occurring polarization properties of scattered sky light to minimize the detected sky background signal. It can be used in conjunction with linearly polarized elastic backscatter lidars to maximize lidar receiver SNR. In this approach, a polarization selective lidar receiver is aligned to minimize detected skylight, while the polarization of

the transmitted lidar signal is rotated to maintain maximum lidar backscatter signal throughput to the receiver detector, consequently maximizing detected signal to noise ratio. Results presented include lidar elastic backscatter measurements, at 532 nm which show as much as a factor of $\sqrt{10}$ improvement in signal-to-noise ratio over conventional un-polarized schemes. For vertically pointing lidars, the largest improvements are limited to symmetric early morning and late afternoon hours. For non-vertical scanning lidars, significant improvements are achievable over much more extended time periods, depending on the specific angle between the lidar and solar axes. A theoretical model that simulates the background skylight within the single scattering approximation showed good agreement with measured SNR improvement factors. Diurnally asymmetric improvement factors, sometimes observed, are explained by measured increases in PWV and subsequent modification of aerosol optical depth by dehydration from morning to afternoon. Finally, since the polarization axis follows the solar azimuth angle even for high aerosol loading, as demonstrated using radiative transfer simulations, it is possible to conceive automation of the technique. In addition, it is shown that while multiple scattering reduces the SNR improvement, the orientation of the minimum noise state remains the same.

In Chapter 6, Satellite measurements do not provide the vertical information needed to assess aerosol transport mechanisms. To supply this information, multiwavelength lidar measurements are needed to study the vertical structure of aerosol events. In support of NASA – INTEX and NOAA-NEAQS transport experiments we present lidar retrievals, which identify multiple stratified particulate plumes occurring over New York City on

July 21, 2006 in support of MODIS imagery. In particular, multiwavelength measurements at the City College of New York are used to determine the angstrom coefficient of the plumes that unambiguously identifies them as fine mode particulates and not cloud particles. A description of our lidar system capabilities and processing algorithms used to process simultaneous backscatter lidar measurements with Aeronet CIMEL Optical Depth (τ or OD) data is presented and back-trajectory analysis is used to confirm the source of the plumes to be from Alaskan wild fires. Finally, surface measurements from in-situ particle counters are presented and show no enhanced PM2.5 loading. This result is supported by lidar measurements, which confirm that nearly all of the aerosol plumes are located above the normal aerosol boundary layer (Jegou, M.Chanin et al.) showing that satellite measurements are often incomplete and is not useful to assess surface air quality. In particular, we show that high PM2.5 events are triggered from more local sources such as the Ohio Basin and climatological conditions which drive the pollution to the surface.

Finally, Chapter 7 presents a conclusions and summary with future research suggestions.

3 THE CUNY LIDARS AND LIDAR EQUATION

3.1 Experimental Approach: CUNY Lidars Specifications

The City University of New York (CUNY) has developed two ground-based lidar systems, one mobile and one stationary, that operate at multiple wavelengths for monostatic elastic backscatter retrievals of aerosol and cloud characteristics and profiles. Lidar measurements are performed at the Remote Sensing Laboratory of the City College of New York (CCNY). The lidar systems are designed to monitor enhanced aerosol events as they traverse the eastern coast of the United States, and form part of the National Oceanic and Atmospheric Administration's (NOAA's) Cooperative Remote Sensing Center (NOAA-CREST) Regional East Atmospheric Lidar Mesonet (REALM) lidar network. The lidar measurements reported in this thesis involve geometric form factor considerations and design (Chapter 4), and the experimental polarization discrimination technique (Chapter 5) and were carried out using the mobile (in vehicle) elastic monostatic biaxial backscatter lidar system at the CCNY site (longitude 73.94 W, latitude 40.83 N), at 355nm, 532 nm, and 1064 nm wavelengths. The lidar measurements reported in the Introduction (Chapter 1) and in plume-cloud discrimination work in support of NASA and NOAA experiments (Chapter 6) were carried out using the stationary (CCNY remote sensing laboratory) elastic monostatic coaxial backscatter lidar system at the same CCNY location. Chapter 3 presents, in section 3.1.1, the experimental set up and details specifications of the stationary coaxial lidar. Section 3.1.2 describes the

second multiwavelength mobile lidar system. In section 3.2 theoretical lidar formulations and solutions are presented.

3.1.1 Stationary Rayleigh /Mie-Raman Lidar

The experimental apparatus for the stationary CCNY remote sensing laboratory lidar is shown in Figure 3.1. This lidar is a multiwavelength Mie-Raman lidar which was designed for investigation of tropospheric aerosol and water vapor vertical profiles with a three wavelength (355, 532, 1064 nm for Mie scattering) ND: YAG laser. The lidar outputs are linearly polarized and has a 0.6 cm beam diameter, 0.5 mrad divergence, pulse duration of 3 ns (at 355nm and 532 nm), and 3.5 ns (for 1064 nm). The pulse repetition rate is between 10 Hz to 50 Hz; in this research I used pulses repetition rate of 50 Hz.

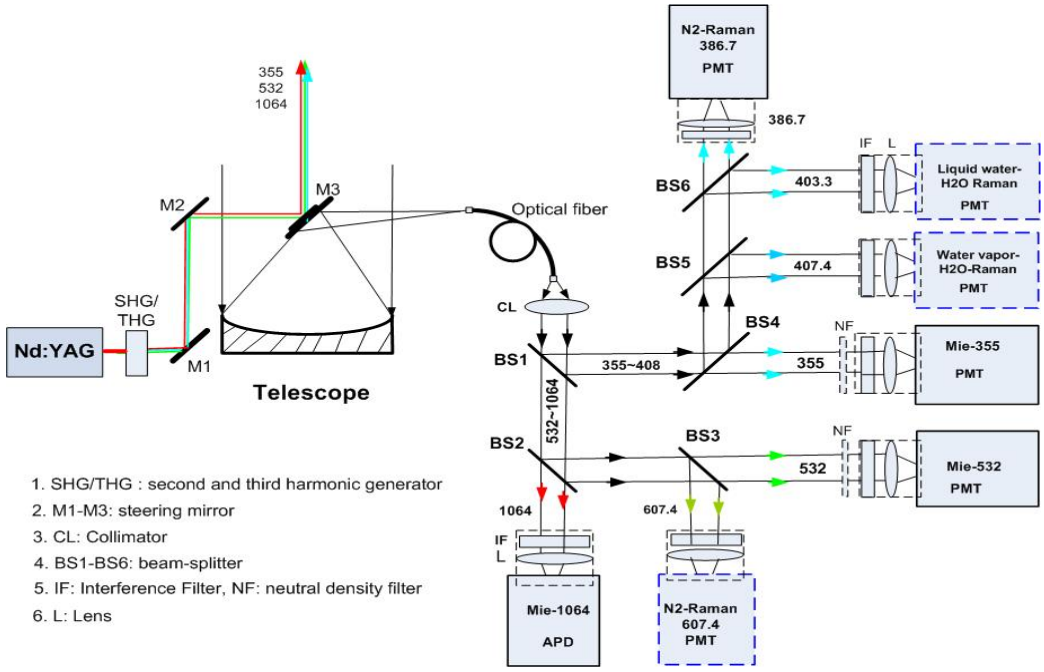

Figure 3.1 Schematic diagram of the multi-wavelength Mie-Raman stationary lidar

The receiver telescope primary mirror is a 20” (508 mm) diameter Newtonian telescope with a focal length of 70” (1.77 m) coupled to Hamamatsu photomultiplier detectors (PMT R11527P for visible, PMT R2693 for ultraviolet) in addition to avalanche photodiode (APD) for 1064. Optical Andover filters with 1 nm bandwidth were placed in the front of the detectors. These filters are centered at 355 nm, 532 nm, and 1064 nm wavelength. Lidar transmitter and receiver subsystem parameters are listed in Table 3.1.

Table 3-1 Stationary lidar system specification

Transmitter		**Receiver**	
Laser	Q-Switched (An optical on-off switch) Nd: YAG Infinity 40-100	**Telescope Aperture**	Newtonian telescope 20 “ (50.8 mm)
Wavelength	1064, 532, 355 nm	**Focal length**	70 “ (1778 mm)
Energy/pulse	500 mJ at 1064 nm 250 mJ at 532 nm 200 mJ at 355 nm	**Detectors** **532 nm** **355 nm** **1064 nm**	Hamamatsu PMT: R11527 P PMT R2693 P APD
Pulse Duration	3.5 ns at 1064 nm 3 ns at 532, 352 nm	**Data Acquisition**	LICEL TR 40-160
Repetition Rate	10- 50 Hz	**Photon Counting**	LICEL TR 40-160
Harmonic Generation	Quanta_Ray HG-1		

Data were acquired in both analog and photon counting (PC) modes. Typically the data that were obtained in the PC mode averaged 600 pulses over a 1 min interval using a Licel 40-160 transient recorder with a 40 MHz sampling rate, for analog-to-digital conversion, and a 250 MHz photon counting sampling interval. The connection and the setup of Licel, as a powerful data acquisition tool, are shown in Figures 3.2 and 3.3.

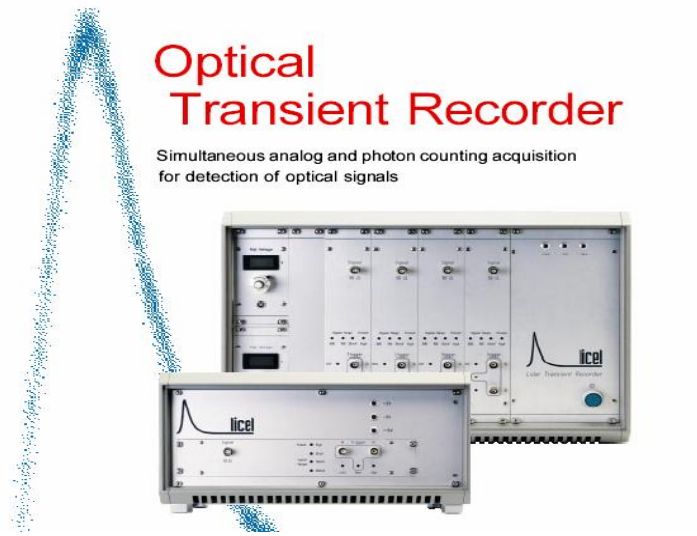

Figure 3.2 Licel data acquisition: 5 channels

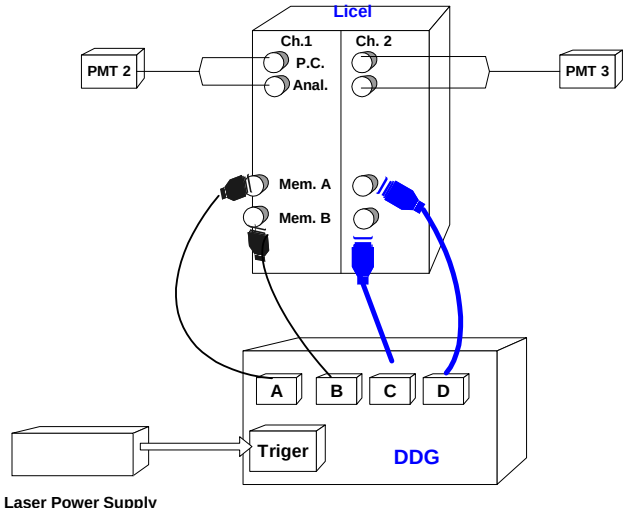

Figure 3.3 Licel connections

3.1.2 Mobile Rayleigh -Mie Lidar

CCNY mobile (in-vehicle) lidar is an elastic monostatic biaxial backscatter lidar system located, for experiments, at the City College of New York (CCNY longitude 73.94 W, latitude 40.83 N). The lidar transmitter is a 10-Hz Q-Switched Nd: YAG_ MDL Continuum Surelite laser. The transmitted wavelengths are UV at 355 nm, Visible at 532 nm, and near IR at 1064 nanometers. The lidar output is linearly polarized and has a 0.5 cm beam diameter, 0.5 mrad divergence. In this dissertation (Chapter 6) the visible channel at 532 nm is used with pulse energies of 100 mJ and a pulse width of 3 ns. A ½ wave plate rotates the polarization of outgoing signal to match desired receiver polarization. Figure 3.4 shows the arrangement used to implement the measurements.

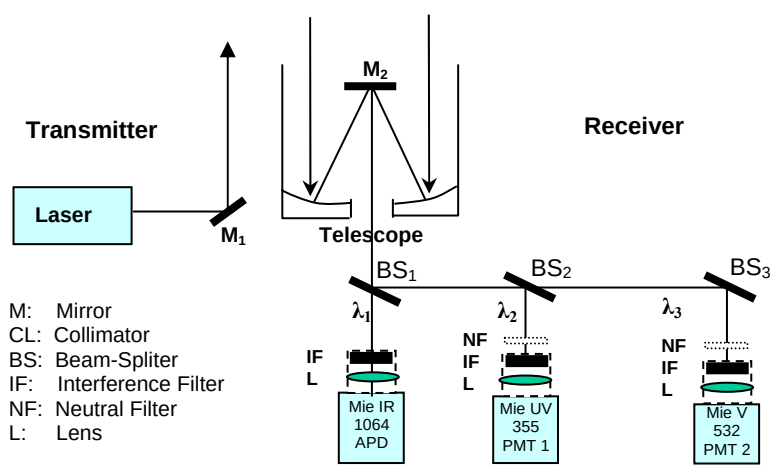

Figure 3.4 CCNY schematic diagram of the multi-wavelength Mie lidar (mobile system)

The receiver was a 14” (355.6 mm) diameter CM-1400 Schmidt-Cassegrian telescope with a focal length of 153.9” (3910 mm). The lidar return from the receiver telescope is detected, by a photo-multiplier (PMT R11527P) with a 1 nm bandwidth optical filter

(532F02-25 Andover), centered at the 532 nm wavelength. For extended ranges, data is acquired in the photon counting (PC) mode. For the polarization technique this is (Chapter 6), typically averaging 600 pulses over a one minute interval, using the Licel 40-160 transient recorder with 40 MHz sampling rate for A/D conversion and a 250 MHz photon counting sampling interval. Mobile lidar characteristics are shown in details in Table 3.2.

Table 3-2 Mobile lidar system specification

Transmitter		**Receiver**	
Laser	Q-Switched Nd: YAG Continuum Surelite ll -10	**Telescope Aperture**	CM_1400 Schmidt Cassegrian telescope 35.56 mm
Wavelength	1064, 532, 355 nm	**Focal length**	3910 mm
Energy/pulse	650 mj at 1064 nm 300 mj at 532 nm 100 mj at 355 nm	**Detectors** **532 nm** **355 nm** **1064 nm**	Hamamatsu PMT: R11527 P PMT: R758-10 APD
Pulse Duration	7 ns at 1064 nm	**Data Acquisition**	LICEL TR 40-160
Repetition Rate	10 Hz	**Photon Counting**	LICEL TR 40-160
Harmonic Generation	Surelite Double (SLD) Surelite Third Harmonic (SLF)		

The setup used to implement the polarization-tracking scheme with this lidar is shown in detail in Chapter 6. For the reader's convenience this lidar arrangement is briefly summarized below.

To select the polarization of light entering the detector, a polarizing beam splitter is located in front of the collimating lens that is used in conjunction with a narrow band filter (alternatively, dichroic material polarizers were also used). This polarizing beam splitter (analyzer) is then rotated to minimize the detected sky background light P_b. On the transmission side, the half wave plate at the output of the polarized laser output is then used to rotate the polarization of the outgoing lidar beam so as to align the

polarization of the backscattered lidar signal with the receiver polarizing analyzer and hence maximize its throughput (i.e., at the minimum P_b setting). This procedure was repeated for all measurements, with appropriate adjustments being made in receiver polarization analyzer alignment and a corresponding tracking alignment in the transmitted beam polarizations to adjust for different solar angles at different times of the day, and hence minimize the detected P_b and maximize lidar SNR. Cross polarized extinction ratios on the receiver analyzer were approximately 10^{-4} . At present, the rotation of the polarization angle is done manually, but as we will see in Chapter 6, the process can be automated by recognizing that the polarization rotation angle can be matched directly to the solar azimuth angle, which may be pre-computed.

3.2 Retrieval of Lidar Returns

In general, the form of the lidar equation depends upon the kind of interaction invoked by the laser radiation. Neglecting the multiple scattering among scatters wavelength shift between the transmitter and the receiver (inelastic scattering), and similar to the derivation of the radar equation, the lidar return signal, the backscattered mean power received from range R, $P(\lambda_L, \lambda\ , R)$ of lidar system can be written as:

$$P(\lambda_L, \lambda\ , R) = P_L \frac{A_o}{R^2} \frac{c\tau_L}{2} \xi(\lambda_L)\xi(R)\beta(\theta, \lambda_L, \lambda\ , R) \times \exp\left(-\int_0^R \alpha(\lambda_L, R^{'})dR^{'}\right) \times \exp\left(-\int_0^R \alpha(\lambda\ , R^{'})dR^{'}\right) \quad \textbf{(3.1)}$$

Where, $P(\lambda_L, \lambda, R)$ is the total scatter laser power registered by the lidar receiver detector from distance R if the transmitted light of wavelength λ_L, and the wavelength of the backscatter light is λ. This power depends on two main parameters:

- The backscatter properties of the atmosphere whether particulate or molecular backscatter (which disperse , shift light wavelength, and/or depolarize the laser light)
- The lidar system parameters (mirrors, filters, telescope, and optics specifications, alignments, geometric form factor, and overlap function)

P_L: represents the average power in the laser pulse, A_o/R^2 describes the solid angle of the receiver optics (A_o is the area of the telescope primary mirror),

$\xi(\lambda)$: denotes the receiver's spectral transmitter factor, (losses in mirrors, polarizers, prism, filters, detector efficiency, etc.). $\xi(\lambda)$: is independent on range, but wavelength dependent.

$\xi(R)$: is the geometric factor (telescope Field Of View (FOV)-laser beam overlap function). $\xi(R)$: depends on the distance (*R*), but wavelength independent.

$$0 \le \xi(R) \le 1 \tag{3.2}$$

It is well known that light propagating in a random medium undergoes scattering (Ishimaru 1997; José M. Bioucas Dias, Leitão et al. 2004). $\beta(\theta, \lambda_L, \lambda, R)$: is the volume backscatter coefficient, θ is the scattering angle. For the backscattered signal the scattering angle $\theta = \pi$, and we will henceforth simply use $\beta(\lambda_L, \lambda, R)$ to represent the backscattering coefficient which, can be written as:

$$\beta(\theta, \lambda_L, \lambda, R) = \beta(\pi, \lambda_L, \lambda, R) = \beta(\lambda_L, \lambda, R) \tag{3.3}$$

For simple elastic scattering ($\lambda_L=\lambda$), there is no wavelength shift, so the backscattering coefficient can be written as: $\beta(\lambda, R)$

The spatial length of the laser pulse is $c\tau_L$

(*c*: is speed of light, $\tau_L = t_1 + t_2$ is Laser pulse rectangular duration)

Where t_1 is the pulse rising time, and the falling time is t_2, ($t_1>0$, and $t_2>0$), we noted that, the light reaches the receiver detector at time *t* is originated from the interval

$$\frac{(t - t_1)c}{2} < R < \frac{(\tau_L)c}{2} \tag{3.4}$$

The delay time between any two successive pulses (Δt) must be greater than $\frac{R_{\max} c}{2}$,

where R_{max} is the maximum range at which the lidar data can be collected (Fhjii and Fukuchi 2005).

Also, light propagating in a random medium suffers attenuation (Ishimaru 1997; José M. Bioucas Dias, Leitão et al. 2004). This attenuation (Atmospheric transmittance, $T(\lambda\ ,R)$) can be divided into two terms:

1. Attenuation factor from the transmitter to the target object between lidar site (*R=0*) and the object site at range *R*:

$$T_L(\lambda_L, R) = \exp\left(-\int_0^R \alpha(\lambda_L, R')dR'\right) \quad \textbf{(3.5)}$$

2. Attenuation factor for the backscattering from the target (at *R*) to the receiver:

$$T(\lambda\ ,R) = \exp\left(-\int_0^R \alpha(\lambda, R')dR'\right) \quad \textbf{(3.6)}$$

$\alpha(\lambda_L, R)$ and $\alpha(\lambda, R)$: are the atmospheric extinction coefficients for both transmitter and return signals, respectively. Similar to the backscatter coefficient, for elastic scattering, i.e., $\lambda_L=\lambda$, the extinction coefficient can be written as:

$$\alpha(\lambda_L, R) = \alpha(\lambda, R) = \frac{dI}{I} \quad \textbf{(3.7)}$$

Where *I*: is the laser beam intensity.
Equations 3.5, 3.6 can be written as:

$$\exp\left(-\int_0^R \alpha(\lambda_L, R')dR'\right) = \exp\left(-\int_0^R \alpha(\lambda\ , R')dR'\right) \quad \textbf{(3.8)}$$

Then the total attenuation factor in the elastic lidar equation is:

$$T^2(\lambda, R) = \exp\left(-2\int_0^R \alpha(\lambda, R')dR'\right) \quad \textbf{(3.9)}$$

Both $\beta(\lambda, R)$ and $\alpha(\lambda, R)$ are the backscatter and extinction cross section per unit volume of air, respectively. Therefore, the suitable unites for $\beta(\lambda, R)$ are (cm^2. sr^{-1}/cm^3) or ($cm^{-1}.sr^{-1}$). Also, $\alpha(\lambda, R)$ unite is (cm^2/cm^3) or (cm^{-1}).

Commonly, the elastic lidar equation is written as:

$$P(\lambda, R) = P_L \frac{A_o}{R^2} \frac{c\tau_L}{2} \xi(\lambda)\xi(R)\beta(\lambda, R) \times \exp\left(-2\int_0^R \alpha(\lambda, R')dR'\right) \quad \textbf{(3.10)}$$

Clearly, the backscatter and the extinction coefficients $\beta(\lambda, R)$ and $\alpha(\lambda, R)$ are the two parameters in the lidar equation that relate the return signal with the atmosphere properties.

3.2.1 Solving Lidar Equation (Retrieval Method)

Measurement of the backscatter and extinction coefficients in elastic-backscatter lidar was a significant goal for a lot of publications (Fernald, B. Herman et al. 1972; Klett 1981; Fernald 1984; Klett 1985; Sasano, E. Browell et al. 1985; Carswell 1990; Kunz and Leeuw 1993; Lentz, Alfred W. Cooper et al. 1994; V.Kovalev and Moosmüller 1994)

The two variables containing the relevant geophysical information:

Backscatter coefficient: $$\beta(\lambda, R) = \frac{N(R)}{d\sigma(\lambda, \theta)/d\Omega} \quad \textbf{(3.11)}$$

Extinction coefficient: $$\alpha(\lambda, R) = N(R)\sigma(\lambda) \quad \textbf{(3.12)}$$

Where: *N(R)*: is the volume number concentration

$d\sigma(\lambda, \theta)/d\Omega$: is the backscatter cross section

$\sigma(\lambda)$: is the extinction cross section

In this study, I considered two distinct classes of scatterers, molecules (Rayleigh) and the aerosol (Mie). The total backscatter and extinction coefficients ($\beta_{tot}(\lambda, R)$, $\alpha_{tot}(\lambda, R)$) for elastic lidar can be expressed by:

$$\beta_{tot}(\lambda, R) \equiv \beta_a(\lambda, R) + \beta_m(\lambda, R) \quad \textbf{(3.13)}$$

$$\alpha_{tot}(\lambda, R) \equiv \beta_a(\lambda, R) + \beta_m(\lambda, R) \quad \textbf{(3.14)}$$

Where, the subscripts (a), and (m) are for aerosol (Mie) and molecular (Rayleigh) scatter, respectively. Under the assumption that the molecular components can be retrieved accurately, the lidar equation provides a single relationship between two independent quantities $\beta_a(R)$ and $\alpha_a(R)$ and in most LIDAR studies, it is assumed that the aerosol extinction to backscatter ratio is:

$$S_a = \alpha_a(\lambda, R) / \beta_a(\lambda, R) \quad \textbf{(3.15)}$$

S_a: is a constant (homogeneous aerosol approximation) which can be estimated either from data tables or estimated from other data sources. Finally, the calibration constant is hard to determine directly from the physical geometry and instrumentation and therefore an absolute measure of one of the aerosol coefficients along the lidar path is needed. Molecular extinction to backscatter ratio is independent of wavelength and can be approximated for a standard atmosphere and expressed as (Klein 1970):

$$\left(S_m = \frac{\alpha_{\mathrm{m}}(R)}{\beta_{\mathrm{m}}(R)} = \frac{8\pi}{3} \right) \quad \textbf{(3.16)}$$

Since the molecules can be treated as being isotropic. We can use the empirical formula for molecular optical depth as function of wavelength (in nm) (Klein 1970):

$$\tau_m = C_1 \lambda_n^{-4} \left(1 + C_2 \lambda_n^{-2} + C_3 \lambda_n^{-4}\right) \tag{3.17}$$

Where:

$$\begin{aligned} \lambda_n &= \frac{\lambda}{550}, \\ \mathrm{C}_1 &= 0.09364, \\ \mathrm{C}_2 &= 0.0374, \\ \mathrm{C}_3 &= 0.00142 \end{aligned} \tag{3.18}$$

We derive $\beta_m(R)$ and $\alpha_m(R)$.

$$\alpha_m(R) = \tau_m \frac{P(R)/T(R)}{\int_0^R \frac{P(R)}{T(R)} dR} \tag{3.19}$$

Using these derived values we are ready to do the Lidar inversion technique to retrieve the aerosol optical properties. Therefore, if we assume that the molecular optical coefficients are known (a valid assumption), the solution depends on the following additional information:

- The aerosol backscattering coefficient $\beta_a(\lambda, R)$ which can be estimated if the molecular profile (aerosol free region) is known. This makes slant measurements undesirable and will require vertical soundings and a method of determining when an aerosol free region is considered.

- A value for S_a. We show how this can be estimated if we have the total aerosol optical depth τ which we get from sun photometry.

We still have two unknowns in the lidar equation, namely $\beta_a(R)$ and $\alpha_a(R)$ the particle backscatter and extinction coefficients, respectively. Even with the previous assumption, the exact value of aerosol ratio S_a (Eq. 3.15) is unknown since it depends on the physical and chemical properties of the atmospheric particles. Simultaneously coupling data from measurements of the total optical depth using the sun spectrophotometer greatly improves the retrieval of vertical profile aerosol optical parameters, since it makes the choice of the lidar ratio more precise.

A solution under the assumed conditions can be written as (Fernald 1984):

$$\beta_a(R)+\beta_m(R)=\frac{\overline{P}(R)\exp\left[-2(S_m-S_a)\int_R^{R_{\max}}\beta_m(R')dR'\right]}{\left(\frac{\overline{P}(R_{\max})}{\beta_{tot}(R_{\max})}\right)+2S_a\int_R^{R_{\max}}\overline{P}(R')\exp\left[-2(S_m-S_a)\int_{R'}^{R_{\max}}\beta_m(R'')dR''\right]dR'} \quad \textbf{(3.20)}$$

where $R_{\max}$: is chosen to be the highest point in the lidar range with sufficiently high signal-to-noise ratio (calibration range is determined as the height region or point where Rayleigh scattering dominates the measured signal).

And $\overline{P} \equiv PR^2$ is the range corrected backscattered power. Note that this solution fixes the boundary condition at the top of the lidar range and seeks a solution by back-integration that is more stable than the corresponding forward solution.

Therefore, given the following data set $\{S_a, \beta_a(R_{\max})\}$, the lidar signal can be inverted to obtain both $\beta_a(R), \alpha_a(R)$. Therefore, an estimate of the data set $\{S_a, \beta_a(R_{\max})\}$ is required and the approach we use to analyze the lidar signals and estimate the optical coefficient error is outlined below.

A set of reasonable ratios of aerosol backscattering to molecular backscattering coefficients (AMR) at the reference point ($R_{\max}$) is assumed.

$$AMR \equiv \frac{\beta_a(R_{\max})}{\beta_m(R_{\max})} \tag{3.21}$$

It is difficult to determine accurately the volume extinction coefficient of aerosol, where we can not separate Mie form Rayleigh signals. In this case, we have to assume a set of reasonable aerosol ratios $S_{\min} < S_a < S_{\max}$, where $S_a(R) = \frac{\alpha_a(R)}{\beta_a(R)}$, to solve the lidar equation for the aerosol extinction coefficient ($\alpha_a(R)$). This assumption is impossible to estimate reliably; since the aerosol lidar ratio $S_a(R)$ is varied strongly with the altitude ($S_{aer}(R)$ varied between 20 and 100) due to the relative humidity increase with the altitude (S ratio depends on chemical, physical and morphological properties of the particles which are relative humidity dependent). As shown in Table 3-3 (Kovalev and Eichinger 2004), big variations of aerosol typical lidar ratio for different aerosol types have been determine at 532 nm wavelength using Raman lidar

Table 3-3 Different aerosol types and the corresponding aerosol lidar ratio $S_a(R)$

Aerosol (particle) types	**aerosol lidar ratio $S_a(R)$ (sr)**
Marine Particle	20-35
Saharan dust	50-80
Less absorbing urban particles	35-70
Absorbing particles from biomass burning	70-100

It should be noted that above the boundary layer, the aerosol concentration decreases substantially and the ratio can usually be bounded by some small number less than one with tighter constraints obtained by increasing the lidar range

1. The aerosol profiles $\beta_a(R), \alpha_a(R)$ for each set of parameters, is calculated.
2. For each parameter set, the optical depth over the entire lidar range including the molecular contribution above the lidar range

$$\tau_L(S, AMR) = \int_0^{R_{\max}} (\alpha_a(R') + \alpha_m(R'))\, dR' + \int_{R_{\max}}^{\infty} \alpha_m(R') dR' \qquad \textbf{(3.22)}$$

is calculated.

3. The admissible profiles are those that simultaneously satisfy the constraints $AMR_{\min} \le AMR \le AMR_{\max}$ and $\tau_{\min} \le \tau_L \le \tau_{\max}$ estimated from sun-photometry measurements.

4. For each range *R*, a histogram can be constructed for both optical coefficients providing a reasonable estimate of both the aerosol extinction and backscatter profiles for each range.

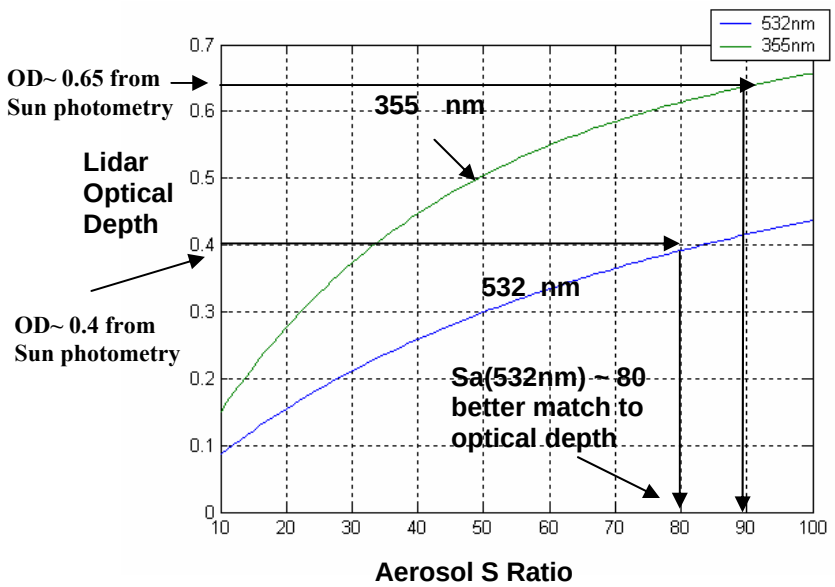

Figure 3.5: Example of integrated optical depth, using Fernald method, as function of S_a

While this procedure accounts for atmospheric variability, the effects of background and detector noise should also be included into the statistics. It should also be noted that in the body of this work, only the mean value of the optical data coefficients are displayed. To verify the algorithm against other processing methods for consistency, we compare the Fernald algorithm to an iterative algorithm (Russell et al) implemented at NASA Langley and note the agreement between the two methodologies.

4 LIDAR RECEIVER DESIGN PARAMETERS: IMPACTS AND SELECTION

Introduction

Improvements in lidar SNR by optimization of the design of the lidar receiver were examined by a series of simulations. In this part of the research, I concentrated on biaxial lidar systems, where overlap between laser beam and receiver field of view (FOV) is an important aspect of noise considerations. The first optimized design, **Section 4.1**, evolved is a wedge shaped aperture (field stop). The implemented design is adaptive and range dependant. While this design has the virtue of greatly reducing background light, it is difficult to implement practically, requiring both changes in area and position with lidar range. A second more practical approach, **Section 4.2**, which preserves some of the advantages of the wedge design, was also evolved. This uses a smaller area circular aperture optimally located in the image plane for desired ranges and match to the receiver telescope parameters. Simulated numerical results for a biaxial lidar have shown that the best receiver parameters selection is one using a small circular aperture (field stop) with a small telescope focal length *f*, to ensure the minimum FOV that accepts all return signals over the entire lidar range while at the same time minimizing detected BGP and hence maximizing lidar SNR and attainable lidar ranges. The improvement in lidar SNR was up to 18 % with equivalent improvement in the required averaging time by 3.2%. In **Section 4.3**, the impact of the receiver detector parameters on lidar SNR improvements is discussed.

4.1 Geometric Factor Effect in Lidar

The complexity of measurements of aerosols characteristics, air pollution, and meteorology can be approached using multiwavelength lidar systems. At our remote sensing lab at the City College of New York in addition to the tow backscatter Lidar systems (stationary and mobile), we are currently developing Raman capabilities. However, due the weakness of the lidar return signal, the background noise elimination is very important. Full overlap between laser beam and telescope field-of-view (FOV) is one of the most significant parameter to reduce the background sun radiation. Numerical results show that significant improvement in background rejection can occur if the receiver aperture is designed properly, and if this design is range dependant. The results demonstrate the effects of variations of the telescope's field of view, laser beam divergence, and the receiver aperture misalignment. To improve lidar range given a specific laser type and basic optical detection scheme, two strategies can be pursued: (1) increasing the laser output power, (2) improving the detector and/or its associated optics. Halldorsson and Langerholc in their paper (1978) proposed the Geometric from Factor (GF) sensitivity due to the receiver and transmitter optics misalignment, and laser beam divergence theoretically. That was the reason in 1979 for Y. Sasano *(Sasano, H. Shimizu et al. 1979)* to introduce an experimental method to determine the geometrical form factor. He considered that the aerosol distribution is homogenous which leads to a spatially homogeneous volume backscattering coefficient $\beta(R)$, and an atmospheric transmission $T(R) = 1$. On the other hand, Ravil et al. on 2002 (Agishev and Comeron 2002) defined a spatial filtering efficiency J of the lidar receiving subsystem, which allowed us to compare

different receiving subsystem designs from the point of view of their ability to reject the background radiations.

However, most of previous publications have discarded the laser radar observations of aerosols for short distances because of the unknown factor of insufficient overlapping between the transmitting laser beam and the FOV of the receiving optics. These intersect at some distant point so that the ratio of the overlapping area to the laser beam cross section is small at short distances. The geometric factor is very sensitive to misalignment in the optical system (Sasano, H. Shimizu et al. 1979) making near field observations impossible. In practice usually a larger receiver field of view is needed to ensure collection of the useful signals, which results in an increase of the background radiation reaching the photodetector (Measures 1984; Agishev and Comeron 2002). However, it is possible to design a unique aperture that can be effective for desired ranges and permits subtraction of the background radiation while keeping the backscatter laser signal becomes feasible. This design optimizes the SNR and attainable range of lidar systems.

4.1.1 Geometric Form Factor Definition

For common monostatic lidars the assumption that the fields of view for signal and background radiation are the same is not sufficiently correct (Agishev and Comeron 2002). The Geometric form Factor (GF) or the overlap factor is the overlap of the area of laser irradiation with the field of view (FOV) of the receiver optics (i.e., telescope and aperture) at certain altitude R. Figures 4.1, 4.2 show that the overlap area for the monostatic biaxial lidar. That appears in lidar equation below as $\xi(R)$:

$$P(\lambda_L, R) = P_L \frac{A_o}{R^2} \xi(\lambda_L) \beta(\lambda_L, R) \xi(R) \frac{c\tau_L}{2} \exp\left(-2\int_0^R k(\lambda_L, R)\, dR\right) \quad \textbf{(4.1)}$$

Assumptions for the above equation, are that elastic (Mie or Rayleigh) scattering, prevails where the wavelength of observation is the same as that of the laser wavelength, also assume the medium is homogeneous over the zone of overlap between FOV and the laser beam (i.e., we can treat $\xi(R)$ as a delta function, where the probability $\xi(R)$ is unity where the FOV of receiver optics overlaps the laser beam and zero elsewhere). Consider the temporal shape of the laser pulse by a rectangle of duration of τ_L .The distribution of the laser irradiance across the target plane is assumed to be uniform over the area of illumination.

Where:

$P(\lambda_L, R)$ = the total scatter laser power received from a range R at wavelength of λ_L

$P_L = \frac{E_L}{\tau_L}$: The average power in the laser pulse (E_L the output energy of the laser pulse)

$\frac{A_o}{R^2}$: The solid angle of the receiver optics (A_o is the area of the telescope objective mirror)

$\xi(\lambda_L)$: The receiver's spectral transmitter factor

$\beta(\lambda_L, R)$: The volume backscatter coefficient

$\xi(R)$: Geometric form Factor

$c\tau_L$: Laser pulse length (c is speed of light, τ_L is laser pulse rectangular duration)

$k(\lambda_L, R)$: Atmospheric attenuation coefficient at the laser wavelength

The above geometric form factor assumptions are reasonable for long-range measurements. But for shorter range is highly questionable (Measures 1984). However, cognizant of theses constraints, we can write:

$$P(\lambda_L, R) = P_L \frac{A(R)}{R^2} \xi(\lambda_L) \beta(\lambda_L, R) \frac{c\tau_L}{2} e^{-2\int_0^R k(\lambda_L, R) dR} \quad \textbf{(4.2)}$$

The only different between Eq. (4.1) and Eq. (4.2) that, *A(R)* has replaced the product of $A_o \xi(R)$

Where *A(R)* is the effective telescope area

$$A(R) = \frac{A_0}{\pi L^2(R)} \int_{r=0}^{r_T} \int_{\psi=0}^{2\pi} \xi(R, r, \psi) F(R, r, \psi) r dr d\psi \quad \textbf{(4.3)}$$

$A_o = \pi * t_o^2$

$L(R) = \sqrt{L_0 + \theta^2 R^2}$ is the laser beam radius at rang of R

L_0 : the laser output aperture radius

θ : The laser's half divergence angle

$t_T(R) = t_0 + \phi R$: is the FOV cross section radius of the receiver optics at rang R

t_o: effective radius of telescope mirror

ϕ : is the receiver optics half opening angle

r : is the radial displacement of the point of interest in the target plane from the telescope axis

ψ : is the corresponding azimuthally angle from a vertical plane passing through the axis.

$\xi(R,r,\psi)$: is geometric probability function

$F(R,r,\psi)$: is laser irradiance distribution function

Then the GF can be expressed as:

$$\xi(R) = \frac{1}{\pi L^2(R)} \int_{r=0}^{t_T} \int_{\psi=0}^{2\pi} \xi(R,r,\psi) F(R,r,\psi) r dr d\psi \quad \textbf{(4.4)}$$

Assuming no obstruction on the telescope (actually, most of the lidar systems used Cassegrainian or Newtonian telescopes, which are designed with some obstructions of the return signals), also assuming that a uniform distribution of the laser beam at the target area. Then we can deal with $\xi(R)$ as a delta function and we can simplify Eq. (3.4) to:

$$\xi(R) = \frac{\Gamma\{t_T(R); L(R); d(R)\}}{\pi L^2(R)} \quad \textbf{(4.5)}$$

where: Γ is the overlap area function.

$d = b_o + R\delta$: d is the distance between the laser and telescope optical axes at altitude R shown in Fig. 4.1 below, b_o is the distance between the laser and telescope optical axes at $R=0$ as shown in Fig. 4.3

δ : is the angle between the telescope and laser axes. In our system $\delta = 0$

That means, if we calculate the overlap area, we calculate the geometric factor GF [$\xi(R)$]. Therefore, if we keep the overlap area maximum, that leads to maximize GF, i.e., $\xi(R) \approx 1$ for 100% overlap.

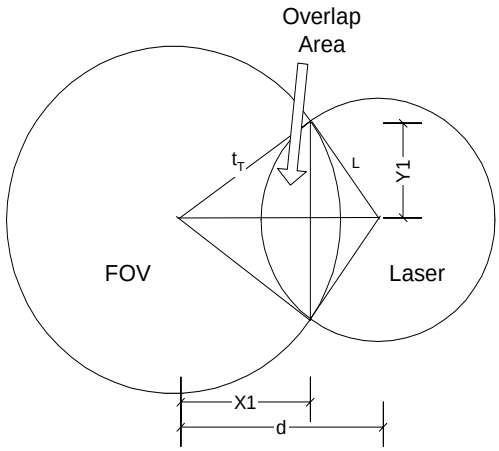

Figure 4.1 Overlap area calculation

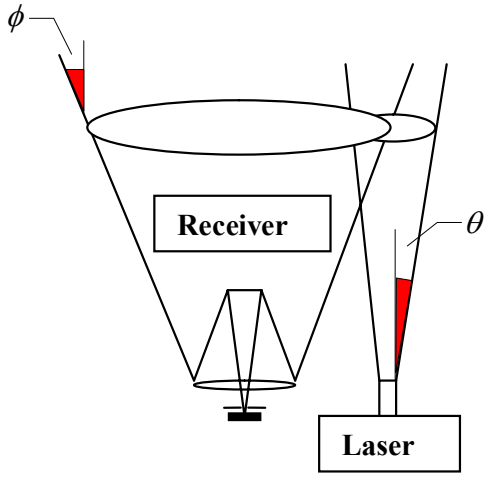

Figure 4.2 Schematic diagram of elastic biaxial lidar

4.1.2 Procedures and Calculations

In the biaxial lidar system, the overlap area is calculated to determine the optimal receiver aperture position and shape using computer simulation. To subtract the background solar radiation in the daytime measurements the aperture must have specific position, shape, and dimensions for the range of interest. These calculations depend on the system parameter (see Table 3-2). The simulations are in two sections; the first part is calculations without corrections with an aperture in a round shape, and its position at the focal length of the telescope. The second section involves adaptive calculations (calculations with correction), which seek the optimal position, shape, and dimensions for the receiver aperture to subtract BG radiations. In my calculations I assumed that the laser propagation axis is parallel to the receiver (telescope) optical axis. i.e., $\delta = 0$. In practice enough time was allowed for the system alignment to make sure $\delta = 0$. Figure 4.3 illustrates the schematic diagram of the CCNY truck monostatic biaxial lidar system. The telescope is represented by a single lens of focal length f, and radius t_o. Where, $L_0 = 5$ *mm*, $b_o = 200$ *mm*, $t_o = 177.8$ *mm*, $f = 3910$ *mm*, and $\theta = 7 \times 10^{-4}$ *rad*, I studied the target range between $R_{min} = 10$ *m*, $R_{max} = 50$ *km*. Also I divided the entire range of interest into three portions, that low range (10 m – 500 m), middle range (500 m – 20 km), and high range (20 km – 50 km). However the image focus will move over the image plane significantly, but since we can calculate the movement of the image according the object height, a synchronized diaphragm can be developed to optimize the SNR.

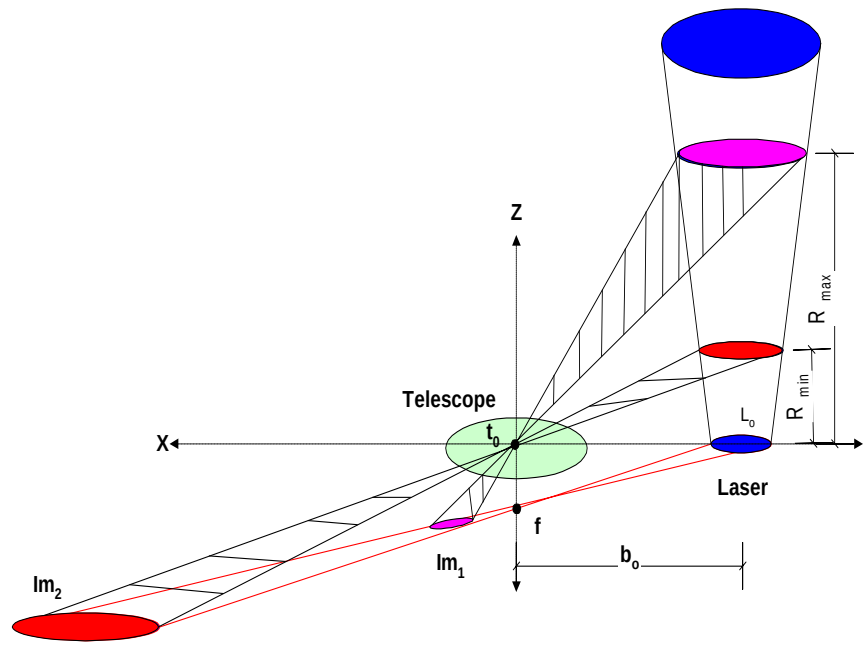

Figure 4.3 The monostatic biaxial lidar, schematic diagram shows laser beam, telescope, , and sounding trace images for ranges of R_{min}, R_{max}

4.1.3 Results

Results of simulations of lidar images and aperture capture (for different diaphragm size and lidar ranges) are introduced in the following sections below.

1.1.3.1 Results without Corrections

In this case aperture is kept in the same position at the telescope focal point (origin); also the aperture is circular shape with 2 mm diameter.

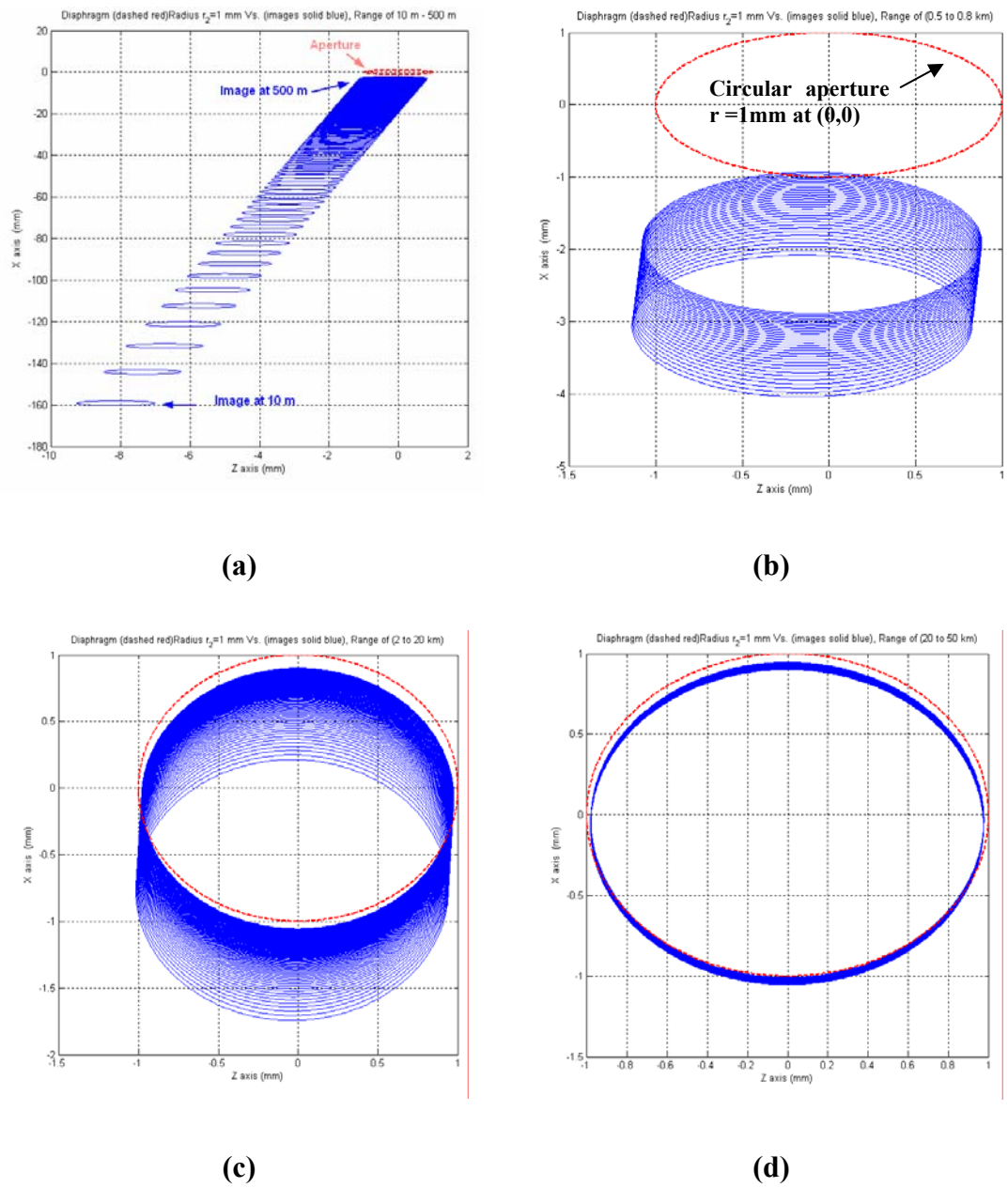

Figure 4.4 The overlap area between circular aperture with radius of 1mm vs. the object images of range R_{min}= 10 m to R_{max}=50 km (a) Short range (10-500 m) images: No overlap (b) (500-800 m) range images: Just started to overlap at 800 m (c) Range (2-20 km): Partial collection (d) Range (20 – 50 km): Almost complete collection

1.1.3.2 Results with Corrections (New Position, Circular Apertures)

For the first case, without correction the same circular aperture is kept with 1mm radius at the telescope focal point (origin). In the second case, with corrections, the round aperture is moved to a new position and made large enough to accommodate the entire images for certain range. Then I compared the GF in each case.

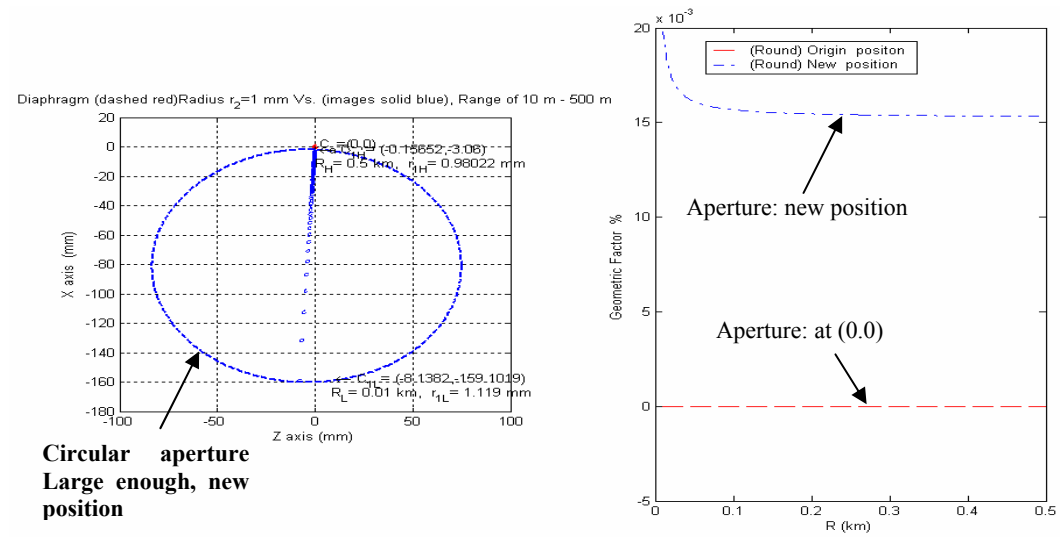

(a)

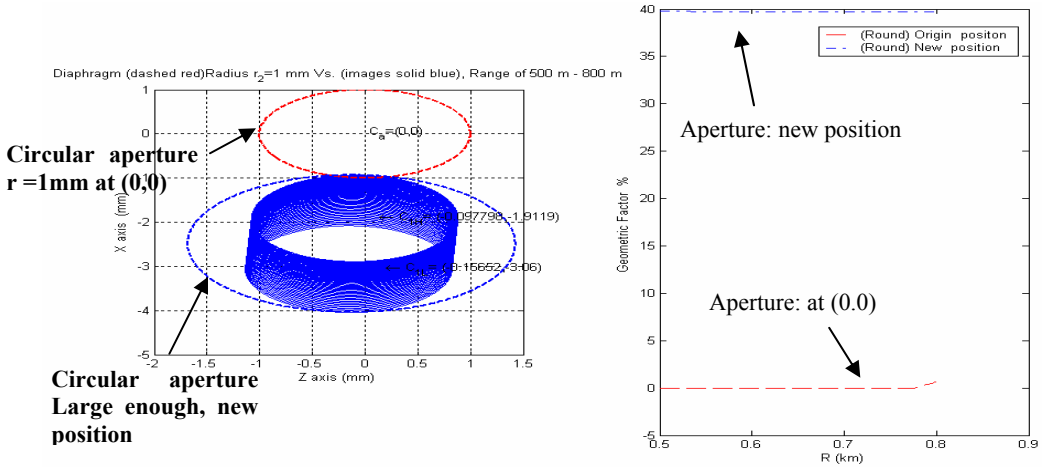

(b)

Figure 4.5 The GF of range R_{min}= 10 m to R_{max}=50 km, comparison between the original round aperture of 1mm radius at the origin and a new round aperture that accommodates the entire image. (a) Short range (10-500 m) (b) Range of (500-800 m)

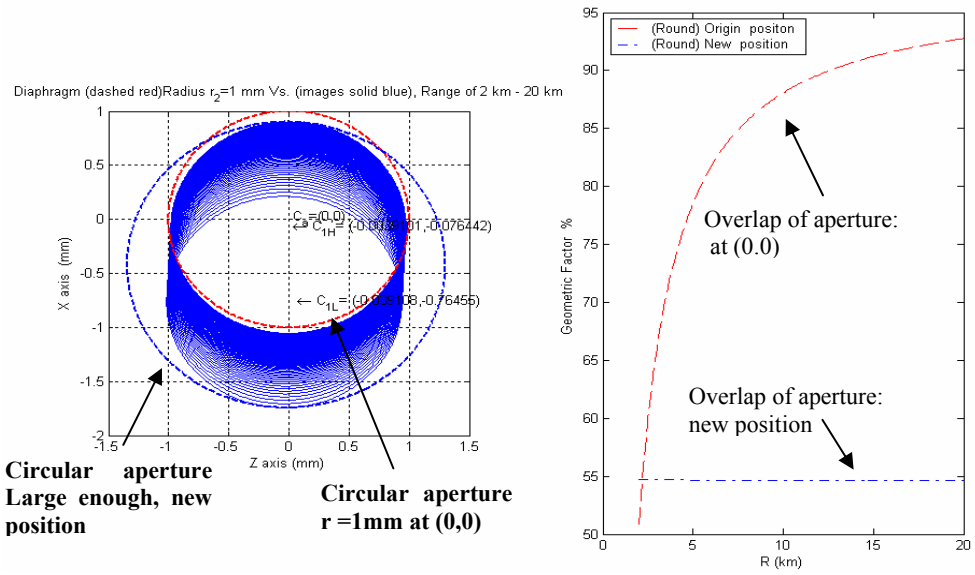

(a)

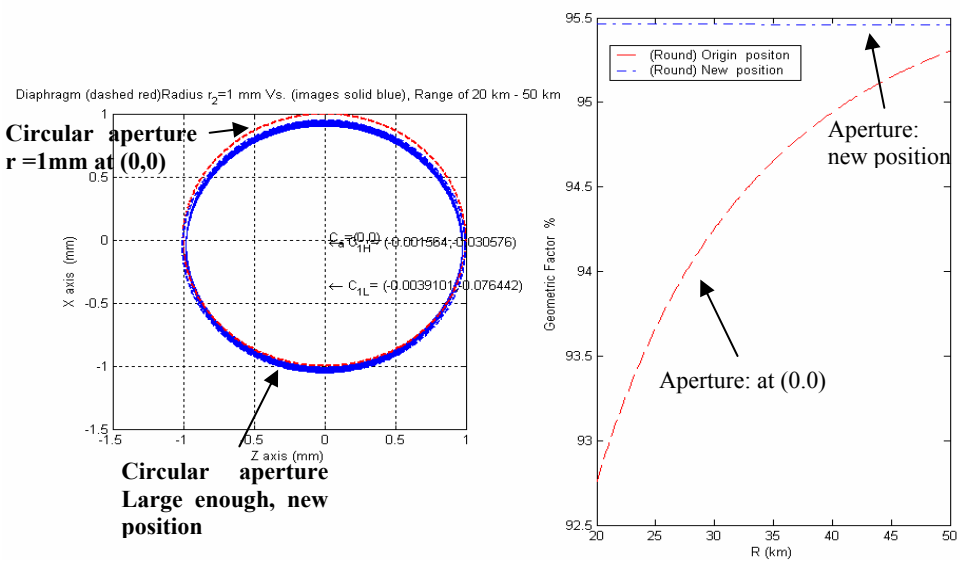

(b)

Figure 4.6 The GF of range R_{min}= 10 m to R_{max}=50 km, comparison between the original round aperture of 1mm radius at the origin and a new round one that accommodates the entire image. (a) Middle range (2-20 km) (b) High range of (20 – 50 km)

1.1.3.3 Results with Corrections (Wedge-like Shape Apertures)

In this case we are theoretically designing apertures in wedge-like shape with dimensions and positions as shown in Table 4-1. GF in these cases is equal to 100%.

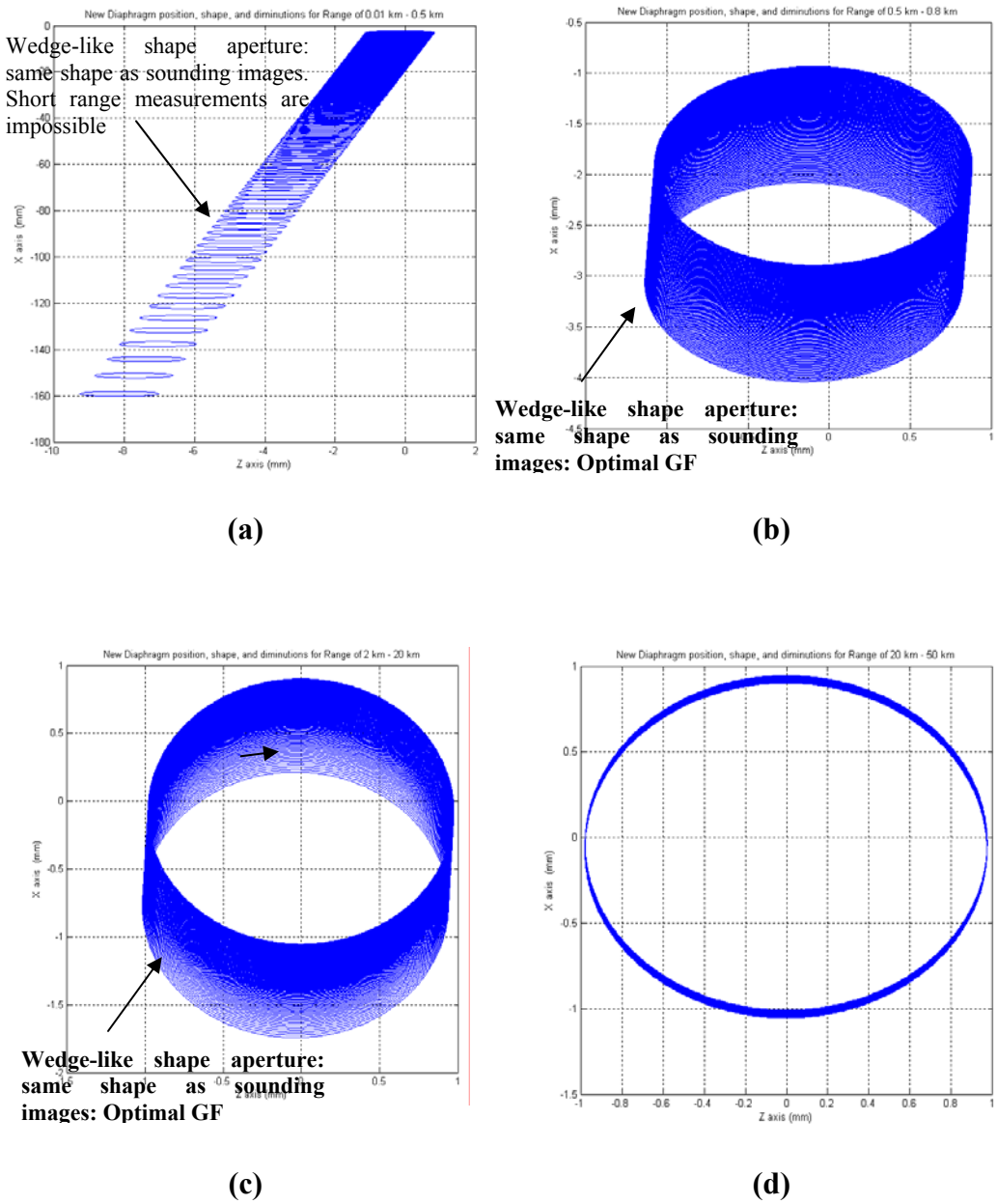

Figure 4.7 Optimal GF using new wedge-like shape apertures of various ranges, CCNY lidar (a) 10 m to 500 m (b) 500-800 m (c) 2km-20 km (d) 20 km- 50 km

4.1.4 Conclusion

In the first case, there were no change in the aperture position, size, and shape. The aperture position was at the origin (the telescope focal point), the shape and size were circular with 1mm radius (the most common aperture shape), respectively. In this case for shorter range, as shown in Figures 4.4 (a), (b), the overlap is almost zero. That is because the intersection between the receiver optics FOV and the laser beam will only occur at some distant point. Below this point in the near field, observation is impossible. On the other hand, Figures 4.4 (c), (d) show the images of biaxial lidar system at CCNY corresponding to objects at range of 2km to 50 km. the aperture is not large enough to accommodate images of the whole range. Thus the receiver detectors are cutting of the lidar backscatter signal. However, for higher ranges (greater than 20 km) one can use a common circular shape aperture with more than 86% GF. In the second case, results with corrections (new position with circular apertures) show that one can increase the circular aperture diameter and adjust the position to accommodate the entire desirable images. However, the GF will be even worse, as shown in Figures 4.5 (a), (b), and 4.6 (a) for shorter and middle range. But for the higher ranges, shown in Figure 4.6 (b), this approach provides a good solution with 95.5% GF improvement. Figure 4.7 shows the results for the third case, results with corrections (wedge-like shape apertures). Since the focused images are moving over the image plane as shown in Figures 4.3 and 4.7, I calculated the movement of the lidar image according to the object height using a computer simulations, and then I developed, theoretically, a synchronized diaphragms with special characteristics (shape, positions and size) as shown in Table 4-1. This allows us to optimize the SNR by making GF equals to 100%. Using the wedge-like shape

diaphragm characteristics in Table 4.1, a control system that moves the diaphragm to the accurate position over the image plane with respect to the object altitude and the corresponding images of interest can be implemented to assure the overlap. Therefore assure high lidar SNR.

Table 4-1 Wedge-like shape diaphragms most excellent selection: Position, dimensions, and shape due to different ranges for the mobile monostatic biaxial lidar at the CCNY

Fig. 4.7		**Small Image due to higher ranges (R_{max})**		**Big Image due to shorter ranges (R_{min})**	
	Range (altitude)	**Coordinates Image Plane**	**Radius mm**	**Coordinates**	**Radius mm**
a	**10 m – 500 m**	**(-0.156, -3.06)**	**0.9802**	**(-8.13, -159.1)**	**1.12**
b	**500 m– 800 m**	**(-0.0978, -1.9)**	**0.9792**	**(-0.156, -3.06)**	**0.9802**
c	**2 km – 20 km**	**(-0.00391, -0.076)**	**0.9776**	**(-0.039, -0.076)**	**0.9782**
d	**20 km– 50 km**	**(-0.00156, -0.0305)**	**0.9775**	**(-0.00391, -0.0764)**	**0.9776**

4.2 The he Impact of Receiver Aperture Design and Telescope Properties on Lidar SNR Improvements

Range and sensitivities of lidar measurements in daylight are limited by sky background noise power (BGP). This is particularly important for Raman lidar techniques where the Raman backscattered signal is relatively weak. This often restricts Raman lidar measurements to nighttime where BGP is absent. The background noise elimination is particularly important in daytime measurements in case where full overlap between laser beam and receiver telescope field-of-view (FOV) is necessary. Results of numerical simulations for a vertically pointing lidar show that significant improvements in lidar signal to noise ratio (SNR) can be obtained, by minimizing the detected sky BGP. This can be, optimally achieved if the receiver telescope aperture is properly designed to track lidar target images, which are range dependant. In this context, the connection between receiver telescope field of view and optimum aperture size are examined. The SNR improvements, which can be obtained in this manner, translate to corresponding improvements in lidar range for backscatter schemes including Raman and DIAL.

Light Detection and Ranging (lidar) is an active remote sensing instrument that transmits laser and measure the backscatter radiation after interacting with various components of the atmosphere. The impacts of aerosol in the human health with diseases such as lung cancer, bronchitis, and asthma have been essential motivations to record aerosol properties and transportation. lidars have been applied to study stratospheric aerosols (Zuev V., V. Burlakov et al. 1998), tropospheric aerosols (Barnaba F and Gobbi 2001) and climate gases such as stratospheric ozone (Douglass L. R., M.R. Schoeberl et al.

2000) as well as for analyzing the clouds properties (Stein, Wedekind et al. 1999). In this section of the work I examine the potential for improving SNR for monostatic lidar systems by analyzing and optimizing detector aperture (field stop) geometry. Monostatic lidar systems can be subdivided into two categories, coaxial and biaxial lidar systems. The main disadvantages in the coaxial lidar systems, where the transmitted laser beam is coaxial with the receiver's FOV, are the detector saturation problem that occurs from the superfluous scatter signals in the lidar transmitter optics. Biaxial lidars, where the transmitter and receiver are located adjacent to each other, system is a practical solution to overcome these coaxial lidar systems problems. But, on other hand, the recorded data from the biaxial lidar is negatively impacted by the geometrical factor (GF) at shorter range. To realize the effect of GF '$\xi(R)$' on the return lidar signal, the lidar Equation can be written as (Measures 1984):

$$P(\lambda_L, R) = P_L \frac{A_o}{R^2} \xi(\lambda_L) \beta(\lambda_L, R) \xi(R) \frac{c\tau_L}{2} \exp\left(-2\int_0^R k(\lambda_L, R)\, dR\right) \quad \textbf{(4.6)}$$

Where, $P(\lambda_L, R)$ is the total scatter laser power received from a distance R, P_L represents the average power in the laser pulse, A_o/R_2 describes the solid angle of the receiver optics (A_o is the area of the telescope primary mirror), $\xi(\lambda_L)$ denotes the receiver's spectral transmitter factor, $\beta(\lambda_L, R)$ is the volume backscatter coefficient, $c\tau_L$ represents laser pulse length (c is speed of light, τ_L is Laser pulse rectangular duration), $k(\lambda_L, R)$: Atmospheric extinction coefficient. The smaller the value of $\xi(R)$ is the smaller the return signal and the smaller SNR particularly for short distances. GF can be defined as the ratio of the energy transferred to the photodetector to the energy reaching the

telescope primary mirror, E_{det} /E_{scat} (Velotta, B. Bartoli et al. 1998).This reduction in the detector response to the return signal is caused by a lack of perfect overlap between the receiver telescope's FOV and the transmitter laser beam. In Section 4.2.1, we discuss the overlap effect of the GF including the receiver field stop position and size, and their effect in lidar SNR improvement. Lidar simulation results are introduced in section 4.2.2. Also, the telescope best selection to reduce BGP is introduced in Section 4.2.3. Conclusions and future works are presented in Section 4.2.4.

4.2.1 Problem Description and Analysis

The standard configuration for most lidars is to place a round aperture in the focal point of the receiver telescope. It is also commonly assumed that once the lidar receiver FOV and transmitted beam are completely overlapping, the efficiency of collection is unity (Measures 1984). However, this analysis does not properly take into account the shifted position of the collected backscattering signals on the image plane from the telescope focal point at the receiver. The position and size of the atmosphere sounding (image) vary according to the distance 'b_o' between the laser and telescope optical axis. This image displacement is range dependant as shown in Fig. 4.8. In Fig 4.8, the telescope is represented by a lens with diameter of t_o and (f) focal length. The farther the lidar object ($Z=R_{max}$) the smaller the sounding image (Im_1), on the other hand the closer the lidar object ($Z=R_{min}$) the larger the sounding image (Im_2). Numerous papers implemented a wedge like shape aperture design to over come this shifted problems (Agishev and Comeron 2002; Hassebo, R. Agishev et al. 2004). In this paper we study the effect of changing a round aperture, the realistic shape, size and place in the lidar SNR.

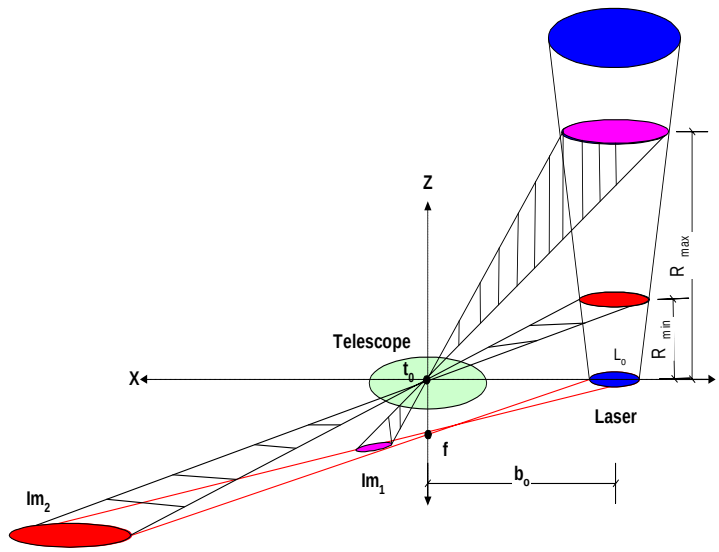

Figure 4.8 The monostatic biaxial lidar, schematic diagram shows laser beam, telescope, , and sounding trace images for ranges of R_{min}, R_{max}

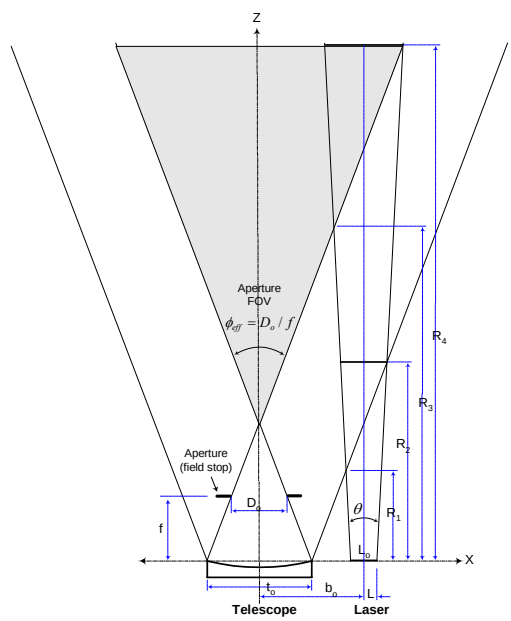

Figure 4.9 Biaxial lidar: overlapping between effective FOV of receiver telescope (diameter of t_o) and laser beam (initial diameter L_o) and aperture diameter D_o

As shown in Fig. 4.8, z: is optical vertical axis. The ground level (x-axis), where the location of the telescope primary mirror and the transmitted laser beam, is at $z=0$. As the range R increases, there will be a point R_1 where the first intersection between the left boundary of the laser beam and the right boundary of the telescope FOV occurs. Then at ($z= R_2$) the complete overlap is formed with the telescope FOV. But this is not the effective overlap function. The effective FOV is based on, D_o, the field stop diameter and f 5s the telescope focal length ($\phi_{eff} = D_o / f$ the shaded area in this case) (Hassebo, R. Agishev et al. 2004). The actual overlap started at ($z= R_3$) and finally the effective overlap is completed at (z= R_4). At short distances ($z<R_3$) the ratio of the overlapping area (OL_{area}) to the image area (Im_{area}) that formed near to f is:

$$\xi(R) = \frac{OL_{area}}{\mathrm{Im}_{area}} = 0 \tag{4.7}$$

where $OL_{area} = 0$. This is makes near field observations impossible (effective telescope area: $A_{eff}(R) = A_o \xi(R) = 0$). In the case of a small circular aperture ($D_o = 2\ mm$ diameter) at the telescope focal pint f_o, the overlap function $\xi(R)$ is very small for any object in ranges of ($R_3<z<R_5$), where at R_5 there is an arbitrary object which has a large sounding image that is formed very far from f in the imaging plan (see Fig. 4.8). Design of a unique aperture to cover certain desired ranges is feasible.

4.2.2 Results

In this work I propose a feasible design of a circular aperture to accommodate certain desired ranges and minimize the detected BGP. That can be achieved by moving the center of the simple aperture (D_o) from the origin (Agishev and Comeron 2002) some distance to the left (depending on the object height) and reducing the aperture size from D_o to smaller diameter D_s (i.e., reducing the effective FOV from $\phi_{eff} = D_o / f_o$ to $\phi_{eff} = D_s / f_s$) where f_s is a smaller telescope focal length. Lidar simulation results for biaxial system are shown in Fig. 4.9. This simulation is for the following parameters: The distance between the beam and the telescope axis is $b_o = 200\ mm$, laser initial beam diameter $L_o = 5$ mm, beam divergence $\theta = 0.5 mrad$, telescope primary mirror diameter of $t_o = 178\ mm$, and two different telescope focal lengths of $f_s = 1.7\ m$, $f_L = 4\ m$. We always take into account that θ is smaller than the effective telescope's FOV ($\phi_{eff} = D / f$), and that both D and f (the field stop diameter and the telescope focal length, respectively) have three different values. These values are: (1) $D = D_o = 2mm$, for commonplace aperture (placed at the telescope focal length $f = f_o$). (2) $D = D_s$ for small telescope focal length ($f = f_s = 1.7\ m$). (3) $D = D_L$ for telescope with bigger focal length ($f = f_L = 4\ m$). Obviously, the new aperture position and size reduction are range dependent. For shorter ranges (0.5 – 5 km) the aperture diameter became smaller (i.e., $D_s = 1.8\ mm$ for $f_s = 1.7\ m$) and the center is shifted by ~0.45 mm, on the other hand, if we use a bigger telescope, a field stop diameter of $D_L = 4.7\ mm$ (for $f_L = 4m$) must be used. This bigger aperture (i.e., bigger BGP) center must be shifted by ~2.4 mm that to housing the entire images. However, for higher lidar ranges (5-25 km) the field stop size gets much smaller ($D_s = 1.4$

mm for f_s*=1.7 m*) that centered approximately at the origin (0, 0), but D_L *=3 mm* center shifted by ~0.5 mm. I noted that the field stop shifted positions and sizes changing are more significant for the shorter ranges particularly for bigger telescope focal length.

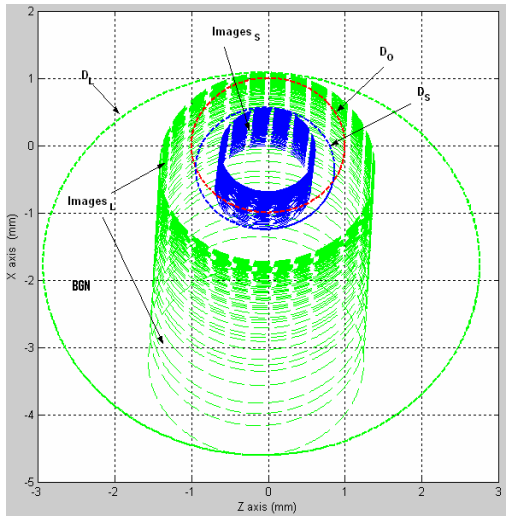

Figure 4.10 Lidar images for range 500m-5km. The green images (images $_L$) for 4 m telescope focal length and the blue images (images $_S$) for telescope with 1.7m focal length. The commonplace aperture (D_o=2 mm) placed at the telescope focal point, D_L is a round aperture to accommodate (images $_L$) and D_S is a round aperture to accommodate (images $_S$).

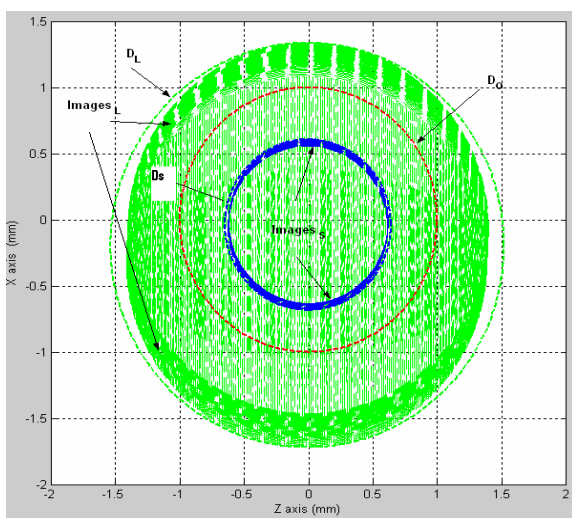

Figure 4.11 Lidar images for range 5km-25km. The green images (images $_L$) for 4 m telescope focal length and the blue images (images $_S$) for telescope with 1.7m focal length. The commonplace aperture (D_o=2 mm) placed at the telescope focal point, D_L is a round aperture to accommodate (images $_L$) and D_S is a round aperture to accommodate (images $_S$).

4.2.3 Telescope Selection

Typically in lidar measurements a larger FOV_{eff} is desired to decrease the height where the laser beam meets the effective telescope FOV for the first time ($z= R_3$). The FOV_{eff} ($\phi_{eff} = D / f$) enlargement requires increasing the field stop size (D) for the same telescope focal length f. Yet, the larger the FOV_{eff} (ϕ_{eff}) the bigger the BGP that reaches the PMT, beside the larger the multiple scattering effect (Allen and Platt 1977; Bruscaglioni, G. Zaccanti et al. 1983; Sassen and Petrilla 1986). This trade off can be optimized using two techniques. (1) If the laser beam is tilted toward the telescope by inclination angel Θ to increase the effective lidar range (Stelmaszczyk, M. Dell'Aglio et al. 2005). (2) Reducing FOV_{eff} by decreasing both field stop diameter (D) and telescope focal length f, that the BGP increment can be avoided. Where, BGP is proportional to FOV_{eff} in the shot noise regime (Kuze, H. Kinjo et al. 1998; Hassebo, B. Gross et al. 2006). As shown in the simulation results (Figs. 4.10 and 4.11), the larger the telescope focal length ($f= f_L$), is the larger the image size ($Images_L$), and the larger the sky BGP mainly in shorter distance. Where ($Images_L$), in Figs. 4.10 and 4.11, are the lidar sounding images collected through ($f_L = 4m$) telescope focal length, and ($Images_S$) represents the lidar sounding images collected through telescope with focal length of ($f_S=1.7\ m$) both from objects at ranges of 500m-5km, and 5km-25km as illustrated in Figs 4.10 and 4.11, respectively. D_s, blue circle, and D_L, green circle, represent the round shape apertures that accommodate the entire lidar return signal with a 1.7m, and 4m telescopes respectively. As can be seen in Table 4-2, numerical results show that a factor of as much as (17.8 %) improvement in lidar signal-to-noise ratio is obtained if we use

even smaller telescope ($f_S=1\ m$) over conventional large telescope ($f_L=4\ m$). That improvement is attainable if we assume that the mean value of the photomultiplier tube (PMT) output power (P_d) is proportional to BGP (i.e., $\langle p_d \rangle \alpha BGP$). i.e., the detector operates in the shot noise limit. A system operating below under the shot noise limit (if the detected noise amplitude (standard deviation) is proportional to the square root of the mean detected signal at the fare range (i.e. $\Delta P_d = \sqrt{\langle p_d \rangle}$).The potential of this work becomes visible if we compare the detected SNR with small and bigger telescope focal lengths. In the shot noise regime, the SNR improvement factor (SNR_{imp}) can be expressed in terms of BGP corresponding to large and small telescope focal length (BGP^L, BGP^S, where in this case $BGP^L > BGP^S$) (Hassebo, B. Gross et al. 2006):

$$SNR_{imp} = \frac{SNR_S}{SNR_L} = \sqrt{\frac{P_{sig} / BGP^S}{P_{sig} / BGP^L}} = \sqrt{\frac{BGP^L}{BGP^S}} \qquad \textbf{(4.8)}$$

This formula shows that decreasing the sky background noise from BGP^L to BGP^S using smaller telescope focal length will improve the SNR. This SNR improvement can be translated into improvement in the attainable lidar range.

Table 4-2 Image size vs. telescope focal length for different lidar range. Effective FOV (ϕ_{eff}) is shown no big different in the higher range for a variety of *f*. Normalized ϕ_{eff} with respect to ϕ_{eff} of (f = 4m) is also shown.

Telescope F	**Lidar range 'R'**		**Aperture diameter**	**$\phi_{eff} = D_L / F$**	**ϕ_{eff} (Norm)**	**SNR_{Imp}**
	From (km)	**To (km)**	**D_L**	**(mrad)**	**%**	**%**
4 m	**0.5**	**5**	**4.7**	**1.175**	**100**	**0**
	5	25	3	0.75	100	0
3 m	**0.5**	**5**	**3.4**	**1.13**	**96**	**2**
	5	25	2.1	0.7	93	3.6
1.7 m	**0.5**	**5**	**1.8**	**1.058**	**90**	**5.4**
	5	25	1.4	0.7	93	3.6
1 m	**0.5**	**5**	**0.85**	**0.85**	**72**	**17.8**
	5	25	0.6	0.6	80	11.8

By comparing the results in Table 4-2, it is evident that a lidar system with small focal length (*f= 1m*) is much better for reducing BGP than other systems with big focal length (*f =4m* for example) telescope particularly, for short distances. This subtraction of the BGP can be translated to improvement in lidar SNR up to 17.8 %. Alternately it represents significant improvement in the lidar range and/or the detector's averaging time. Where, we can relate SNR improvement with the detector's averaging time improvement (τ_{imp}^{det}) as: $\tau_{imp}^{det} = (SNR_{imp})^2$ (Hassebo, B. Gross et al. 2005). Thus, an improvement of detector's averaging time of, $\tau_{imp}^{det} = (0.18)^2 \approx 3.2\%$, can be achieved from a 17.8 % lidar SNR improvement.

4.2.4 Conclusions

In the classical design of lidar receiver subsystem which does not take into account that in the receiving optics the detected images are placed on a line forming an angle with the imaging plane of receiver telescope, GF is often too small. The design proposed here to minimize detected sky BGN by more optimally locating a smaller circular receiver aperture results in significant lidar SNR improvement. Simulated numerical results for a biaxial lidar have shown the best telescope selection is one using a small circular aperture (field stop) with a small telescope focal length *f* to ensure the minimum FOV that accepts all return signals over the entire lidar range while at the same time minimizing detected BGP and hence maximizing lidar SNR and attainable lidar ranges. The improvement in lidar SNR was up to 18 %. This in turns lead to a good improvement in the lidar range and the detector's averaging time. A reduction of the required detector's averaging time of, $\tau_{imp}^{\det} \approx 3.2\%$, can be achieved.

4.3 Detectors Noise Considerations

Detector is an electro-optical element that converts light energy to electrical energy. Detectors enable scientists to quantify the intensity of light and to sense light outside of the visible region of the electro-magnetic spectrum. In lidar system we normally use Photo Multipliers Tubes (PMT) to detect visible and ultraviolet backscatter signals, beside Raman lidar signals, but Avalanche photodiodes (APD) are used for IR backscatter detection signal. An APD is a Solid State detector. It operates like a photodiode but electrons enter an avalanche region where they multiply by gain of about 50 to 100s times. PMTs are vacuum tubes. Photons enter the tube through the photocathode, get converted to an electron and get multiplied by the dynodes; the multiplied secondary electrons emitted from the last dynode are finally collected by the anode as shown in Figure 4.12. PMTs generally operate with a gain of about 10^6 . PMTs are generally used where really low light levels need to be detected, on other hand APDs are generally used where the light wavelength of interest is out of the PMT sensitivity range. However, some companies produced APD to replace the PMTs in certain wavelength with better behaviors than the PMTs in the same range. For example, now we can measure optical signals in the near IR using APD with high quantum efficiency (QE) (at 650 nm QE>80%, at 900 nm QE= 85%, and at 1060 nm QE=38%) comparable to UV-Visible detectors. The increased sensitivity in the near infrared is a major advantage compared to photomultipliers. And the must interesting issue is; signals can be acquired using analog detection as well as single photon counting mode using APDs.

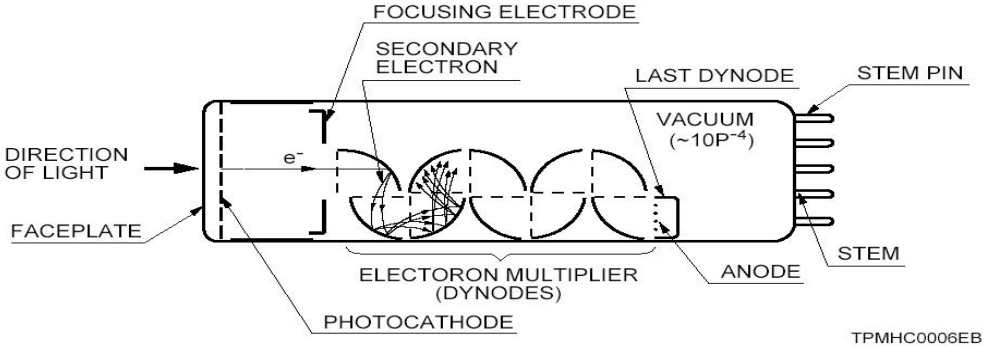

Figure 4.12 The Photomultiplier Tube (PMT) schematic diagram (Hamamatsu)

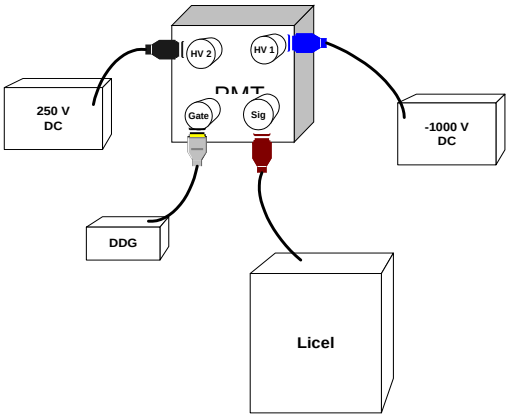

Figure 4.13 Photomultiplier Tube (PMT) connection

In PMTs, the photocathode characteristics and the operating gain are the main parameters determining the electronic noises. Dark current is electrons that released from the photocathode in the absence of any incident light. Dark current arises from thermal and field-emission processes and can be any where from 10^{-13} to 10^{-17} Amperes at room

temperature (Measures 1984). To optimize the SNR, PMT should be selected on the basis of maximum quantum efficiency at the wavelength of interest. Thermionic and field emission release of electrons from the dynodes is an important component of the dark current. Cooling is a solution where Thermionic emission is highly temperature-dependant. Focusing the incident light on only a small part of the photocathode will increase SNR. Also using the photon counting mode which discriminates single electron pulses that have not acquired the full gain will improve the SNR. Furthermore, to prevent the PMTs saturations especially from near field scatter of laser radiation by using ND filters and/or large distance separation between the transmitter and the receiver optics. In CCNY lidars systems we store data in 1 min data files (3000 shots with 50 Hz laser pulses) for the lab lidar system, and 1200 shots with 10 Hz laser pulses for the truck lidar system. These returns are averaged during the analysis procedures. The following formulas describe SNR in laser radar system. This illustrates how different kinds of noises are involved in the SNR relationship, (in the denominators), i.e., if we reduce these noises we improve SNR.

$$(SNR)^2 = \frac{E_s^2(\lambda)}{E(\lambda)\left[E_s(\lambda) + E_b^T(\lambda) + \frac{(i_d + i_J)E(\lambda)}{2eB^*}\right]} \quad \textbf{(4.9)}$$

Where

$E_s(\lambda)$ The arrival signal pulse energy at the PMT in the time interval $t - to - (t + \tau_d)$

$i_d = \frac{e\langle n_e^d \rangle}{\tau_d}$ = the mean photocathode noise

$\langle n_e^d \rangle$ The mean number of photocathode electrons created in the interval τ_d in the absent of light

i_J = Johnson (thermal) noise current

e : The electronic charge

$E_b^T(\lambda) = E_b^N(\lambda) + v_\eta E_b^L(\lambda_L)$: The total background

$E_b^N(\lambda)$: The natural background

$E_b^L(\lambda_L)$: The laser scatters background

$$v_\eta = \frac{\lambda_L \eta(\lambda_L)}{\lambda\ \eta(\lambda\ )}$$

λ_L : The wavelength of the photo detection system

$\eta(\lambda\ )$: The quantum efficiency of the photocathode at wavelength λ

$$B^* = \frac{BF_G}{\xi_e}$$

$B = \dfrac{1}{2\tau_d}$: The photodetector bandwidth

F_G: Represent δ^2, where ($\delta \approx 1$) account for the statistical fluctuations in the emission of the secondary electrons from the dynodes, and can thought of as a noise factor associated with the gain. F_G = *1 to 2.5*

ξ_e: The collection efficiency of the electrostatic focusing (defines what fraction of the photoelectrons, created at the cathode, arrives at the first dynode). The relevant parameters for photocathode, PMT anodes, and APD SNRs are summarized below (Measures 1984).

4.3.1 The photocathode SNR

$$(SNR)_c = \frac{i_s}{\left[\sqrt{2eB(i_s + i_b + i_d)}\right]} = \frac{i_s}{i_n} \quad \textbf{(4.10)}$$

$i_s(t) = \dfrac{\lambda\eta(\lambda)eE_s(\lambda)}{hc\tau_d}$ **The photocathode current**

$\dfrac{\lambda E_s(\lambda)}{hc\tau_d}$ The mean rate of arrival of signal photons (energy of $\dfrac{hc}{\lambda}$) at the photocathode

$i_n = \sqrt{2eB(i_s + i_b + i_d)}$ The shot noise

$i_b = \dfrac{e\left\{\lambda\eta(\lambda)E_b^N(\lambda) + \lambda_L\eta(\lambda_L)E_b^L(\lambda_L)\right\}}{hc\tau_d}$ The equivalent background current

4.3.2 The SNR for the PMT (anode current)

$$(SNR)_a = \frac{G\xi_e i_s}{\left[\sqrt{2eBG^2F_G\xi_e(i_s + i_b + i_d)}\right]} = \frac{I_s}{I_n} \quad \textbf{(4.11)}$$

I_n: The noise current at anode

$I_s = G\xi_e i_s$: The anode signal current

G: The dynode chain gain (10^5 - 10^7)

4.3.3 The SNR for the APD (Avalanche Photodiode)

$$SNR = \frac{G\xi_e i_s}{\sqrt{\left(\frac{4kTB}{R_{eq}}\right) + 2eBG^2 F_G \xi_e (i_s + i_b + i_d)}} \quad \textbf{(4.12)}$$

$\left(\frac{4kTB}{R_{eq}}\right)$: The Johnson (thermal) noise current associated with the equivalent load resistance of the output circuit R_{eq}

i_d : The bulk leakage current of the APD

ξ_e : can be unity

$F_G = 1$ *to* 2.5

4.3.4 Detectors Selection

The PMT types used in the CCNY lidars were carefully selected in terms of SNR considerations. Initially, we used PMT type R758-10 in the truck (mobile) lidar system, and PMT type R928 in the Laboratory (stationary) lidar system. The PMT R758-10 has a small anode dark current (0.1 n ampere), but also has a small maximum output current (0.001 m ampere). On the other hand the effective area is (3*12 mm^2). For PMT type R928; the anode dark current (3 n ampere) which too high value, but the maximum

output current (0.1 m ampere) is acceptable value, and the effective area is (8*24 mm^2) which good enough. Both PMTs were not sufficiently low noise for the photon counting mode. So currently, we use three different types of PMT, (R11527 P, R7400 P-06, and R2693 P). These types are specially selected on account of low noise and high gain for use in PC mode (Hamamatsu). Table 4-3 is a comparison between the previous PMTs and the current PMTs that we use at CCNY lidars. The comparison shows the different between the PMT's characteristics that affect the SNR as shown above in section (4.3). It was also essential to eliminate spurious radio frequency (rf) noise by proper grounding and avoidance of ground loops.

Table 4-3 Detectors selection improved SNR. Main PMTs characteristics of CCNY lidars: both previous and current systems are shown. (Hamamatsu)

Key Specifications	**Previous PMTs**		**Current PMTs**		
	R758-10	**R928**	**R1527 P**	**R2693 P**	**R7400P06**
For Photon Counting Gain			6.7E+06	6 E+06	1 E +6
Dark Current	0.1 nA	3 nA	0.1-0.5 nA	0.1-2 nA	0.2 nA
Dark Count			10 cps	15-50 cps	80-400 cps
Quantum efficiency at 300 nm: (%)			19	20.5	
Gain	4.5E+05		6.7E+06	6 E+06	1 E+06
Active area	3 x 12 mm	8 x 24 mm	8 x 24 mm	18 x 16 mm	8 mm ϕ
Wavelength range	160-930 nm		185-680 nm	185-650 nm	300-650 nm
Peak sensitivity wavelength			400 nm	375 nm	420 nm
# of Dynodes	9		9	9	8

5 POLARIZATION DISCRIMINATION TECHNIQUE TO MAXIMIZE LIDAR SIGNAL-TO-NOISE RATIO FOR DAYLIGHT OPERATIONS

The impact and potential of a polarization selection technique to reduce sky background signal for linearly polarized monostatic elastic backscatter lidar measurements are examined. Taking advantage of naturally occurring polarization properties in scattered sky light, we devised a polarization discrimination technique in which both the lidar transmitter and receiver track and minimize detected sky background noise while maintaining maximum lidar signal throughput. Lidar elastic backscatter measurements, carried out continuously during daylight hours at 532 nm, show as much as a factor of $\sqrt{10}$ improvement in signal-to-noise ratio and the attainable lidar range up to 34% over conventional un-polarized schemes. For vertically pointing lidars, the largest improvements, are limited to the early morning and late afternoon hours, while for lidars scanning azimuthally and in elevation at angles other than vertical, significant improvements are achievable over more extended time periods with the specific times and improvement factors depending on the specific angle between the lidar and solar axes. The resulting diurnal variations in SNR improvement sometimes show asymmetry with solar angle, which analysis indicates can be attributed to changes in observed relative humidity that modifies the underlying aerosol microphysics and observed optical depth.

5.1 Introduction

This work describes a technique which is designed to improve the operation of conventional elastic backscatter lidars in which the transmitted signal is generally linearly polarized. The technique requires the use of a polarization sensitive receiver. Polarization selective lidar systems have, in the past, been used primarily for separating and analyzing polarization of lidar returns, for a variety of purposes, including examination of multiple scattering effects and for differentiating between different atmospheric scatterers and aerosols (Schotland, K. Sassen et al. 1971; Hansen and Travis 1974; Sassen 1974; Platt 1977; Sassen 1979; Platt 1981; Kokkinos and Ahmed 1989; G.P.Gobbi 1998; Roy, G. Roy et al. 2004). In the approach described here, the polarized nature of the sky background light is used to devise a polarization selective scheme to reduce the sky background power detected in a lidar. This leads to improved signal-to-noise ratios (SNR) and attainable lidar ranges, which are important considerations in daylight lidar operation (Hassebo, B. Gross et al. 2005; Hassebo, Barry M. Gross et al. 2005; Ahmed, Y. Hassebo et al. 2006; Ahmed, Yasser Y. Hassebo et al. 2006; Hassebo, B. Gross et al. 2006). The approach discussed here is based on the fact that most of the energy in linearly polarized elastically backscattered lidar signals retains the transmitted polarization (Schotland, K. Sassen et al. 1971; Hansen and Travis 1974; Kokkinos and Ahmed 1989), while the received sky background power (Welton, Campble et al.) observed by the lidar receiver shows polarization characteristics that depend on both the scattering angle, θ_{sc}, between the direction of the lidar and the direct sunlight and the orientation of the detector polarization relative to the scattering plane. In particular, the sky background signal is minimized in the plane perpendicular to the scattering plane,

while the difference between the in-plane component and the perpendicular components (i.e degree of polarization) depends solely on the scattering angle. For a vertically pointing lidar, the scattering angle θ_{sc} is the same as solar zenith angle θ_s Fig. 5.1. The degree of polarization of sky background signal observed by the lidar is largest for solar zenith angles near $\theta_S \approx 90^o$ and smallest at solar noon. The essence of the proposed approach is therefore, at any time, to first determine the parallel component of P_b with a polarizing analyzer on the receiver, thus minimizing the detected P_b, and then orienting the polarization of the outgoing lidar signal so that the polarization of the received lidar backscatter signal is aligned with the receiver polarizing analyzer. This ensures unhindered passage of the primary lidar backscatter returns, while at the same time minimizing the received sky background P_b , and thus maximizing both SNR and attainable lidar ranges.

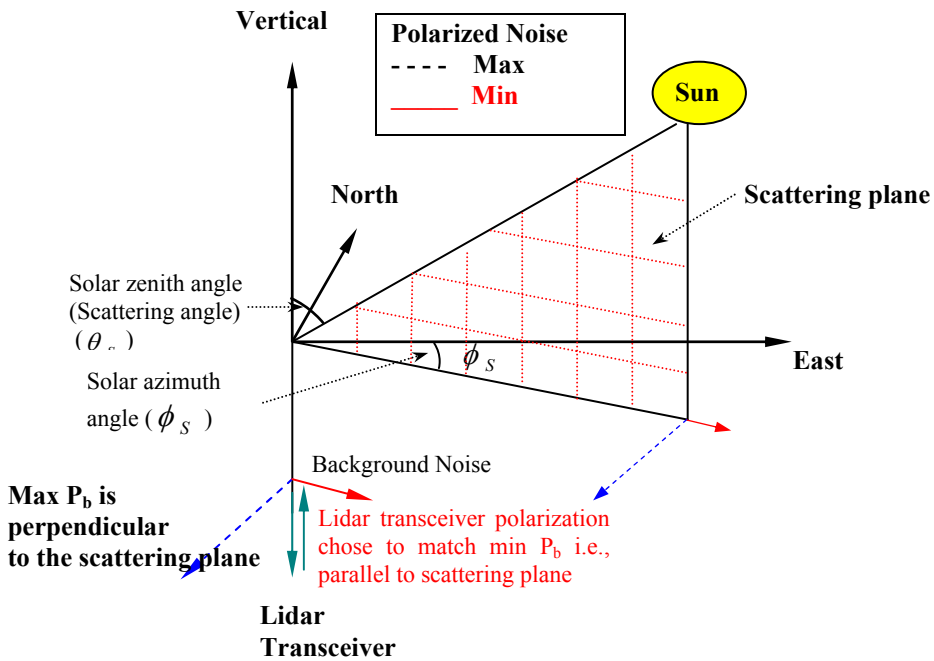

Figure 5.1 Sky background suppression geometry for a vertical pointing lidar: θ_s is the solar zenith angle (equal to the scattering angle for this geometry) ϕ_s is the solar azimuth angle; and OAB is the solar scattering plane

The experimental approach and system geometry to implement the polarization discrimination scheme are described in **Section 5.2**. **Section 5.3** presents results of elastic lidar backscatter measurements for a vertically pointing lidar at 532 nm taken on a clear day in the New York City urban atmosphere, that examine the range of application of the technique. In particular, the diurnal variations in P_b as functions of different solar angles are given and the SNR improvement is shown to be consistent with the results predicted from the measured degree of linear polarization, with maximum improvement restricted to the early morning and late afternoon. **Section 5.4** examines the situations in

which asymmetric diurnal variations in sky P_b are observed, and demonstrates the possibility that an increase in relative humidity (Halldorsson and Langerhoic), consistent with measured increases in measured Precipitable water vapor (PWV) and aerosol optical depth (AOD), may account for the asymmetry.

Analysis of the overall results is presented in **Section 5.5**, where the SNR improvement factor is compared with a single scattering radiative transfer theory. Possible modifications due to multiple scattering are also explored. In **Section 5.6**, the diurnal variation of the polarization rotation angle is compared to the theoretical result and an approach for automation of the technique based on theory is discussed. In addition, the potential impact of the method on lidars scanning azimuthally and in elevation at angles other than vertical is examined and shown to have a much wider range of effective operational periods during the day compared to vertical lidars. Conclusions and summary are presented in **Section 5.7**.

5.2 Experimental approach and system geometry

The City University of New York (CUNY) has developed two ground-based lidar systems, one mobile and one stationary, that operate at multiple wavelengths for monostatic elastic backscatter retrievals of aerosol and cloud characteristics and profiles. Lidar measurements are performed at the Remote Sensing Laboratory of the City College of New York, (CCNY). The lidar systems are designed to monitor enhanced aerosol events as they traverse the eastern coast of the United States, and form part of NOAA's Cooperative Remote Sensing Center (NOAA-CREST) Regional East Atmospheric Lidar

Mesonet (REALM) lidar network. The lidar measurements reported here were carried out with the mobile elastic monostatic biaxial backscatter lidar system at the CCNY site (longitude 73.94 W, latitude 40.83 N), at 532 nm wavelength. The lidar transmitter and the receiver subsystems are detailed in Table 5-1

Table 5-1 Lidar system specifications

Transmitter		**Receiver**	
Laser	Q-Switched Nd: YAG Continuum Surelite ll - 10	**Telescope Aperture**	CM_1400 Schmidt Cassegrian telescope 35.56 mm
Wavelength	1064, 532, 355 nm	**Focal length**	3910 mm
Energy/pulse	650 mj at 1064 nm 300 mj at 532 nm 100 mj at 355 nm	**Detectors** **532 nm** **355 nm** **1064 nm**	Hamamatsu PMT: R11527 P PMT: R758-10 APD
Pulse Duration	7 ns at 1064 nm	**Data Acquisition**	LICEL TR 40-160
Repetition Rate	10 Hz	**Photon Counting**	LICEL TR 40-160
Harmonic Generation	Surelite Double (SLD) Surelite Third Harmonic (SLF)		

The lidar return from the receiver telescope is detected by a photo-multiplier (PMT R11527P) with a 1 nm bandwidth optical filter (532F02-25 Andover), centered at the 532 nm wavelength. For extended ranges, data is acquired in the photon counting (PC) mode, typically averaging 600 pulses over a one minute interval and using a Licel 40-160 transient recorder with 40 MHz sampling rate for A/D conversion and a 250 MHz photon counting sampling interval. Fig. 5.2 shows the arrangement used to implement the polarization-tracking scheme. To select the polarization of light entering the detector, a polarizing beam splitter is located in front of the collimating lens that is used in

conjunction with a narrow band filter (alternatively, dichroic material polarizers were also used).

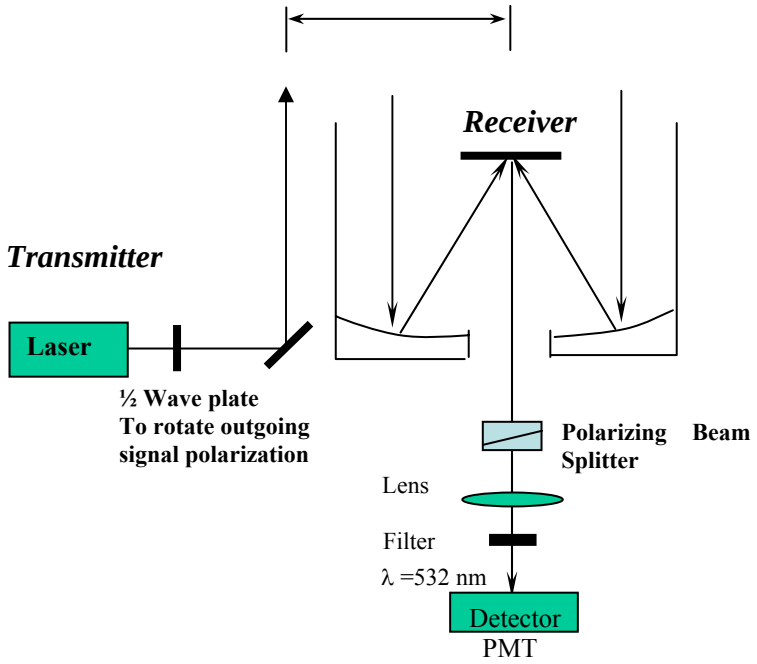

Figure 5.2 Schematic diagram of polarization experiment set up for elastic biaxial monostatic lidar (mobile lidar system)

This polarizing beam splitter (analyzer) is then rotated to minimize the detected sky background P_b. Cross polarized extinction ratios on the receiver analyzer were approximately 10^{-4} . On the transmission side, a half wave plate at the output of the polarized laser output is then used to rotate the polarization of the outgoing lidar beam so as to align the polarization of the backscattered lidar signal with the receiver polarizing analyzer and hence maximize its throughput (i.e., at the minimum P_b setting). This procedure was repeated for all measurements, with appropriate adjustments being made in receiver polarization analyzer alignment and a corresponding tracking alignment in the

transmitted beam polarizations to adjust for different solar angles at different times of the day, and hence minimize the detected P_b and maximize lidar SNR.

5.3 Results

5.3.1 Lidar data

Figures 5.3- to- 5.5 show experimental results with the receiver analyzer oriented to minimize P_b and a corresponding tracking lidar polarization orientation to maximize the detected backscattered lidar signal and its SNR at different times on Oct 07, 2004 (6:29 PM, 3 PM, and noon). All times given are in (EST) Eastern Standard Time.

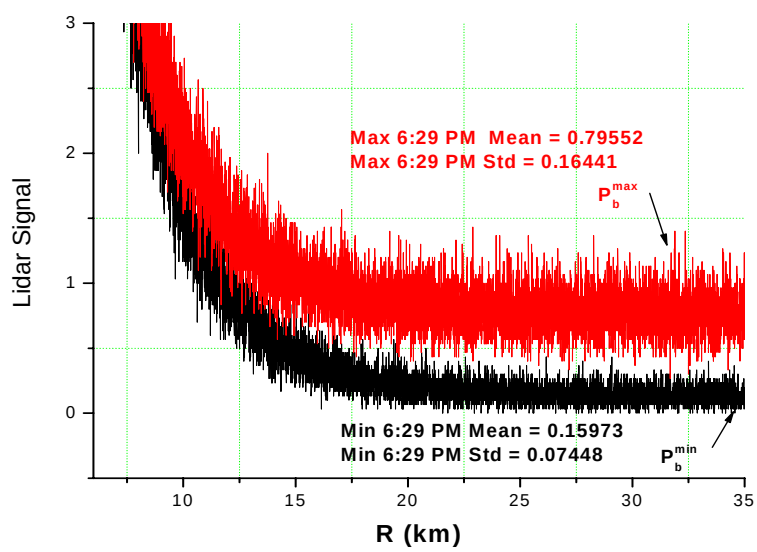

Figure 5.3 Comparison of max P_b verses min P_b lidar signals at 6:29 PM on 07 October 2004.

The detected lidar signal is the sum of atmospheric backscatter of the laser pulse and the detected background light. The upper trace corresponds to the receiver polarization analyzer oriented to minimize P_b and the lidar transmitter polarization oriented to maximize the detected backscattered lidar signal while the lower trace is the result when orthogonal orientations of both receiver analyzer and lidar polarization are used, minimizing the sky background component in the return signal. Similar measurements were made at 3:00 PM and noon on the same day as shown in Figures 5.4 and 5.5 respectively.

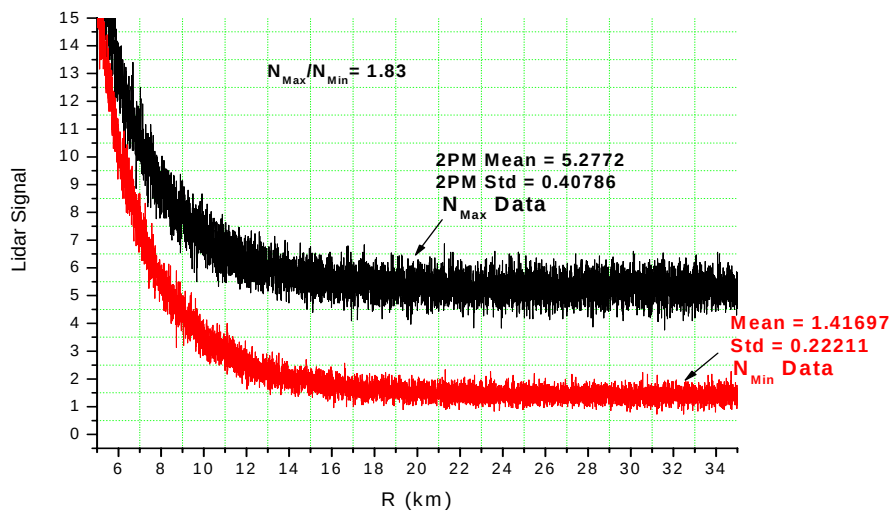

Figure 5.4 Comparison of max max P_b (N_{Max}) verses min P_b (N_{Min}) lidar signals at 3 PM (EST) on 07 October 2004: Range 35 km, Lidar signal in linear scale

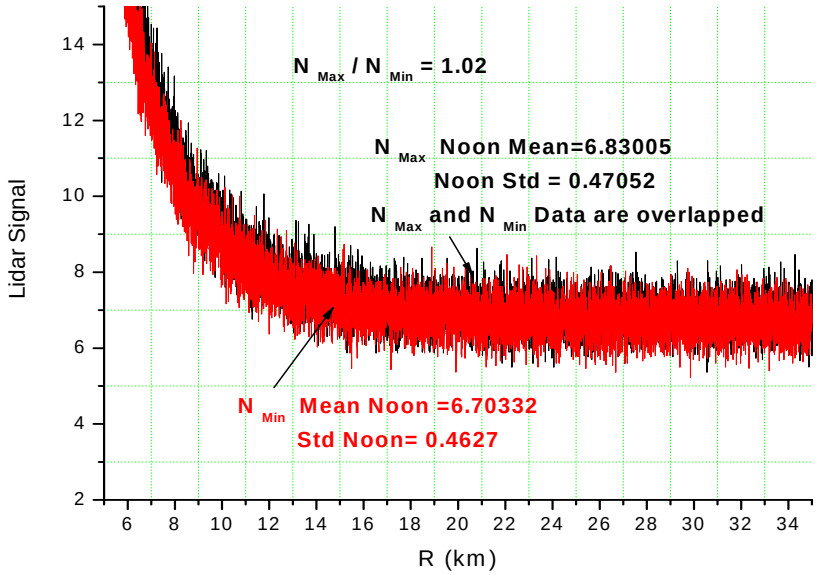

Figure 5.5 Comparison of max P_b (N_{Max}) verses min P_b (N_{Min}) lidar signals at noon (EST) on 07 October 2004: Range 35 km, Lidar signal in linear scale, two signals are overlapped

Fig. 5.6 shows the resulting return signals in the far zone where the sky background signal is the dominant component (20-30 km range) for these times and for both orthogonal polarizations.

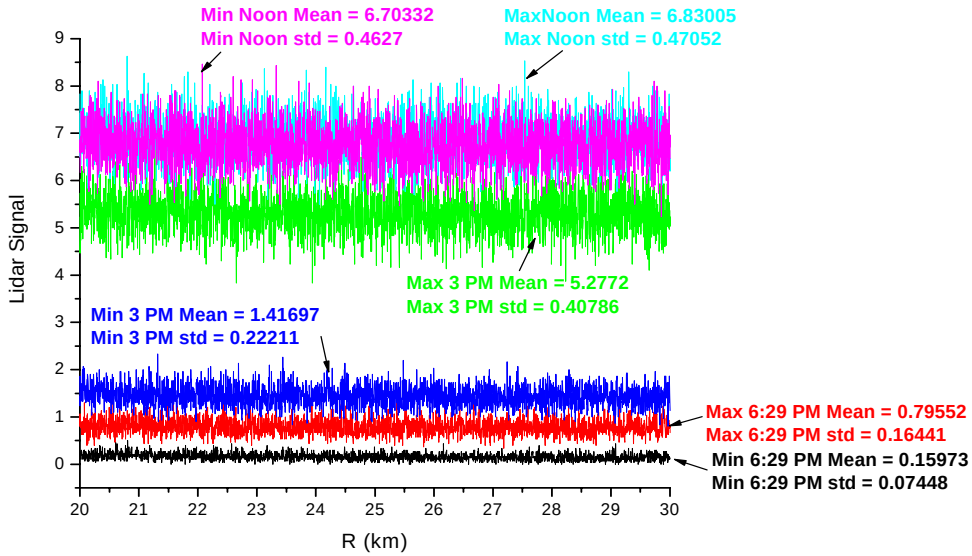

Figure 5.6 Comparison of experimental return signals at 6:29 PM, 3 PM and noon on 07 October 2004, far range of 20- 30 km, both orthogonal cases are shown.

The relative impact on the sky background signal, P_b, of the polarization discrimination scheme is seen to be largest at 6:29 PM, when the lidar solar angle is large (89°), while at noon it is minimal. The detected signal for maximum P_b is much noisier than the detected signal with minimum P_b, except in the noon measurement. This is consistent with the shot noise limit applicable to PMT's where the detected noise amplitude ΔP (standard deviation) is proportional to the square root of the mean detected background signal $\langle P \rangle$ (i.e., $\Delta P \propto \sqrt{\langle P \rangle}$) where P is the detector output, whose mean value is proportional to P_b. This relation is most conveniently expressed in terms of the ratios of the detected signals at the orthogonal polarization states $R = P_b^{\max} / P_b^{\min}$, in which the shot noise

condition is now: $\Delta R = \sqrt{R}$. This relation has been verified in our experiments and the results summarized in Table 5-2

Table 5-2 Comparison of experimental results to verify shot noise operation ($\Delta R = \sqrt{R}$)

Time	$\langle P_{\min} \rangle$	$\Delta P_{\min}$	$\langle P_{\max} \rangle$	$\Delta P_{\min}$	$R = \frac{\langle P_{\max} \rangle}{\langle P_{\min} \rangle}$	$\Delta R = \frac{\Delta P_{\max}}{\Delta P_{\min}}$	$\sqrt{R}$
Noon	6.7	0.46	6.83	0.46	1.2	**1.019**	**1.09**
3:00 PM	1.41	0.22	5.27	0.22	3.72	**1.82**	**1.9**
6:29 PM	0.159	0.074	0.795	0.074	5.2	**2.2**	**2.2**

In assessing the extent to which the polarization discrimination detection scheme can improve the SNR and the operating range, I compare the detected SNR with a polarizer, to that which would be obtained if no polarization filtering was used. When shot noise from background light is large compared to that from the lidar signal backscatter, the SNR improvement can be expressed in terms of an SNR improvement factor (G_{imp}) expressed in terms of maximum and minimum P_b measurements ($P_b^{\max}, P_b^{\min}$) as:

$$G_{imp} = \frac{SNR_{Max}}{SNR_{Unpol}} = \sqrt{\left(\frac{P_b^{\min} + P_b^{\max}}{P_b^{\min}}\right)} = \sqrt{1 + \left(\frac{P_b^{\max}}{P_b^{\min}}\right)} \quad \textbf{(5.1)}$$

To examine how the decreased P_b translates into a SNR improvement, Fig. 5.7 shows the range dependent SNR obtained for both maximum and minimum noise polarization orientations for a representative lidar measurement. The results show that for SNR=10, the range improvement resulting from polarization discrimination resulted

in an increase in lidar operating range from 9.38 km to 12.5km (a 34% improvement). Alternatively, for a given lidar range, say 9 km, the SNR improvement was 250%.

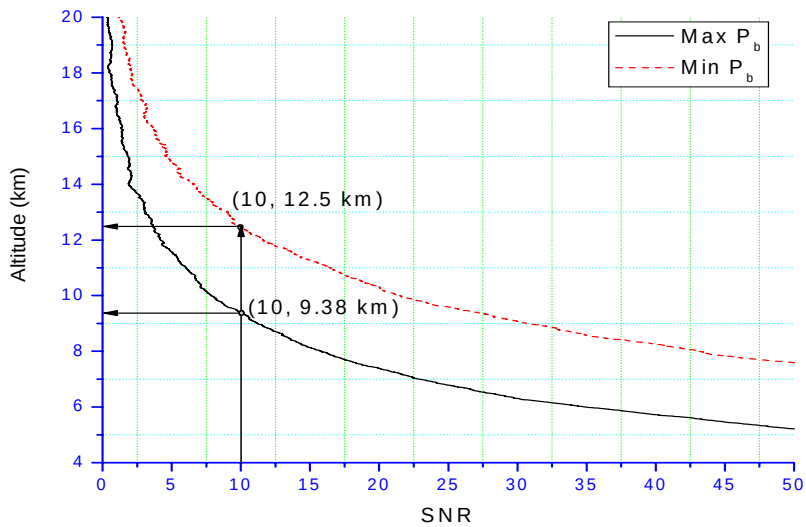

Figure 5.7 Experimental range dependent SNR for maximum and minimum polarization orientations

Another useful way of looking at the effect of SNR improvement is to note that the SNR improves as the square root of the detector's averaging time. Thus a 250% improvement in SNR is equivalent to reducing the required averaging time by a factor of $(1/2.5)^2$.

5.4 SNR Improvement with respect to solar zenith angle

The SNR improvement factor (G_{imp}) is plotted as a function of the local time, Fig. 5.8, and the solar zenith angle, Fig.5.9. Since the solar zenith angle retraces itself as the sun passes through solar noon, it would be expected that the improvement factor

(G_{imp}) would be symmetric before and after the solar noon and depend solely on the solar zenith angle. This symmetry is observed in Figs.5.8 and 5.9 for measurements made on 19 February 2005 and is supported by the relatively small changes in optical depth (AOD) values obtained from a collocated shadow band radiometer, (morning $\tau = 0.08$, afternoon $\tau = 0.11$)

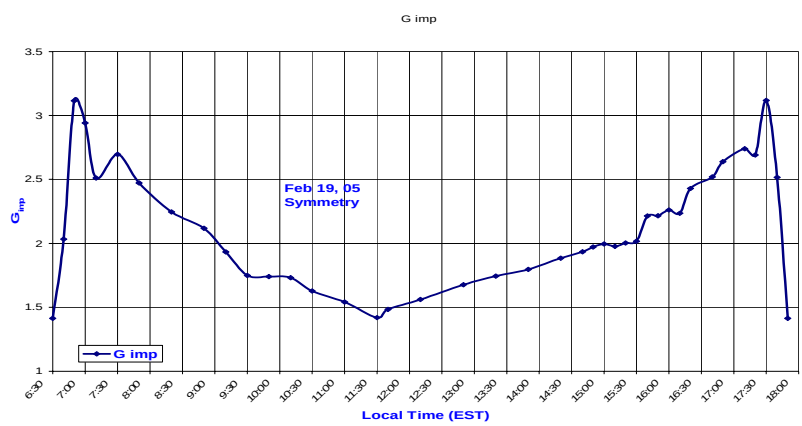

Figure 5.8 G_{imp} in detection wavelength of 532 nm verses local time on 19 February 2005

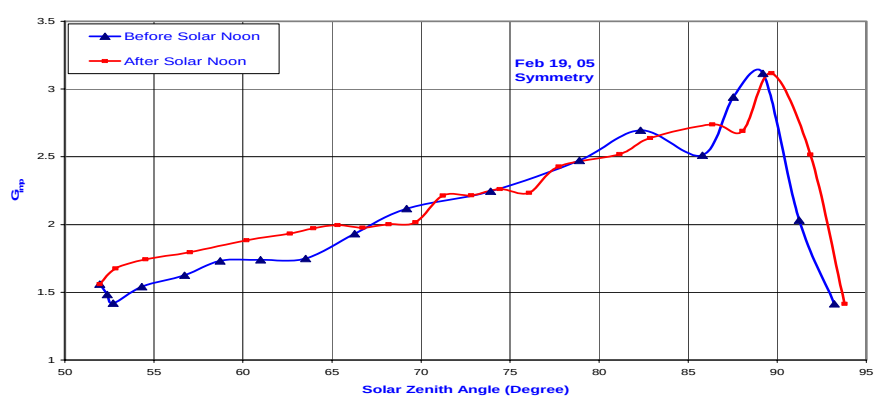

Figure 5.9 G_{imp} in detection wavelength of 532 nm verses solar zenith angle on 19 February 2005

5.5 Effect of Variable Precipitable Water Vapor on SNR

Symmetry was, however, not always observed in our experimental results. Fig. 5.10 shows G_{imp} plotted as a function of the solar zenith angle for 23 February 2005. Small asymmetries were observed. These appear to be related to changes in humidity, which can modify the scattering properties and lead to enhanced multiple scattering effects. The results are supported by the variation in Precipitable water vapor (PWV) shown in Fig. 5.11, obtained from the CCNY Global Positioning System GPS measurements which were processed by the NOAA Forecast Systems Laboratory (FSL) (NOAA Web) for both days.

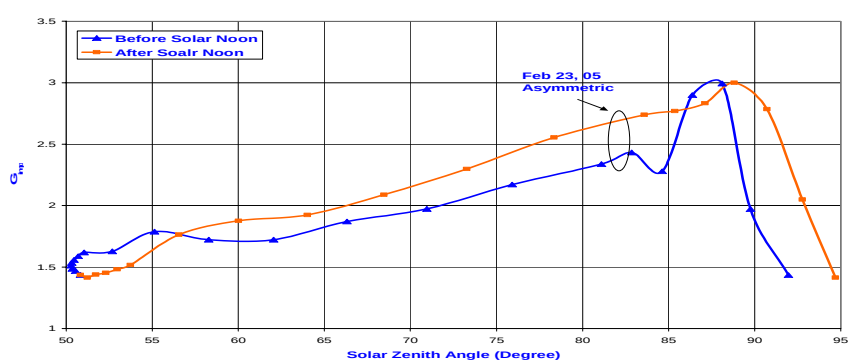

Figure 5.10 Gimp in detection wavelength of 532 nm verses solar zenith angle on 23 February 2005

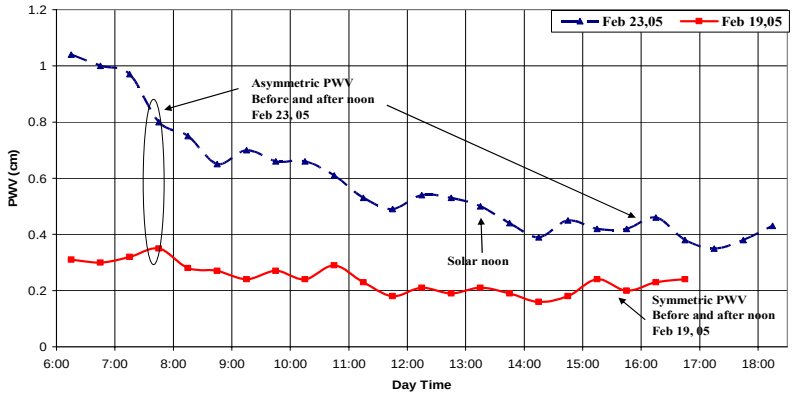

Figure 5.11 PWV (cm) loading verses local time on 19 February 2005 and 23 February 2005

The 23 February the aerosol optical depth measurements from the shadow band radiometer show larger proportional changes (morning $\tau = 0.16$ afternoon $\tau = 0.09$) than those of 19 February, which are consistent with the asymmetry in the PWV, with higher optical depths corresponding to high PWV (and RH%) conditions.

5.6 Discussion and analysis

To compare qualitatively the extent of P_b polarization observed in our experiments with theoretical estimates, we use a single scattering model of the atmosphere, justified by the relatively small optical depths measured by sky radiometry

during the experiments. In this limit, P_b is simply proportional to the diffuse transmission, T, of sunlight through the atmosphere, which takes the form:

$$T_i(\mu;\mu_o) = \frac{\tilde{\omega}}{4(\mu - \mu_o)} P_i^{eff} \left(e^{\frac{-\tau}{\mu}} - e^{\frac{-\tau}{\mu_o}}\right) \quad \textbf{(5.2)}$$

where i =1,2 for parallel (in plane) and perpendicular (out of plane) polarization respectively, μ_0, μ are direction cosines of the solar and viewing angles, τ is the total optical depth, and $\tilde{\omega}$ is the single-scatter albedo. P_1^{eff} and P_2^{eff} are the effective phase functions for the parallel and perpendicular components corresponding to the minimum P_b and maximum P_b. For a two-component atmosphere consisting of a mixture of aerosol and molecules where τ_{mol}, and τ_{aer} are the optical depths for molecular and aerosol components. The effective phase functions are then a weighted combination given by:

$$P_i^{eff} = \frac{\tau_{mol} P_i^{mol} + \tau_{aer} P_i^{aer}}{\tau_{mol} + \tau_{aer}} \quad \textbf{(5.3)}$$

where the total phase functions for the molecular component can be written as:

$$P_{Tot}^{mol} = \frac{3}{4}(1 + \cos^2(\theta_{sc})) \quad \textbf{(5.4)}$$

The molecular optical thickness is obtained from the following empirical formula:

$$\tau_{mol} = C_o\left(\frac{\lambda}{\lambda_o}\right)^{-4}\left[1 + C_1\left(\frac{\lambda}{\lambda_o}\right)^{-2} + C_2\left(\frac{\lambda}{\lambda_o}\right)^{-4}\right] \quad \textbf{(5.5)}$$

where the parameter values are $C_o = 0.09364$, $C_1 = 0.0374$, $C_2 = 0.00142$, and $\lambda_o = 550nm$.(Klein 1970)

The equivalent effective phase functions for the aerosol components depend on the normalized particulate distribution function used, and are approximated (assuming spherical particles) by:

$$P_i^{aer} = S_i(\theta_{sc})\left[\frac{4}{q^2 Q_e}\right] \quad \textbf{(5.6)}$$

$$S_i(\theta_{sc}) = \int S_i^{norm}(r,\theta_{sc})\,\bar{n}(r)\,dr \quad (5.7)$$

Here S_i is the scattering function for each polarization, Q_e is the Mie extinction efficiency, which is a function of the normalized size parameter $q = 2\pi a/\lambda$ where a is the particle radius and λ is the wavelength, $\bar{n}(r)$ is the particle size distribution and S_i^{norm} is the normalized single particle scattering function (for a given polarization) (Hanel 1976; Measures 1984; Liou 2002). We obtain from Eq. (5.2) above, the ratio of the maximum noise $P_b^{\max}$ to the minimum noise $P_b^{\min}$ as:

$$\frac{P_b^{\max}}{P_b^{\min}}(\theta_{sc}) = \frac{T^{\perp}(\mu;\mu_o)}{T^{ll}(\mu;\mu_o)} = \frac{P_2^{eff}}{P_1^{eff}} \quad \textbf{(5.8)}$$

from which, the SNR improvement function G_{imp} can be theoretically estimated using Eq. (5.1). To evaluate this expression, the optical depth of both the molecular and aerosol components as well as the angular dependence of the phase functions should be known.

5.6.1 Symmetric data set

The conditions on 19 February 2005 were quite clear and dry, with rather small optical thickness. We therefore used a fine-mode-dominated aerosol particle size distribution representative of “clear” conditions together with the sky radiometry

measured optical thickness $\tau_{aer} = 0.1$. The use of the fine mode aerosol was justified by a fairly sharp decrease in aerosol optical depth as a function of wavelength resulting in an angstrom coefficient $\gamma = -1.6$. The comparisons between measurements and theoretical results for a single scattering model are given in Fig. 5.12. This shows G_{imp} as a function of the solar zenith angle for a day where PWV variation between morning and afternoon was not significant (recall $\theta_{sc} = \theta_s$ for a vertically pointing lidar). Reasonably good agreement is seen between the theory and observations. Very similar results were obtained on other low PWV variation days (1, 2 February 2005).

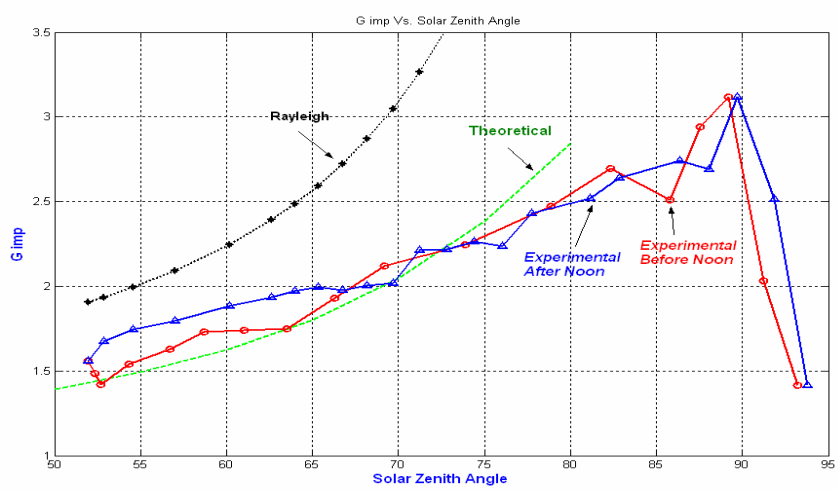

Figure 5.12 Theoretical model agrees with experimental measurements: 19 February 2005
Rayleigh scattering alone is also shown

For comparison, the G_{imp} expected for a completely clear sky due to Rayleigh scattering alone is also shown, where:

$$G_{imp}^{Ray} = \sqrt{1 + \sec^2(\theta_{sc})} \tag{5.9}$$

which is obtained by combining Eq. (5.4) and Eq. (5.8). It is clear that G_{imp} is significantly affected by the impact of even fairly low levels of aerosols.

5.6.2 Asymmetric data set

The asymmetric data of 23 September 2005 can be explained by considering the effects of changes in aerosol particles sizes and refractive index in a moist environment (high RH) because water in the air condenses onto the aerosol. The growth in particle size due to the condensation of water vapor can be described as (Hanel 1976):

$$r(a_w) = r_o \left[1 + \rho \frac{m_w(a_w)}{m_o} \right]^{\frac{1}{3}} \tag{5.10}$$

where the water activity a_w of a soluble aerosol at radius $r(\mu m)$ can be expressed as

$$a_w = RH \exp\left[\frac{2\sigma V_w}{R_w T} \frac{1}{r(a_w)} \right] \tag{5.11}$$

where r_o is the dry particle radius, ρ is the particle density relative to that of water, $m_w(a_w)$ is the mass of condensed water, m_o is the dry particle mass, RH is the relative humidity, σ is the surface tension on the wet surface, V_w is the specific volume of water, R_w is the gas constant for water vapor, and T is the absolute temperature [K]. The refractive index for the wet aerosol particle (n_{eff}), modified by the increased size is approximated by the volume weighted average of the refractive indices of the dry aerosol substance (n_o) and the water (n_w) as :

$$n_{eff} = n_w + (n_o - n_w)\left[\frac{r_o}{r(a_w)}\right]^3 \tag{5.12}$$

From these formulas we note that the magnitude of the particle growth and the change of refractive index with increasing RH depends on the size r_o of the dry aerosol. Also, the magnitude of the particle growth and the change of refractive index with increasing RH (and therefore total PWV) depends on the aerosol type because the water uptake [the ratio $m_w(a_w)/m_o$ in Eq. (5.10)] depends on the aerosol type (Nair and Vohra 1975; Hanel 1976; Hanel and Lehmann 1981; Yan, K. Stamnes et al. 2002). The relationship between the equivalent radius (*r),* and the relative humidity (Halldorsson and Langerhoic) at different values of the equivalent radius $r_{o,}$ in the dry state, have been computed for different models by Hanel (Hanel 1976). In particular, for values of RH (< 99%), the values of the ratio r/ r_o are reasonably independent of r_o, and the smaller the value of the dry state equivalent radius r_o the larger the ratio $r/ r_{o.}$ In Fig. 5.13 I plot the surface level RH measurements from our rooftop weather station (NOAA) for 23 February 2005. The RH for the morning was ~ 70% while by afternoon it had decreased to 30%. Fig. 5.14 shows results obtained from the aerosol hydration model (Hanel 1976) from which it can be seen that the observed change in the RH leads to an estimated change in the radius ratio of 20%. This modification can significantly change the refractive index in accordance with Eq. (5.12) and modify the resulting optical depth.

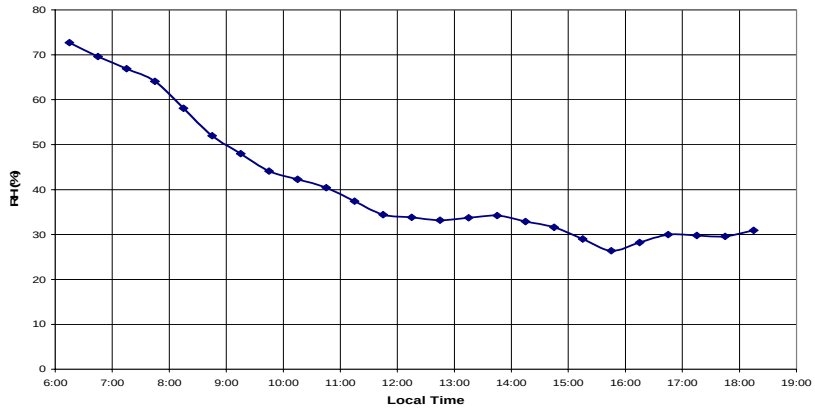

Figure 5.13 Relative humidity, RH, verses local time of New York City on 23 February 2005

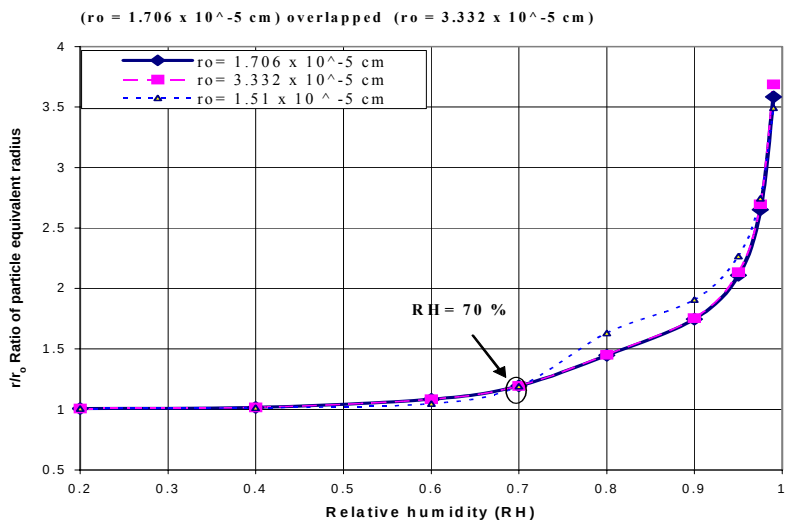

Figure 5.14 The particle equivalent radius ratio r/ r_o verses relative humidity, RH, at different equivalent radius, r_o, in the dry state (RH = 0), and for two aerosol models at 20º C temperature.

To see if the asymmetry observed in the SNR improvement factor can be attributed to the changes in aerosol properties due to hydration, we first modeled the

"dry" aerosol seen in the afternoon as an urban accumulation mode which takes the form of a log normal distribution with parameter values r_m=0.15um, GSD=1.2 and complex refractive index n=1.5-0.2i. The total column number density of the aerosol was then fixed using the afternoon column AOD=0.09 reading obtained from the shadow-band radiometer. The effects of hydration were then modeled by continually sweeping the hydrated aerosol radius and calculating the resultant refractive index from Eq. 5.12 until the resultant AOD matched the measured morning value of $\tau_{aer} = 0.16$. The results are plotted in Fig.5.15 and show that to match the $\tau_{aer} = 0.16$, the final effective radius is given by $r(a_w) = 0.18$um which is consistent with the 20% increase in aerosol radius attributed to the RH changes.

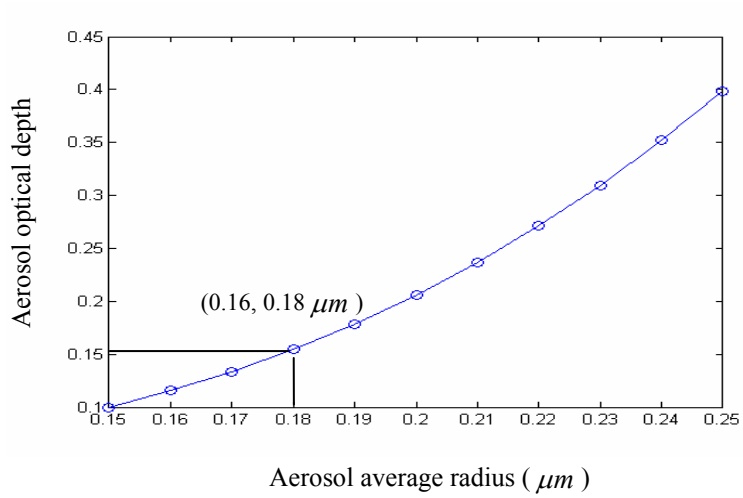

Figure 5.15 Theoretical model: 23 February 2005

Once the microphysical properties were estimated, we again utilize the single scattering analysis to estimate the SNR improvement. Comparisons between

measurements and theoretical results for the single scattering model for these microphysical properties are given in Fig. 5.16. We see that reasonable agreement is obtained between this simplified theoretical approach and the experimental observations.

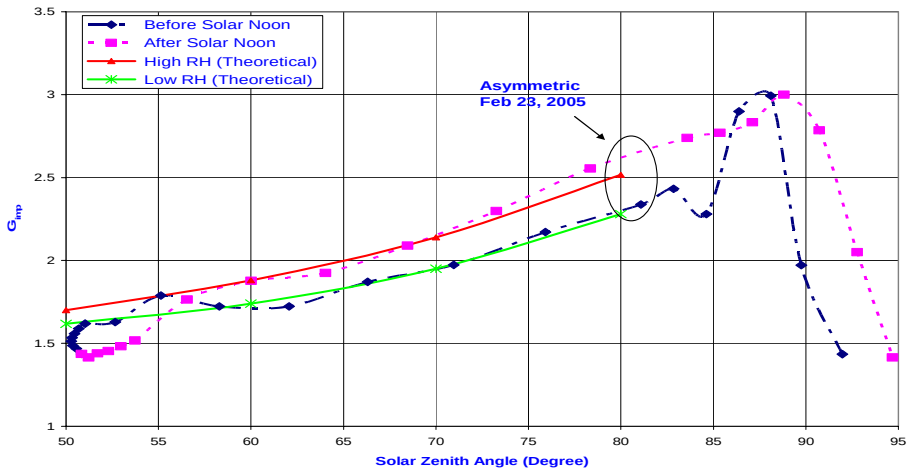

Figure 5.16 Theoretical model agrees with experimental measurements: 23 February 2005

5.7 SNR improvement azimuthally dependence

Within the single scattering theory, the polarization orientation at which the minimum P_b occurs should equal the azimuth angle of the sun (see Fig. 5.1). To validate this result, the polarizer rotation angle was tracked (by rotating the detector analyzer) over several seasons since February 2004 and compared with the azimuth angle calculated using the U.S. Naval Observatory standard solar position calculator

(Applications) (14 April 2005). As expected, the polarizer rotation angle needed to achieve a minimum P_b closely tracks the azimuth angle, Fig. 5.17.

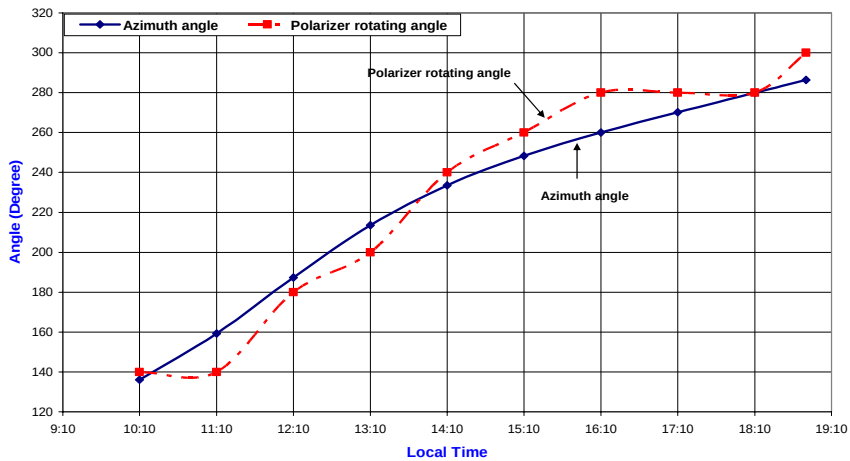

Figure 5.17 Comparison between solar azimuth angle and angle of polarization rotation needed to achieve minimum P_b: 14 April 2005

This relationship is important since it allows us to conceive of an automated approach that makes use of a pre-calculated solar azimuth angle as a function of time and date to automatically rotate and set both the transmitted lidar polarization and the detector polarizer at the orientations needed to minimize P_b. With an appropriate control system, it would then be possible to track the minimum P_b by rotating the detector analyzer and the transmission polarizer simultaneously to maximize the SNR, achieving the same results as would be done manually as described above. Plans are underway to integrate this automated approach into our lidar system. It is also useful to examine the potential impact of the polarization discrimination scheme

on non-vertically pointing lidars. Typically, scanning lidars operating in an elastic or Raman backscatter mode, and are used to scan for particulates or trace constituents in the troposphere. They are of particular interest to air quality monitoring applications where it is often desired to obtain information on spatial distributions of particulates and trace constituents above an urban area. This would include horizontal and near horizontal scans, e.g. along urban canyons etc. Eye safety concerns severely limit acceptable visible lidar pulse energies for these applications, so any schemes to improve received SNR's are important. As seen earlier, for a vertically pointing lidar, the SNR improvement is greatest when the sun elevation is low which restricts the period of large improvement to relatively short times in the early morning and late afternoon. The situation is quite different for a non-vertical scanning lidar. To illustrate, we consider a scanning lidar located at CCNY that is designed to scan the atmosphere above the downtown New York Metropolitan skyline. Since CCNY is approximately 5 km north of the downtown area, the lidar azimuth angle does not need to vary appreciably ($\pm 15^\circ$), and the lidar zenith angle need only vary from $50^\circ \le \theta_{lid} \le 80^\circ$ corresponding to relatively complete coverage through the planetary boundary layer.

From the vertical lidar results, Fig. 5.16, we note that significant SNR improvement (greater than a factor of 2) only occurs for scattering angles θ_{sc} above 70 degrees. This result, when applied to the scanning geometry and making use of the symmetry of the scattering phase function, shows that significant SNR improvement will occur in the interval $70 < \theta_{sc} < 110$. To illustrate the differences between the vertical and

scanning case, we plot in Fig. 5.18, the variation in scattering angle for both the scanning and vertical configurations for June 21, a typically important time of the year for lidar measurements because of the increase in aerosol particulates in summer months. The scattering angle and the complete solar position (zenith and azimuth) needed to obtain it, were again calculated using the solar position calculator(Applications).

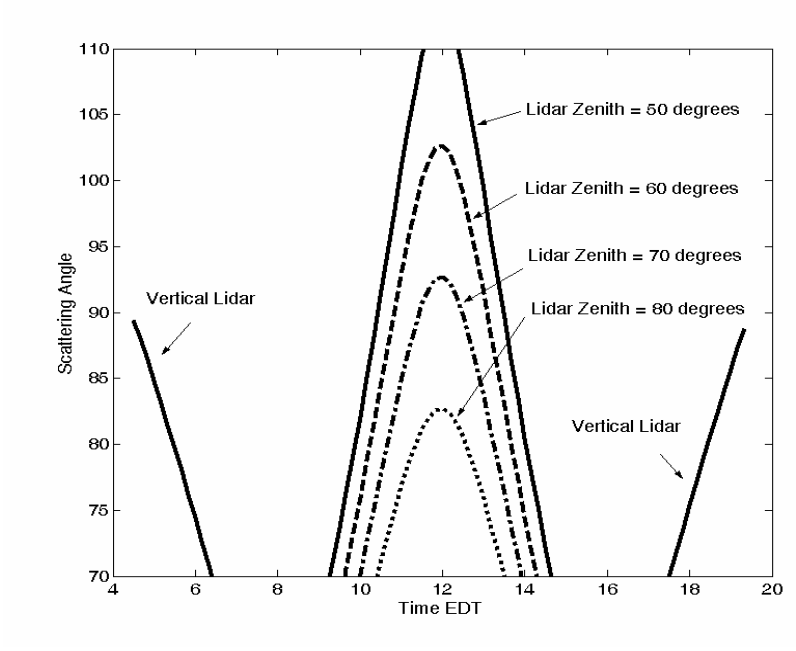

Figure 5.18 The scattering angle θ_{sc} between the solar and lidar directions for the scanning lidar geometry as function of lidar zenith angle and time of day showing periods where SNR improvement can be significant. The vertical lidar result is also plotted to contrast the time periods.

Fig. 5.18 shows that for a good portion of the day (10:00 AM– 2:00 PM), the scattering angle will lie in the range $70 < \theta_{sc} < 110$ permitting significant SNR improvement to be obtained by polarization discrimination. This is in contrast to the situation for a vertically pointing lidar where these improvements occur for very limited times near sunrise and sunset.

We have also examined, in a very preliminary manner, the impact of multiple scattering on the polarization discrimination technique. While it is intuitive that the maximum noise suppression should occur when the receiver polarization is parallel to the scattering plane in the single scattering regime, it is not so clear that this will hold for multiple scattering. However, it can be seen in Figure 5.18 that even for high optical depth (multiple scattering regime $\tau_{aer} = 0.5$), the maximum noise improvement factor calculated using a full polarized radiative transfer code developed at NASA GISS (Chowdhary, B. Cairns et al. 2006) occurs when the differential azimuth angle is zero (i.e. the scattering plane and the observation plane are the same).

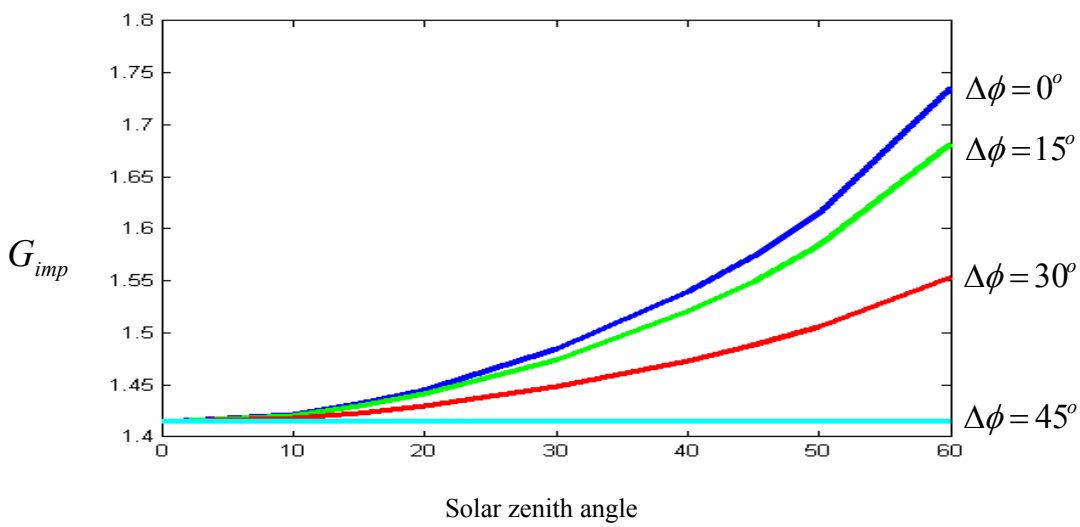

Figure 5.19 Multiple scattering models $\tau_{aer} = 0.5$ showing the minimum noise is parallel to the scattering plane irregardless of OD, $\Delta\phi$ is the azimuth angle difference between the scattering and the polarization planes.

Note also that when there is a 45 degree difference between the planes, only the minimum improvement of $\sqrt{2}$ is obtained since both polarization components are equal and the background noise is effectively unpolarized.

5.8 Multiple Scattering Effects

5.8.1 Magnitude of SNR Improvement Factor

The analysis I performed to obtain the SNR improvement factor G_{imp} was restricted only to the single scattering theory which was applicable for AOD values ~0.1 which matched our experimental situation. However, a complete analysis also requires that the effects of multiple scattering are included in the calculation which requires a radiative transfer code to calculate. In addition, once we consider larger optical depths, the aerosol models themselves change with the AOD. This dynamic modification of the microphysical properties should be taken into account and have been included in the newest models (MODIS) used in the MODIS aerosol retrieval algorithms. The current model is now comprised of a combination of fine and coarse modes based on Aeronet cluster algorithms and the microphysical volume size distribution takes the form may be written as

$$\left[\frac{dV}{d\log r}\right]_{\tau} = V_{\tau}^{1}\exp\left(-\frac{\left[\log\left(r/r_{\tau}^{1}\right)\right]^{2}}{2\left[\sigma_{\tau}^{1}\right]^{2}}\right) + V_{\tau}^{2}\exp\left(-\frac{\left[\log\left(r/r_{\tau}^{2}\right)\right]^{2}}{2\left[\sigma_{\tau}^{2}\right]^{2}}\right) \tag{5.13}$$

where r_{τ} is the mode radius, σ_{τ} is the mode width , V_{τ} is the mode volume and m_{τ} is the mode complex refractive index. In this model, the refractive index is wavelength independent. For the New York area, the aerosol climatology in best described as non absorbing [22] so we use the non absorbing model whose parameterization as function of τ_{550} and is given in Table 5-3 It is clear that multiple scattering will tend to depolarize

the scattering and therefore reduce the improvement factor but it is still useful to quantify the affect over all scattering angles and optical depths which can be realistically obtained.

Table 5-3 Dynamic mode parameters of bimodal aerosol distribution from MODIS aerosol model

Mode	r_τ	σ_τ	V_τ	m_τ
Accum	$\sim 0.0434\tau_{550} + 0.1604$	$0.1529\tau_{550} + 0.3642$	$0.1718\ \tau_{550}^{0.8213}$	$1.42 - (-0.0015\tau_{550}+0.007)i$
Coarse	$0.1411\tau_{550} + 3.3252$	$0.1638\tau_{550} + 0.7595$	$0.0934\ \tau_{550}^{0.6394}$	$1.42 - (-0.0015\tau_{550}+0.007)i$

In the model described above, it should be mentioned that the RH is not used as a parameter but is included to some level implicitly through the increase in mode radius and decrease in the imaginary component of the refractive index with aerosol optical depth which follows the hygroscopic growth process. Therefore, since the goal is to get a reasonable measure of the improvement factor under all reasonable conditions, we will use the above parameterization which implicitly includes all RH conditions.

The results of the improvement factor calculated using a full polarized RT code developed at NASA GISS (Chowdhary, B. Cairns et al. 2006) are presented in Figure 5.20 in the form of a contour plot for different G_{imp} levels. It is clear from the contour plot that the improvement factor G_{imp} for a give scattering angle decreases significantly as the optical depth increases and the range of angles where the improvement is significant decreases with increase AOD.

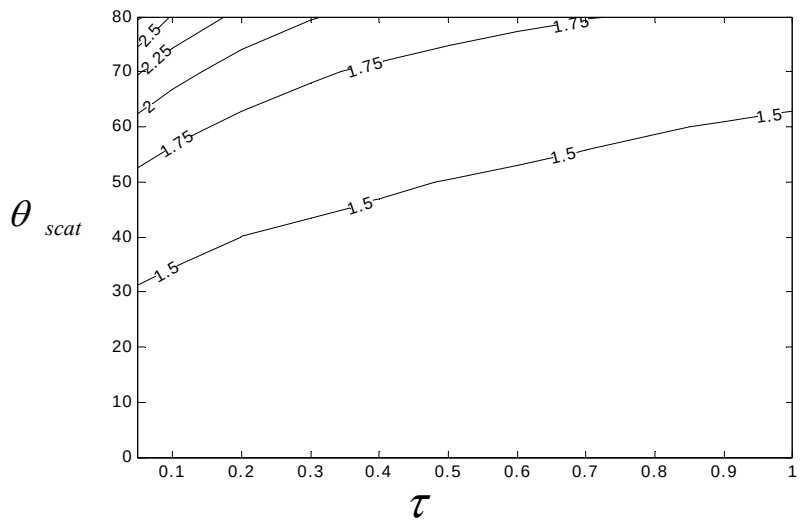

Figure 5.20 Variation of Improvement factor as function of scattering angle and optical depth using radiative transfer theory

5.8.2 Polarization Plane Orientation and SNR Improvement

While the magnitude of the SNR improvement factor is to some extend diminished due to scattering and depolarization, it is still important to confirm if the scattering plane defining the maximum and minimum polarization states has changed. Within the single scattering theory, the polarization orientation at which the minimum P_b occurs should equal the azimuth angle of the sun (see Figure 5.1). To validate this result, the polarizer rotation angle was tracked (by rotating the detector analyzer) over several seasons since February 2004 and compared with the azimuth angle calculated using the U.S. Naval Observatory standard solar position calculator24 (14 April 2005). As expected, the

polarizer rotation angle needed to achieve a minimum P_b closely tracks the azimuth angle as shown in Figure 5.17.

This relationship is important since it allows us to conceive of an automated approach that makes use of a pre-calculated solar azimuth angle as a function of time and date to automatically rotate and set both the transmitted lidar polarization and the detector polarizer at the orientations needed to minimize P_b. With an appropriate control system, it would then be possible to track the minimum P_b by rotating the detector analyzer and the transmission polarizer simultaneously to maximize the SNR, achieving the same results as would be done manually as described above. Plans are underway to integrate this automated approach into our lidar system.

We have also examined the orientation of the scattering plane for the case of multiple scattering. While it is intuitive that the maximum noise suppression should occur when the receiver polarization is parallel to the scattering plane in the single scattering regime, it is not so clear that this will hold for multiple scattering. However, it can be seen in Figure 5.18 that even for high optical depth (multiple scattering regime $\tau_{aer} = 0.5$), the maximum noise improvement factor occurs when the differential azimuth angle is zero (i.e. the scattering plane and the observation plane are the same). Note also that when there is a 45 degree mismatch between the planes, only the minimum improvement of $\sqrt{2}$ is obtained since both polarization components are equal and the background noise is effectively unpolarized.

5.9 Scanning Lidars

The above analysis was performed for the important case of a vertically pointing lidar. However, it is also useful to examine the potential impact of the polarization discrimination scheme on non-vertically pointing lidars. Typically, scanning lidars operating in an elastic or Raman backscatter mode, and are used to scan for particulates or trace constituents in the troposphere. They are of particular interest to air quality monitoring applications where it is often desired to obtain information on spatial distributions of particulates and trace constituents above an urban area This would include horizontal and near horizontal scans, e.g. along urban canyons etc. Eye safety concerns severely limit acceptable visible lidar pulse energies for these applications, so any schemes to improve received SNR's are important. As seen earlier, for a vertically pointing lidar, the SNR improvement is greatest when the sun elevation is low which restricts the period of improvement to relatively short times in the early morning and late afternoon. The situation is quite different for a non-vertical scanning lidar. To illustrate, we consider a scanning lidar located at CCNY that is designed to scan the atmosphere above the downtown New York Metropolitan skyline. Since CCNY is approximately 5 km north of the downtown area, the lidar azimuth angle does not need to vary appreciably ($\pm 15^\circ$) and the lidar zenith angle need only vary from $50^\circ \leq \theta_{lid} \leq 80^\circ$ corresponding to relatively complete coverage through the planetary boundary layer. Under these conditions, we can calculate the resultant scattering angle as a function of the observation time. From the vertical lidar results (see Fig. 5.16), we note that significant SNR

improvement only occurs for scattering angles θ_{scat} above 70 degrees. This result, when applied to the scanning geometry and making use of the symmetry of the scattering phase function, shows that significant SNR improvement will occur in the interval $70 < \Theta_{scat} < 110$. To illustrate the differences between the vertical and scanning case, we plot in Figure 5.19, the variation in scattering angle for both the scanning and vertical configurations for June 21, a typically important time of the year for lidar measurements because of the increase in aerosol particulates in summer months. The scattering angle and the complete solar position (zenith and azimuth) needed to obtain it, were again calculated using the solar position calculator (MODIS). Figure 5.19 shows that for a good portion of the day (10:00 AM– 2:00 PM), the scattering angle will lie in the range $70 < \Theta_{scat} < 110$ permitting significant SNR improvement to be obtained by polarization discrimination. This is in contrast to the situation for a vertically pointing lidar (lidar zenith angle = 0) where these improvements occur for very limited times near sunrise and sunset.

5.10 Conclusions and Summary

SNR improvements can be obtained for lidar backscatter measurements, using a polarization selection/tracking scheme to reduce the sky background component. This approach can significantly increase the far range SNR as compared to un-polarized detection. This is equivalent to improvements in effective lidar range of over 30% for a SNR threshold of 10. The improvement is largest for large scattering angles, which for vertical pointing lidars occur near sunrise/sunset. It was also demonstrated that for non-vertical scanning lidars, the time period under which significant SNR improvement can

occur extends over a significant portion of the midday (10 AM-2 PM) thereby extending the utility of the technique. A theoretical model that simulates the background skylight using the single scattering approximation was developed and showed fairly accurate predictions of the SNR improvement factor. Asymmetric skylight reduction sometimes observed in experimental results is explained by the measured increase in PWV and subsequent modification of aerosol optical depth by dehydration from morning to afternoon. The model was further extended to include multiple scattering effects based on a polarized radiative transfer code. From these calculations, the SNR improvement factor was obtained as a function of both optical depth and scattering angle based on aerosol models which take into account the dynamic variability of the aerosol microphysical parameters as a function of optical depth, It was found that the improvement factor G_{imp} for a give scattering angle decreases significantly as the optical depth increases and the range of angles where the improvement is significant decreases with increase AOD. However, it was also demonstrated that the orientation of the scattering plane defining the minimum noise state does not change in multiple scattering but follows the solar azimuth angle even for high aerosol loading. Therefore, it is quite conceivable to automate this procedure simply by using solar position calculators to orient the polarization axes.

6 LIDAR MEASURMENTS AT CCNY: SUPPORT OF THE NOAA-NEAQS AND NASA-INTEX-NA EXPERIMENTS

6.1 Introduction

Satellite measurements do not provide the vertical information needed to assess aerosol transport mechanisms. To supply this information, multiwavelength lidar measurements are needed to study the vertical structure of aerosol events. In support of NASA – INTEX and NOAA-NEAQS transport experiments; we present lidar retrievals, which identify multiple stratified particulate plumes occurring over NYC on July 21 in support of MODIS imagery. In particular, multiwavelength measurements at CCNY are used to determine the angstrom coefficient of the plumes that unambiguously identifies them as fine mode particulates and not cloud particles. A description of our lidar system capabilities and processing algorithms used to process simultaneous backscatter lidar measurements with Aeronet CIMEL Optical Depth (OD) data is presented and back trajectory analysis is used to confirm the source of the plumes to be from Alaskan wild fires. Finally, surface measurements from in-situ particle counters are presented and show no enhanced PM2.5 loading. This result is supported by lidar measurements, which confirm that nearly all of the aerosol plumes are located above the normal aerosol boundary layer showing that satellite measurements are often incomplete and is not useful to assess surface air quality. In particular, we show that high PM2.5 events are triggered from more local sources such as the Ohio Basin and climatologically conditions which drive the pollution to the surface.

The City College of New York remote sensing laboratory has two multiwavelength lidar systems: a stationary or Lab based lidar system and a mobile lidar system places on a truck. The specifications of these lidar systems are given in Tables (3-1, 3-2)

Unlike radar, where the intervening medium is not that important, the backscatter signal from the lidar depends both on the scattering efficiency of the particulates at the range as well as the extinction from the intervening media and in the case of aerosols, the extinction and backscatter efficiencies are not related unambiguously. Therefore, we expect that some assumptions will be needed. Within the single scattering approximation valid for most atmospheric conditions, the received backscattered lidar signal for an atmosphere consisting of both molecules and aerosol particles is given (Fernauld) as

$$P_r(R,\lambda) = \frac{CP_0(\lambda)\beta_T(R,\lambda)}{R^2} e^{-2\int_0^R [\alpha_T(R,\lambda)]dr} \quad \textbf{(6.1)}$$

where C is the lidar calibration constant which includes all geometrical and optical efficiencies, P_0 is the transmitted pulse power, R is the inline range from the instrument, $\beta_T \equiv \beta_a + \beta_m$ is the total backscattering volume coefficient which includes both the molecular (Rayleigh) and the aerosol (Mie) contribution and $\alpha_T \equiv \alpha_a + \alpha_m$ is the total extinction coefficient. The R^2 term in the denominator accounts for the receiver FOV variations with range.

Under the assumption that the molecular components can be retrieved accurately, the lidar equation provides a single relationship between two independent quantities $\beta_a(R)$ and $\alpha_a(R)$ and in most lidar studies, it is assumed that the aerosol extinction-to-

backscatter ratio $S_a = \dfrac{\alpha_a(R)}{\beta_a(R)}$ is a constant (homogeneous aerosol approximation) which can be estimated either from data tables or estimated from other data. Finally, the calibration constant is hard to determine directly from the physical geometry and instrumentation and therefore an absolute measure of one of the aerosol coefficients along the lidar path is needed.

A solution under the assumed conditions specified can be written (Fernald 1984)

$$\beta_a(R) + \beta_m(R) = \frac{\overline{P}(R)\exp\left[-2(S_m - S_a)\int_R^{R_{\max}} \beta_m(R')dR'\right]}{\left(\dfrac{\overline{P}(R_{\max})}{\beta_T(R_{\max})}\right) + 2S_a \int_R^{R_{\max}} \overline{P}(R')\exp\left[-2(S_m - S_a)\int_{R'}^{R_{\max}} \beta_m(R'')dR''\right]dR'} \tag{6.2}$$

Where $R_{\max}$ is chosen to be the highest point in the lidar range with sufficiently high SNR, and $\overline{P} \equiv PR^2$ is the range corrected backscattered power. Note that this solution fixes the boundary condition at the top of the lidar range and seeks a solution by back integration that is more stable than the corresponding forward solution.

Therefore, given the following data set $\{S_a, \beta_a(R_{\max})\}$, the lidar signal can be inverted to obtain both $\beta_a(R), \alpha_a(R)$. Therefore, an estimate of the data set $\{S_a, \beta_a(R_{\max})\}$ is required and the approach we use to analyze the lidar signals and estimate the optical coefficient error is outlined below.

1. A set of reasonable ratios $C \equiv \dfrac{\beta_a(R_{\max})}{\beta_m(R_{\max})}$ and a set of reasonable aerosol ratios $S_{\min} < S_{aer} < S_{\max}$ are generated. It should be noted that above the boundary

layer, the aerosol concentration decreases substantially and the ratio can usually be bounded by some small number less than one with tighter constraints obtained by increasing the lidar range.

2. The aerosol profiles $\beta_a(R), \alpha_a(R)$ for each set of parameters, is calculated.
3. For each parameter set, the optical depth over the entire lidar range including the molecular contribution above the lidar range

$$\tau_L(S,C) = \int_0^{R_{\max}} (\alpha_a(R') + \alpha_m(R'))\, dR' + \int_{R_{\max}}^{\infty} \alpha_m(R')\, dR' \qquad \textbf{(6.3)}$$

is calculated.

4. The admissible profiles are those that simultaneously satisfy the constraints $C_{\min} \le C \le C_{\max}$ and $\tau_{\min} \le \tau_L \le \tau_{\max}$ estimated from sun-photometry measurements.

5. For each range *R*, a histogram can be constructed for both optical coefficients providing a reasonable estimate of both the aerosol extinction and backscatter profiles for each range.

While this procedure accounts for atmospheric variability, the effects of background and detector noise should also be included into the statistics. It should also be noted that in the body of this paper, only the mean value of the optical data coefficients are displayed. To verify the algorithm against other processing methods for consistency, we compare the Fernald algorithm (Fernald 1984) to an iterative algorithm (Russell P. B., T. J.

Swissler et al. 1979) implemented at Langley and note the agreement between the two methodologies.

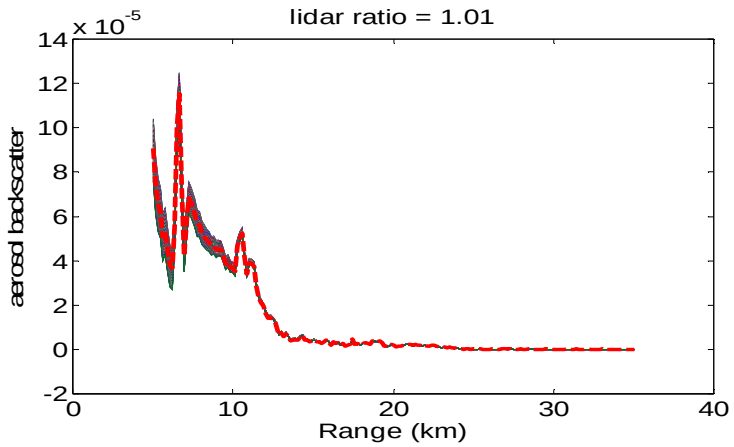

Figure 6.1 Aerosol backscatter processed with CCNY algorithm, S ratio from 10-100 (Langley used 50).

6.2 Results

Much effort has been applied to obtaining larger continuous lidar data blocks to support both the NASA INTEX-NA and NOAA NEAQS experiment which is designed to study the transport of intercontinental chemical and aerosol transport. As an example, we were in position to track smoke plumes over the NYC area from the North West Canadian fires. Below, a MODIS image taken on July 21, 2004 clearly identifies the smoke regions. Below, in Figure 6.2, we see clearly, from MODIS satellite, that smoke plumes are observed over the NYC area but of course, no knowledge of the vertical location or extent of the plume can be determined.

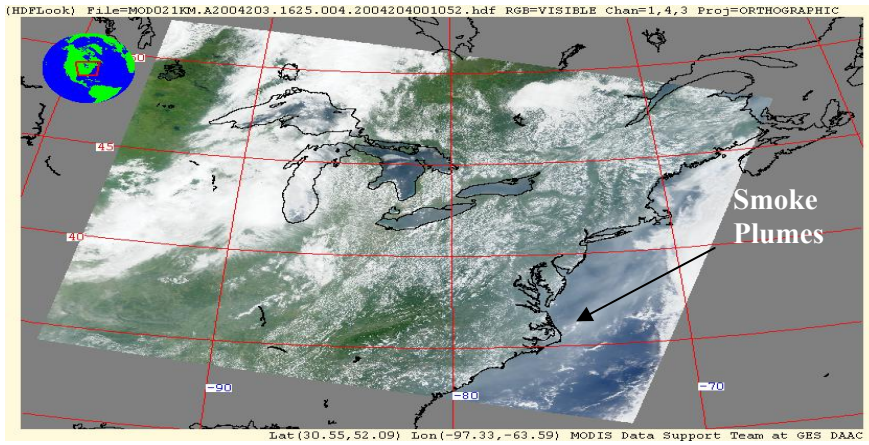

Figure 6.2 Smoke Plumes from MODIS satellite

To obtain vertical information, analysis of a time sequence of lidar data is needed. Given this data, it is possible to apply the Fernald method to obtain the aerosol extinction and backscatter profiles. As mentioned in the introduction, to obtain separately the extinction / backscatter profile, knowledge of the optical depth is needed from other instrumentation. First, for a given point of time, we generate the lidar optical depth measurement and compare to the CIMEL optical depth which is given as 0.4 at 532nm. From this measurement, we estimate, we obtain Sa ~ 80.

To see if this choice is valid over the entire time series, we compare in Figure 6.3, the time series optical depths using Sa~80 resulting in good agreement in general. However, it is clear that the homogeneous model becomes more difficult to justify with a smoke plume and more sophisticated methods may be required.

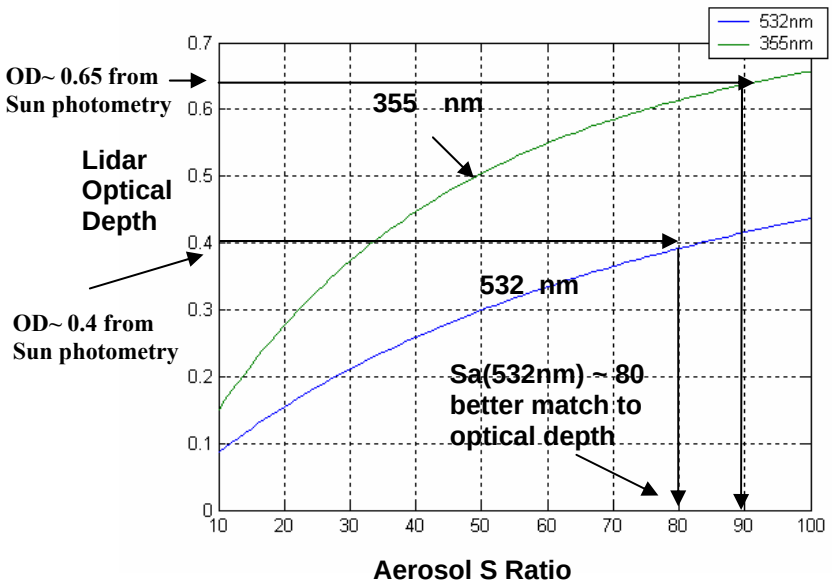

Figure 6.3: July 21 Integrated optical depth (OD), using Fernald method, as function of Sa ratio (OD~0.4 at 532 nm, OD ~0.65 at 355 nm)

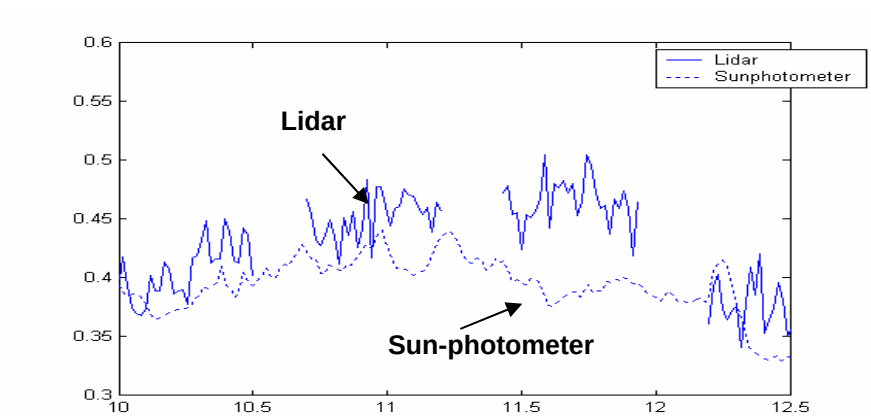

Figure 6.4 Optical depth comparisons to validate choice of extinction to backscatter ratio for 532nm Sa~80.

With the choice of $S_a = 80$, and assuming that the boundary conditions (BC) are determined by having nearly no aerosol contributions at 15 km $\beta_a / \beta_m = .01$, we plot the aerosol extinction coefficient profile in Figure 6.5.

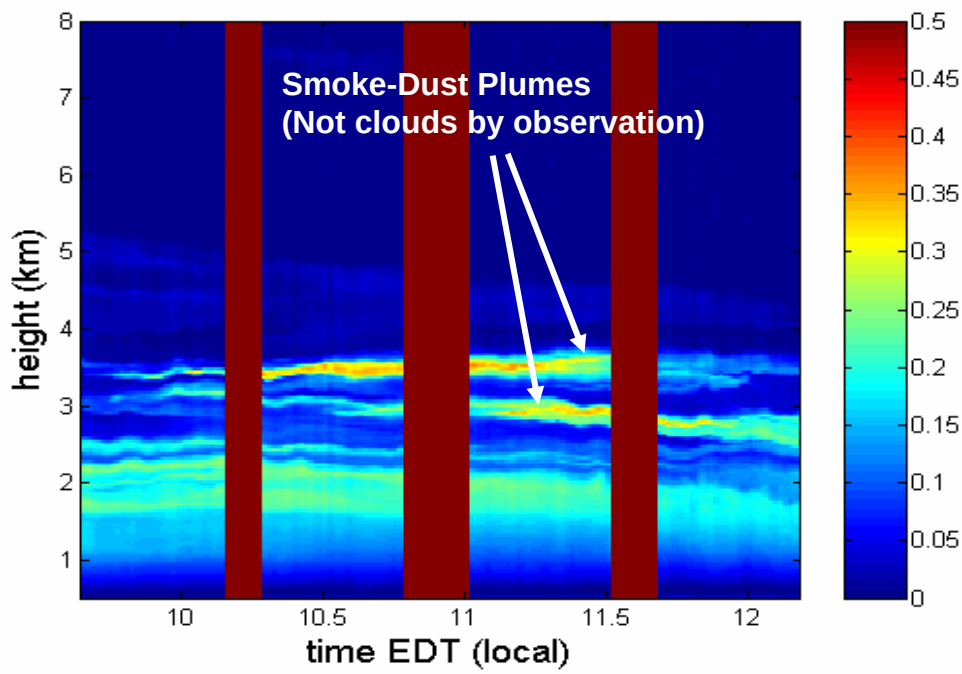

Figure 6.5 Lidar extinction profiles showing existence of plumes

In particular, we note the existence of two very clear and stratified plume layers above the aerosol layer which by visual identification (and the low total extinction) were not clouds. To understand better their formation, we can examine these plumes by looking at their angstrom coefficient which is defined as:

$$\gamma = \frac{\log\left(\beta^{a}_{532} / \beta^{a}_{355}\right)}{\log(355 / 532} \tag{6.4}$$

If the vertical stratified structures were cloud particulates, the angstrom coefficient would be small ~0 independent of the cloud optical depth since clouds are always made up of

large particle modes. On the other hand, smoke plumes can be made of very small absorbing particles which would have a high angstrom coefficient (O'Neill N. T., T. F. Eck et al. 2002). Given two lidar channels each processed independently, it is possible to generate an estimate of the angstrom coefficient profile $\gamma(R)$ which is illustrated in Figure 6.6 for 9:30 AM EST which is the beginning of region 1 and the smoke plumes are weak.

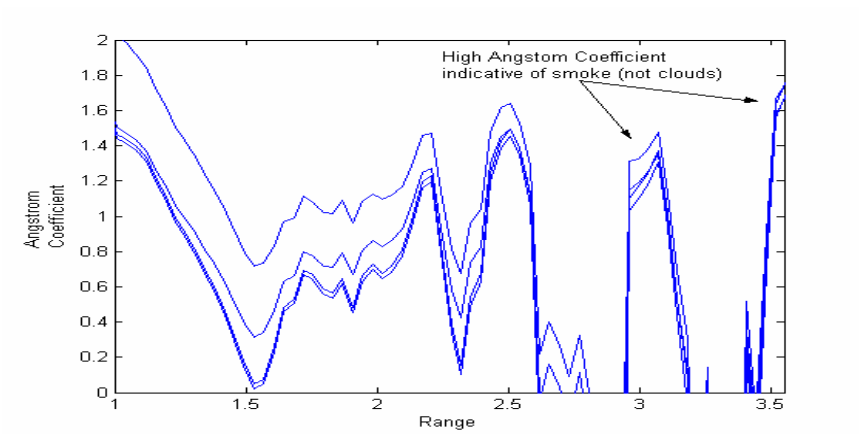

Figure 6.6 Angstrom coefficient using 355-532nm lidar channels for weak plume at 9:30 AM EST.

To see the sensitivity of the angstrom coefficient against uncertainties in the S ratio and far end BC, we plot the angstrom profile for a variety of values resulting in the multiple plots of Figure 6.6. While quantitative changes are evident, they do not significantly affect the far end results. While it is tempting to examine the angstrom coefficient as the plume intensifies, it must be remembered that the 355 channel is already some what noisy and with additional extinction due to the plume, processing of the angstrom coefficient which needs good estimates of the backscatter data at 355 nm becomes more suspect, especially since it is in the denominator. In Figure 6.7, we plot the angstrom coefficient

profile but we see more regions where the coefficient goes below zero (due to our taking the log of negative

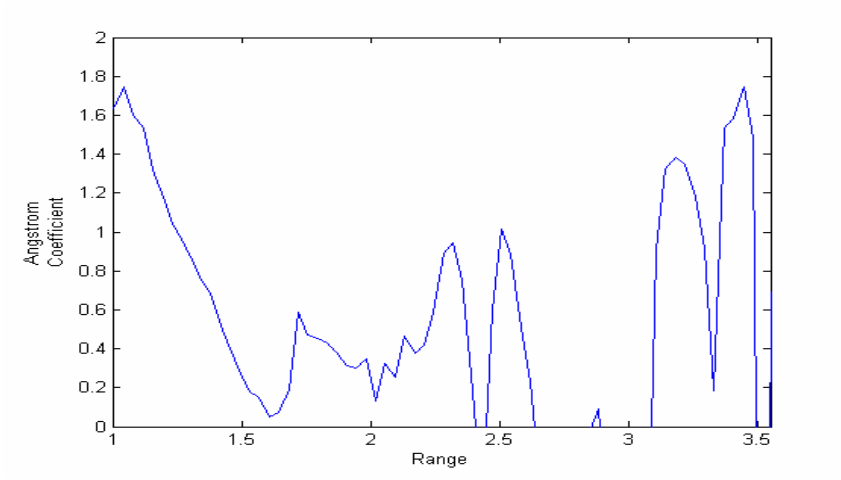

Figure 6.7 Angstrom coefficient using 355-532nm lidar channels for weak plume at 10:10 AM EST.

This problem gets more systemic as the plume depth increases and therefore, becomes more suspect with larger patches of unphysical values but the general observation of a large angstrom coefficient for the smoke plumes is still correct.

To validate that cloud signals differ markedly from the smoke plumes, Figure 6.8 shows the aerosol backscatter profile for July 22 which was a cloudy day.

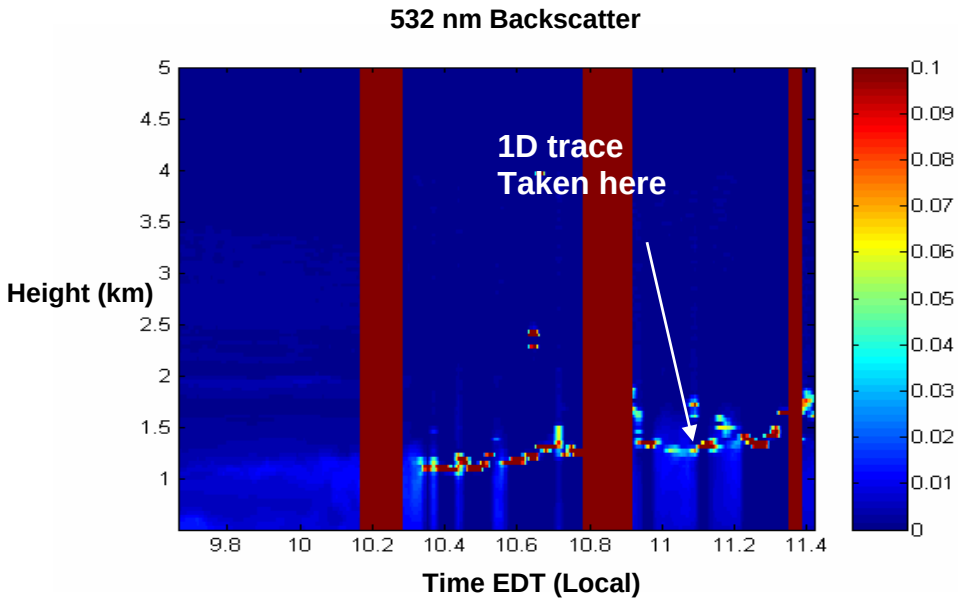

Figure 6.8 July 22 Backscatter of thin hydrated clouds

In Figure 7.9, the backscatter profile for 10 AM at 532 and 355 nm are superimposed. The results are consistent with backscatter obtained from thin hydrated clouds, showing essentially the same backscatter signal at 532 nm and 355nm which results in an angstrom coefficient (γ) of zero. This is in contrast to non-zero value for plumes with individually different backscatter coefficients at different wavelength (O'Neill N. T., T. F. Eck et al. 2002), i.e.,

$$log\ (\beta_{532}/\ \beta_{355}) \neq 0 \qquad (6.5)$$

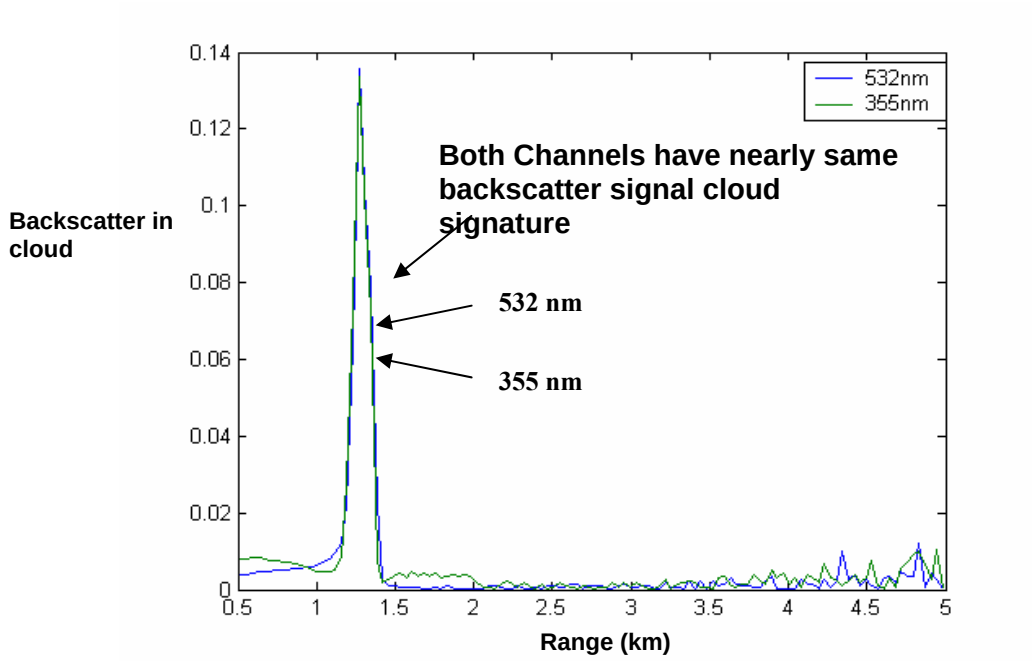

Figure 6.9 July 22 Backscatter of thin hydrated clouds.
Angstrom coefficient can see clouds from smoke.

6.3 HYSPLIT Back-Trajectories

Finally, by locating the plume vertical heights, back trajectory analysis using NOAA-HYSPLIT algorithm can be used to examine the source regions. As seen in Figure 6.10, the back-trajectories are consistent with transport from the northwest Canadian forest fires. Figure 6.11 shows Rainfall Hysplit Back-trajectories for the two vertical plumes at 1500 UTC (11EST) detected by our lidars. The very low amounts of precipitation observed along the trajectories; help explain the long life of the plume.

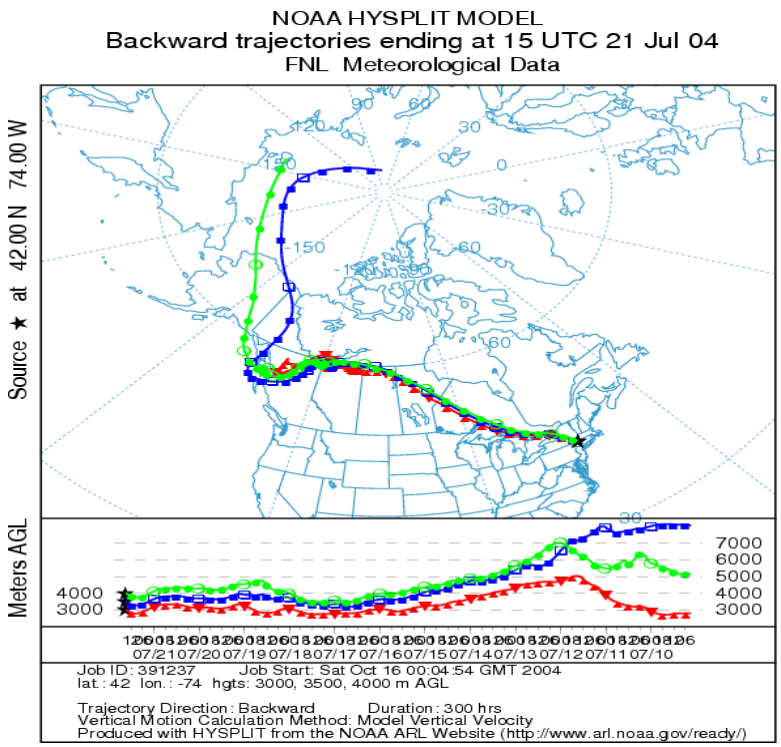

Figure 6.10 Hysplit Back-trajectories showing source of smoke plumes

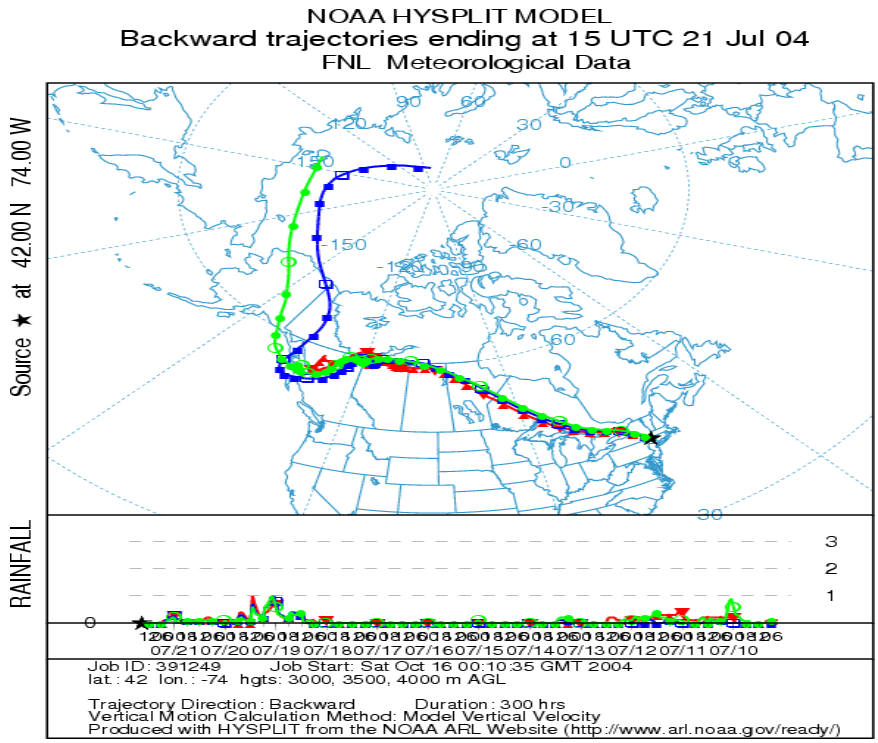

Figure 6.11 Rainfall Hysplit Back-trajectories for two vertical plumes at 1500 UTC (11EST) seen by our lidar. Track to northwest Canadian fires

6.4 PM2.5 Surface Measurements.

While intercontinental transport of smoke plumes were observed in the NYC area, it is reasonable to examine how these plumes affected the surface air quality. To do this, we plot in Figure 6.12, the surface concentrations of coincident PM2.5 and CO measurements obtained from the Department of Environmental Conservation's New York State air quality network (Webpage).

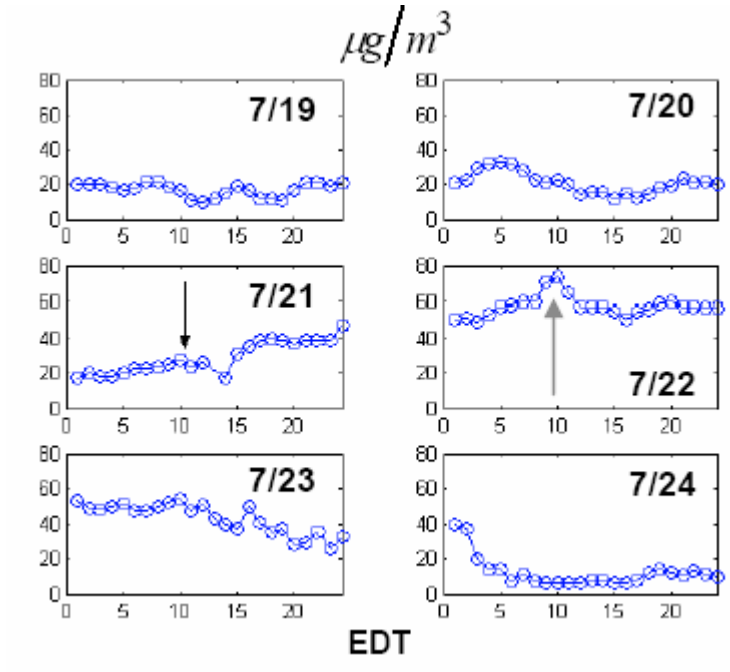

Figure 6.12 PM2.5, Corresponding surface air quality measurements- NYS DEC, NYC

From the PM2.5 concentration time profiles exhibited above, it is clear that the surface air quality was not significantly affected by the smoke plumes. In particular, we see that for the July 21 event, PM2.5 concentrations were comparatively low. However, we note a significant increase in PM2.5 concentration going into the next day. This trend is also clearly exhibited in the CO concentrations as well which are illustrated in Figure 6.13.

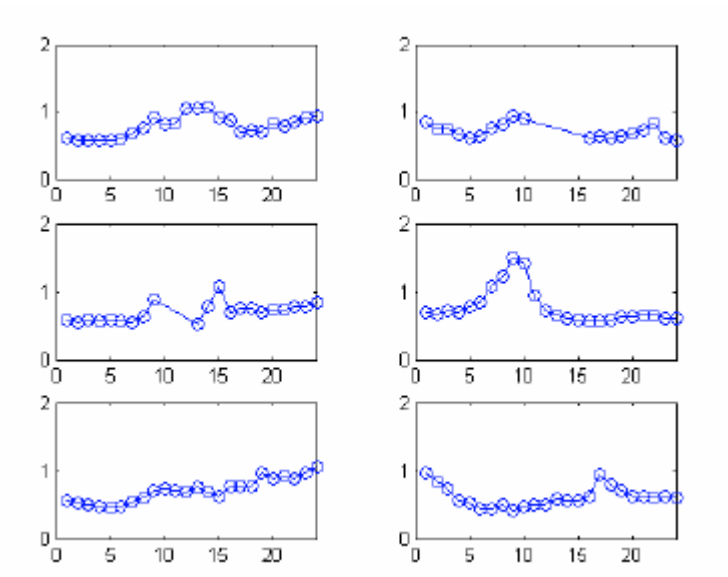

Figure 6.13 CO, Corresponding surface air quality measurements- NYS DEC, NYC

These results suggest that the plumes did not have any significant affect on the surface air quality. This is clearly seen in the lidar aerosol extinction profile in Figure 6.5 where both the smoke plumes and the PBL were significantly aloft. On the other hand, we see that for July 22, the situation is different. In particular, the presence of low altitude clouds is seen to push the pollution to lower a surface altitude which is consistent with the results of the DEC surface air quality samplers. Back-trajectory analysis of this event shows that the sources are most likely originating in the Ohio Basin.

6.5 Conclusions

Lidar measurements have been shown to support satellite measurements that identified transcontinental smoke plumes. In particular, by examining the angstrom coefficient calculated from the 355 – 532nm channels in the plume region, clouds, which possess small angstrom coefficients near 0, were ruled out. In addition, results of Back-trajectory analyses are consistent with satellite observations. Unfortunately, an inherent weakness in looking at plumes with significant optical depth is the increased noise due to attenuation on the 355 channel making the results more suspect. Methods to improve the results including more temporal averaging are underway. However, we also show through the combined use of surface level air quality samplers and lidar measurements that the presence of smoke plumes is not a significant driver for local surface air quality. In particular, we show that high PM2.5 events are triggered from more local sources such as the Ohio Basin and climatological conditions which drive the pollution to the surface

7 CONCLUSIONS

I have examined potential improvements in lidar SNR using two approaches:

1. Receiver design and geometric form factor considerations
2. Elastic backscatter lidar systems using polarization selection to minimize detected skylight noise

Both approaches showed potential for significant improvement.

3. I also presented the results of lidar field measurements which show the lidar system to be effective for aerosol measurements in the troposphere. These results also showed how it is possible to differentiate (dry) smoke plumes from clouds. In addition, I coupled these results with the back-trajectory calculations in support of the NOAA-NEAQS and NASA-INTEX-NA experiments

Lidar Field of View (FOV) Considerations

Improvements in lidar SNR by optimization of the design of the lidar receiver were examined by a series of simulations. This part of the research concentrated on biaxial lidar systems, where overlap between laser beam and receiver field of view (FOV) is an important aspect of noise considerations. The first optimized design evolved is a wedge shaped aperture. While this design has the virtue of greatly reducing background light, it is difficult to implement practically, requiring both changes in area and position with lidar range. A second more practical approach, which preserves some of the advantages of the wedge design, was also evolved. This uses a smaller area circular aperture

optimally located in the image plane for desired ranges. Simulated numerical results for a biaxial lidar have shown that the best receiver parameters selection is one using a small circular aperture (field stop) with a small telescope focal length f, to ensure the minimum FOV that accepts all return signals over the entire lidar range while at the same time minimizing detected BGP and hence maximizing lidar SNR and attainable lidar ranges. The improvement in lidar SNR was up to 18 %.

Lidar SNR Improvements Using Polarization Discrimination Technique

SNR improvements obtained from lidar backscatter measurements, using a polarization selection–tracking scheme to reduce the sky background component, was found to significantly increase the far-range SNR as compared to unpolarized detection. This is equivalent to improvements in the effective lidar range of over 30% for a SNR threshold of 10. The improvement, for vertical pointing lidars, is largest for large scattering angles and therefore occurs near sunrise and/or sunset. It was also demonstrated that when the technique is applied to lidars scanning below 50° zenith angle, the time period under which significant SNR improvement can occur extends over a significant portion of the midday (10 a.m.–2 p.m.) thereby extending the utility of the technique. A theoretical model that simulates the background skylight within the single-scattering approximation was developed and showed fairly accurate predictions of the SNR improvement factor. Asymmetric skylight reduction was sometimes observed in experimental results and is explained by the measured increase in PWV and subsequent modification of aerosol optical depth by dehydration from morning to afternoon. Finally, since the polarization axis follows the solar azimuth angle even for high aerosol loading as demonstrated using

radiative transfer simulations, it is quite conceivable to automate this procedure simply by using solar position calculators to orient the polarization axes. In all previous discussions, clear sky conditions were assumed. The impact of clouds in the lidar field of view is more complex. From intuitive considerations, it can be conjectured that on a partially sunny day, a lidar viewing directly scattered sunlight from a cloud, with large single-scattering components, will see a significant polarized light component in the detected radiation. Under those circumstances, which apply primarily to the scanning lidar orientations, polarization discrimination should improve the SNR.

CCNY Lidars in Support of NASA and NOAA Satellites Measurements

Lidar measurements have been shown to support satellite measurements that identified transcontinental smoke plumes. In particular, by examining the angstrom coefficient calculated from the 355 – 532nm channels in the plume region, clouds, which possess small angstrom coefficients near 0, were ruled out. In addition, results of Back-trajectory analyses are consistent with satellite observations. Unfortunately, an inherent weakness in looking at plumes with significant optical depth is the increased noise due to attenuation on the 355 channel making the results more suspect. Methods to improve the results including more temporal averaging are underway. However, we also show through the combined use of surface level air quality samplers and lidar measurements that the presence of smoke plumes is not a significant driver for local surface air quality. In particular, we show that high PM2.5 events are triggered from more local sources such as the Ohio Basin and climatological conditions which drive the pollution to the surface

Recommended Future Work

- The contribution of Raman lidar in remote sensing technology in general and specially for cloud measurements and evaluating the lidar ratio are appropriate future goals.
- Simultaneous measurements by CALIPSO and NOAA ground based lidars are useful topics for improving the accuracy of data analysis, simulations and algorithms in both systems.
- Polarization studies were based on the assumption of “clear sky conditions”. However, in other circumstances, such as partially cloudy sky, the cloud reflectance is largely polarized, and so may permit use of the technique. More detailed examinations are needed to quantify the effects of multiple scattering by both dry and hydrated aerosols as well as clouds.

Y. Hassebo Publications, Conference Proceedings and Presentations

---

2006

1. Y. Hassebo, B. Gross, M. Oo, F. Moshary, and S. Ahmed, Polarization discrimination technique to maximize lidar signal to noise ratio for daylight operations, **App. Opt**. Vol. **45**, No. 22, pp 5521-5531, (2006)

2. S. Ahmed, Y. Hassebo, B. Gross, M. Oo, F. Moshary, Examination of Reductions in Detected Skylight Background Signal Attainable in Elastic Backscatter Lidar Systems Using Polarization Selection, in 23rd International Laser Radar Conference (**ILRC**), **Japan**, pp 187-190, July 2006 (2006)

3. S. Ahmed, Y. Hassebo, B. Gross, M. Oo, F. Moshary "Potential and range of application of elastic backscatter lidar systems using polarization selection to minimize detected skylight noise" in Lidar Technologies, Techniques, and Measurements for Atmospheric Remote Sensing, Proc. 6367, in press, **SPIE**, (2006)

4. Y. Hassebo, B. Gross, F. Moshary, and S. Ahmed, Lidar signal-to-noise ratio improvements by receiver aperture design analysis and optimization techniques, in Junior Scientist Conference 2006, Vienna University of Technology, **Vienna**, Austria, April 2006 (2006)

5. Y. Hassebo, B. Gross, F. Moshary, and S. Ahmed, Lidar signal-to-noise ratio improvements by aperture design analysis and receiver telescope selection, in Proc. of the Fourth Annual NOAA-CREST Symposium, Mayaguez, **Puerto Rico**, Oral Presentation, February 2006 (2006)

2005

6. Y. Hassebo, Y. Zhao, B. Gross, F. Moshary, S. Ahmed, Multi-wavelength Lidar Measurements at the City College of New York in Support of the NOAA-NEAQS and NASA-INTEX-NA Experiments, Remote Sensing of Atmospheric Aerosols Workshop, pp 16 – 23, **IEEE**, (2005)

7. Y. Hassebo, B. Gross, F. Moshary, Y. Zhao, S. Ahmed, Polarization discrimination technique to maximize lidar signal to noise ratio, in Lidar Technologies, Techniques, and Measurements for Atmospheric Remote Sensing, Oral Presentation, Proc. 5888, pp 93-101, **SPIE**, (2005)

8. Y. Hassebo, B. Gross, M. Oo, F. Moshary, and S. Ahmed, Impact on lidar system parameters of polarization selection / tracking scheme to reduce daylight noise, in

Lidar Technologies, Techniques, and Measurements for Atmospheric Remote Sensing, Proc. 5984, pp 53-64, **SPIE**, (2005)

9. Y. Hassebo, B. Gross, F. Moshary, and S. Ahmed, Impact on Lidar Signal to NOISE Ratio of Polarization technique, Einstein in the City Conference, City College of City University of **New York**, USA, April 2005 (2005)

2004

10. Y. Hassebo, Ravil Agishev, F. Moshary, S. Ahmed, Optimization of biaxial Raman lidar receivers to the overlap factor effect, in the Third Annual NOAA CREST Symposium Hampton **Virginia**, USA, Oral Presentation, April 2004, (2004)

11. Y. Hassebo, presentation on, Novel Aperture Techniques in Raman Lidar, in NOAA CREST Day Conference, CCNY, **New York**, USA, Oral Presentation,March 2004, (2004)

12. Y. Hassebo, Y. Zhao, B. Gross, F. Moshary, S. Ahmed "Multi-wavelength Lidar Measurements at the City College of New York in Support of the NOAA-NEAQS and NASA-INTEX-NA Experiments-I", in Proc. of 5th International Conference On Laser Applications (**ICLA 5**), Cairo, **Egypt**, Oral Presentation, January 2004, (2004)

References

Agishev, R. R. and a. A. Comeron (2002). "Spatial filtering efficiency of monostatic biaxial lidar: analysis and applications." App. Opt. **41**: 7516-7521.

Ahmed, S., Y. Hassebo, et al. (2006). Examination of Reductions in Detected Skylight Background Signal Attainable in Elastic Backscatter Lidar Systems Using Polarization Selection. 23rd International Laser Radar Conference (ILRC), Nara, Japan.

Ahmed, S. A., Yasser Y. Hassebo, et al. (2006). Potential and range of application of elastic backscatter lidar systems using polarization selection to minimize detected skylight noise. SPIE, Sweden.

Allen, R. J. and a. C. M. R. Platt (1977). "Lidar for multiple backscattering and depolarization observations." Appl. Opt. **16**: 3193–3199.

Ansmann, A., U. Wanginger, M. Riebesell, C. Weitkamp amd W. Michaelis (1992). "Independent measurement of extinction and backscatter profiles in cirrus clouds by using a combined Raman elastic-backscatter lidar." Appl. Opt. **33**: 7113-7131.

Applications, U. S. N. O. A. "U.S. Naval Observatory Astronomical Applications, http: //aa.usno.navy.mil/data/docs/AltAz.html."

Barber, P., and C.Yeh (1975). "Scattering of Electromagnetic Waves by Arbitrarily Shaped Dielectric Bodies." Appl. Opt **14**: 2864-2872.

Barnaba F and a. G. Gobbi (2001). "Lidar estimation of tropospheric aerosol extinction, surface area and volume: Maritime and desert-dust cases. ." J. Geophys. Res. **106** (D3): 3005-3018.

Bills, R., C. Gardner, and C. She (1991). "Narrowband lidar technique for sodium temprature and Doppler wind observations of the upper atmosphere." Opt. Eng. **30**(a): 13-21.

Bruscaglioni, P., G. Zaccanti, et al. (1983). "An approximate procedure to isolate single scattering contribution to lidar returns from fogs." Int. J. Remote Sensing **4**: 399–417.

Carswell, A. I. (1990). Lidar remote sensing of atmospheric aerosols. Proc. SPIE.

Charleon, R. J. E. (1995). Aeroeol forcing of climate. New York, J. Wllay.

Charlson, R. J., J. Langner, et al. (1991). "Perturbation of the northern hemisphere radiative balance by backscattering from anthropogenic sulfate aerosols." Tellus **43AB**: 152-163.

Charlson, R. J., S. E. Schwartz, et al. (1992). " Climate forcing by anthropogenic aerosols." Science **255**: 423-430.

Chowdhary, J., B. Cairns, et al. (2006). "The contribution of the water leaving radiances to multiangle, multispectral polarimetric observations over the open ocean: Bio-optical model results for Case I waters". ." Appl. Opt **45**: 5542–5567.

Deirmendjian, D. (1969). Electromagnetic Scattering on Spherical Polydispersion. New York.

Douglass L. R., M.R. Schoeberl, et al. (2000). "A composite view of ozone evolution in the 1995-1996 northern winter polar vortex developed from airborne lidar and satellite observations." J. Geophys Res. **106** (D9): 9879-9895.

Fernald, F., B. Herman, et al. (1972). "Determination of aerosol height distributions by lidar." J. Appl. Meteorol. **11**: 482–489.

Fernald, F. G. (1984). "Analysis of Atmospheric Lidar Observations: Some Comments." Appl. Opt. **23**(5): 652–653.

Gobbi, G. P. (1998). "Polarization lidar returns from aerosols and thin clouds: a framework for the analysis." Appl. Opt. **37**: 5505-5508.

Gardner, C. S., et al. (1993). " Simultaneous observations of sporadic E, Na, Fe, and Ca+ layers at Urbana, Illinois: Three case studies." J. Geophys. Res. **98**: 16,865-16,873.

Gelbwachs, A. (1994). "Iron Boltzmann factor lidar: proposed new remote sensing technique for atmospheric temperature." Appl. Opt(33): 7151-7156.

Granier, C., J. P. Jegou, et al. (1989). "Iron atoms and metallic species in the Earth's upper atmosphere." Geophys. Res. Lett. **16**: 243-246.

Halldorsson and a. J. Langerhoic (1978). "Geometrical form factors for the lidar function." Appl. Opt **17**: 240-244.

Hamamatsu: http://www.hamamatsu.com

Hanel, G. (1976). The properties of atmospheric aerosol particles as functions of the relative humidity at thermodynamic equilibrium with the surrounding moist air. Advances in Geophysics, New York Academic.

Hanel, G. and a. M. Lehmann (1981). "Equilibrium size of aerosol particles and relative humidity: new experimental data from various aerosol types and their treatment for cloud physics application." Contr. Atmos. Phys. **54**: 57-71.

Hansen, J. and a. L. Travis (1974). "Light Scattering in Planetary Atmospheres." Space Science Reviews **16**: 527-610

Hassebo, Y., R. Agishev, et al. (2004). Optimization of Biaxial Raman Lidar receivers to the overlap factor effect" Third NOAA CREST Symposium, Hampton, VA USA.

Hassebo, Y. Y., B. Gross, et al. (2005). Polarization discrimination technique to maximize LIDAR signal-to-noise ratio. Polarization Science and Remote Sensing II, SPIE

Hassebo, Y. Y., B. Gross, et al. (2006). "Polarization discrimination technique to maximize LIDAR signal-to-noise ratio for daylight operations." App. Opt. **45**: 5521-5531.

Hassebo, Y. Y., Barry M. Gross, et al. (2005). Impact on lidar system parameters of polarization selection / tracking scheme to reduce daylight noise. Lidar Technologies, Techniques, and Measurements for Atmospheric Remote Sensing, SPIE.

Hassebo, Y. Y., Y. Zhao, et al. (2005). Multi-wavelength Lidar Measurements at the City College of New York in Support of the NOAA-NEAQS and NASA-INTEX-NA Experiments IEEE.

Heaps, W. S., J. Burris (1996). "Airborne Raman lidar." Appl. Opt **35**: 7128-7137.

Heaps, W. S., J. Burris, and J. French (1997). "Lidar technique for remote measurement of temperature by use for a vibrational-rotational Raman spectroscopy." Appl. Opt **36**: 9402-9405.

Ishimaru, A. (1997). A. Ishimaru, Wave Propagation and Scattering in Random Media. . Piscataway, NJ, IEEE Press.

Jegou, J., M.Chanin, et al. (1980). "Lidar measurements of atmospheric lithium." Geophys. Res. Lett. **7**: 995-998.

Jones, F. E. (1949). "Radar as an aid to the study of the atmosphere " Royal Aeronautical Society **53**: 433-448.

José M. Bioucas Dias, J. M. N. Leitão, et al. (2004). "Reconstruction of Backscatter and Extinction Coefficients in Lidar: A Stochastic Filtering Approach." IEEE TRANSACTIONS ON GEOSCIENCE AND REMOTE SENSING **42**(2).

Junge, C. (1955). "The size distribution and aging of natural aerosol as determined from electrical and optical data on the atmpsphere." J. Meteorol **12**: 13-25.

Klein, M. V. (1970). Optics. New York, Wiley.

Klett, J. D. (1981). "Stable analytical inversion solution for processing lidar returns." Appl. Opt. **20**: 211–220.

Klett, J. D. (1985). "Lidar inversion with variable backscatter/extinction ratios

" Appl. Opt. **24**: 1638–1985.

Kokkinos, D. S. and S. A. Ahmed (1989). Atmospheric depolarization of lidar backscatter signals. Lasers '88' International Conference, Lake Tahoe, NV, STS Press.

Kovalev, V. and H. Moosmüller (1994). "Distortion of particulate extinction profiles measured with lidar in a two-component atmosphere." Appl. Opt. **33**: 6499–6507.

Kovalev, V. and W. Eichinger (2004). Elastic Lidar, Theory, Practice, and Analysis Mathods. New Jersey, Wiley.

Kunz, G. and a. G. Leeuw (1993). "Inversion of lidar signals with the slope method." Appl. Opt. **32**(18): 3249–3256.

Kuze, H., H. Kinjo, et al. (1998). "Field-of-view dependence of lidar signals by use of Newtonian and Cassegrainian telescopes." Appl. Opt. **37**(15).

Lentz, W. J., Alfred W. Cooper, et al. (1994). Improved Klett lidar inversion techniques. Atmospheric Propagation and Remote Sensing III, Proceedings of SPIE.

Liou, K. N. (2002). An Introduction to Atmospheric Radiation. California, Academic Press.

McClung, F. J. a. R. W. H. (1962). "Giant Optical Pulsations from Ruby." Appl. Phys. **33**: 828-829.

Measures, R. M. (1984). Laser Remote Sensing: Fundamentals and Applications. New York, Wiley.

Measures. R. M., a. G. P. (1972). "A Study of Tunable Laser Techniques for Remote Mapping of Specific Gaseous Constituents of the Atmosphere." Opto-electronics **4**: 141-153.

Middleton, W. E. K., and A.F.Spilhaus (1953). Meteorological Instruments. Toronto, , University of Toronto Press.

Mie, G. (1908). Annalen der Physik **24**: 376-445.

MODIS http://modis.gsfc.nasa.gov/data/atbd/atbd_mod02.pdf

MODIS Collection 5 Aerosol Retrieval Theoretical Basis Document.

Nair, P. V. N. and a. K. G. Vohra (1975). "Growth of aqueous sulfuric acid droplets as function of relative humidity." J. Aerosol Sci. **6**: 265–271.

NOAA-CREST " http://earth.engr.ccny.cuny.edu/noaa/wc/DailyData/."

NOAA " http://www.fsl.noaa.gov."

O'Neill N. T., T. F. Eck, et al. (2002). "Optical properties of boreal forest fire smoke derived from Sun photometry." JGR **107**(D11 AAC 6): 1-21.

Petri, K., A. Salik, and J. Coony (1982). "Variable-Wavelength Solar-Blind Raman Lidar for Remote Measurement of Atmospheric Water-Vapor Concentration and Temprature." Appl. Opt **21**: 1212-1218.

Platt, C. M. R. (1977). "Lidar observation of a mixed-phase altostratus cloud." J. Appl. Meteorol. **16**: 339–345.

Platt, C. M. R. (1981). Transmission and reflectivity of ice clouds by active probing. Clouds, Their Formation, Optical Properties, and Effects, San Diego, Calif., Academic.

Renaut, J., C. Pourny, and R. Capitini (1980). "Daytime Raman-LidarMeasurements of Water Vapor." Optics Letters **5**: 233-235.

Rodriguez, M., R. Sauerbrey, et al. (2002). "Optics Letters." 27(772).

Roy, N., G. Roy, et al. (2004). "Measurement of the azimuthal dependence of cross-polarized lidar returns and its relation to optical depth." Appl. Opt. **43**: 2777-2785.

Russell P. B., T. J. Swissler, et al. (1979). " Methodology for error analysis and simulation of lidar aerosol measurements." Appl. Opt. **18**.

Sasano, Y., E. Browell, et al. (1985). "Error caused by using a constant extinction/backscattering ratio in the lidar solution." Appl. Opt. **24**: 3929–3932.

Sasano, Y., H. Shimizu, et al. (1979). "Geometrical form factor in the laser radar equation: an experimental determination." Appl. Opt **18**: 3908-3910.

Sassen, H. Z. K., et al. (1992). "Simulated polarization diversity lidar returns from water and precipitating mixed phase clouds." Appl. Opt. **31**: 2914-2923.

Sassen, K. (1974). "Depolarization of laser light backscattered by artificial clouds." J. Appl. Meterol. **13**: 923–933.

Sassen, K. (1979). "Scattering of polarized laser light by water droplet, mixed-phase and ice crystal clouds. 2. Angular depolarization and multiple scatter behavior." J. Atmos. Sci **36**: 852–861.

Sassen, K. (1994). "Advanced in polarization diversity lidar for cloud remote sensing." Proc. IEEE **82**: 1907-1914.

Sassen, K. and a. R. L. Petrilla (1986). "Lidar depolarization from multiple scattering in marine stratus clouds." Appl. Opt. **25**: 1450– 1459.

Schotland, R. M. (1966). Some Obsevation of the vertical Profile of Water Vapor by a Laser Optical Radar. 4th Symposium on Remote Sensing of the Environment Univ. of Michigan.

Schotland, R. M., K. Sassen, et al. (1971). "Observations by lidar of linear depolarization ratios by hydrometeors." J. Appl. Meteorol **10**: 1011–1017.

She, C. and a. J. Yu (1994). "Simultaneous three-frequency Na lidar measurements of radial wind and temperature in the mesopause region." Geophys. Res. Lett. **21**: 1771-1774.

Spinhirne, J. D. (1991). Lidar aerosol and cloud backscatter at 0.53, 1.06 and 1.54 µm. presented at the 29th Aerospace Sciences Meeting, Reno, NV.

Spinhirne, J. D. (1993). "Micro pulse lidar." IEEE TRANSACTIONS ON GEOSCIENCE AND REMOTE SENSING **31**: 48-54.

Stein, B., C. Wedekind, et al. (1999). "Optical classification, existence temperatures, and coexistence of different polar stratospheric cloud types." J. Geophys. Res. **104** (D19): 23983–23993.

Stelmaszczyk, K., M. Dell'Aglio, et al. (2005). "Analytical function for lidar geometrical compression form-factor calculations." Appl. Opt. **44**(7).

Stephens, G. L. (1994). Remote Sensing of the Lower Atmosphere: An Introduction. New York, Oxford Univ. Press.

Takashi Fhjii and T. Fukuchi (2005). Laser Remote Sensing, Taylor and Francis Group

Velotta, R., B. Bartoli, et al. (1998). "Analysis of the receiver response in lidar measurements." Appl. Opt. **37**: 6999–7007.

Webpage. "http://www.dec.state.ny.us/website/dardata/airmon/sitepage2.htm."

Welton, E., J. Campble, et al. (2001). First Annual Report: The Micro-pulse Lidar Woldwide Observational Network, Project Report

Wiscombe, W. J. (1980). "Improved Mie Scattering Algorithms." Appl. Opt **19**: 1505.

Wöste, L., C. Wedekind, et al. (1997). "Laser und Optoelektronik " **29 (5)**(51).

Yan, B., K. Stamnes, et al. (2002). "Pitfalls in atmospheric correction of ocean colorimagery: how should aerosol optical propertiesbe computed?" Appl. Opt. **41**: 412-423.

Zuev V., V. Burlakov, et al. (1998). "Ten Years (1986-1995) of lidar observations of temporal and vertical structure of stratospheric aerosol over Siberia." J. Aerosol Sci. **29** 1179-1187.

VITA

P. O. Box: 521319
Flushing, NY 11352, USA
Cell phone: (917) 403-0512
E-mail: Ya_Hass@yahoo.com

Yasser Hassebo

Objective

To obtain a teaching / research and development position in the field of mathematics/ engineering

Qualifications Summary

- Four years of **teaching** experience with excellent record in **CCNY** and **BMCC**
- Outstanding analytical, problem solving and innovation skills, demonstrated by a great academic record and strengthened during five years of **research**
- Efficient leadership and teamwork skills developed throughout research projects and work experience including **mentoring, advising and recruiting** students
- Strong communication skills, gained from teaching, preparing technical reports, publications and conferences **presentations**
- Five years of hands-on and **programming** experience in college laboratories

Education

May 01, 2007 — **Ph.D., Electrical Engineering**, The City University of New York, USA
- **Thesis:** "Lidar Signal to Noise Ratio Improvements: Considerations and Techniques"

October 01, 2006 — **Master of Philosophy (M.Phil), Engineering**, The City University of New York, USA

June, 2002 — **M.E., Electrical Engineering,** The City College of the City University of New York
- **Project:** "Routing and Wavelength Assignment in Optical Core **Network**"
- Awarded the School of Engineering Graduate Citation. **GPA:** 3.8/4.0

June, 1995 — **B.S. in Electrical Engineering**, Menofia University, Egypt
- **Thesis:** " Closed Loop Industrial Robotics Control System Using Microprocessor and PLC"
- Distinction with Honor. **Rank:** 4th

Honors and Awards

- Honor: *Who's Who Among American Teachers*, top 5% teachers in **USA,** (05, 06, 07)
- **NOAA-CREST** Fellowship: 2005 – Present
- The City **University** of New York Scholarship: 2002 – 2004
- Awarded the school of engineering graduate citation: 2002
- Menoufia University, graduated with honor: 1995

Teaching Experience

Fall 2006, Present

Sept. 06 - Present

Instructor, LaGuardia CC, CUNY, Math/Engineering Department, USA
- Technical Math for Engineering [MAT 242]
- Precalculus [MAT 200]
- Math in Modern World [MAT 107]
- Mathematics For Health Science [MAT 106]
- Intermediate Algebra and Trigonometry (Math in Action II) [MAT 096]
- Basic Arithmetic and Algebra (Math in Action I) [MAT 095]

Yasser Hassebo
(917) 403-0512
Page 2 0f 4

Teaching Experience (Cont.)

Fall, 02 – Spring 06

Lecturer, BMCC. CUNY. **Mathematics** Department, **USA**

- Mathematics For Health Science [MAT 104]
- Intermediate Algebra and Trigonometry [MAT 056]
- Basic Arithmetic and Algebra [MAT 012]

Fall, 02 – Spring, 06

Lecturer, CCNY, CUNY. **Electrical Engineering/ Engineering** Departments, **USA**

- Introduction to Feedback Control Systems [EE 371]
- Control Laboratory [EE 426]
- Digital Clock Design [ENGR 102]

Spring, 2003
Spring, 2004

Teaching Assistant, CCNY, CUNY. Electrical Engineering Department, **USA**

- Switching Systems [EE 210]
- Introduction to Feedback Systems [EE 371]

Comments of Students

His notes are very neat and organized. He explains everything clearly & welcomes questions. He is fair with the class. He doesn't like to just stand there and lecture; he likes to have a discussion. He is very helpful and always available during his office hours. Very nice Professor would take him in any course. 100% Recommended! If all Professors were a like him, City College would be much better

Research Experience

Aug 02 – Present

Research Assistant, The City College of the City University of New York, **USA**

- Developed backscatter light detection and ranging (**LIDAR**) systems
- Generated and implemented a new LIDAR technique improving LIDAR's signal to noise ratio up to **300%** and the corresponding LIDAR's range to **134%**
- Programming: LIDAR simulations using MATLAB and LABVIEW, Microsoft office, grading program and web design (FrontPage)
- Studied and built "Vehicles silhouette classification using **Neural Networks**"
- Analyzed and studied "Traffic modeling for audio, games, and emails (**TCP/IP network**) using Ethereal"

Jan. 02 – June 02

- **Master Project Thesis:** "*Routing and Wavelength Assignment in Optical Core **Network***", CCNY, NY, **USA**

- Simulating core network topology was for 35 optical router nodes
- Simulation included: traffic generation, shortest path first algorithm (Dijkstera's Algorithm), RWA algorithm, calculating and plotting packet delay and blocking statistics.
- This work implemented using MATLAB programming

Sept. 94–June 95

Senior Undergraduate Thesis: *" Closed Loop Industrial Robotics Control System Using Microprocessor and PLC"*, Menofia University, **Egypt**

- Designed and implemented a three dimensions movement robotic arm.
- Performance was achieved using feedback control, Microprocessor and PLC

Yasser Hassebo
(917) 403-0512

Publications and Presentations (Selected)

- Y. Hassebo, B. Gross, M. Oo, F. Moshary, and S. Ahmed, Polarization discrimination technique to maximize LIDAR signal to noise ratio for daylight operations, Appl. Opt. Vol. 45, No. 22, pp 5521-5531, (2006)
- S. Ahmed, Y. Hassebo, B. Gross, M. Oo, F. Moshary, Examination of Reductions in Detected Skylight Background Signal Attainable in Elastic Backscatter Lidar Systems Using Polarization Selection, in 23rd International Laser Radar Conference (ILRC), Japan, in press, July 2006 (2006)
- Y. Hassebo, B. Gross, F. Moshary, and S. Ahmed, Lidar signal-to-noise ratio improvements by receiver aperture design analysis and optimization techniques, in Junior Scientist Conference 2006, Vienna University of Technology, Vienna, Austria, April 2006 (2006)
- Y. Hassebo, B. Gross, F. Moshary, and S. Ahmed, Lidar signal-to-noise ratio improvements by aperture design analysis and receiver telescope selection, in Proc. of the Fourth Annual NOAA-CREST Symposium, Mayaguez, Puerto Rico, Oral Presentations, February 2006 (2006)
- Y. Hassebo, Y. Zhao, B. Gross, F. Moshary, S. Ahmed, Multi-wavelength Lidar Measurements at the City College of New York in Support of the NOAA-NEAQS and NASA-INTEX-NA Experiments, Remote Sensing of Atmospheric Aerosols Workshop, pp 16 – 23, IEEE, (2005)
- Y. Hassebo, B. Gross, F. Moshary, Y. Zhao, S. Ahmed, Polarization discrimination technique to maximize lidar signal to noise ratio, in Lidar Technologies, Techniques, and Measurements for Atmospheric Remote Sensing, Oral Presentations, Proc. 5888, pp 93-101, SPIE, (2005)
- Y. Hassebo, B. Gross, M. Oo, F. Moshary, and S. Ahmed, Impact on lidar system parameters of polarization selection / tracking scheme to reduce daylight noise, in Lidar Technologies, Techniques, and Measurements for Atmospheric Remote Sensing, Proc. 5984, pp 53-64, SPIE, (2005)
- Y. Hassebo, B. Gross, F. Moshary, and S. Ahmed, Impact on LIDAR Signal to NOISE Ratio of Polarization technique, Einstein in the City Conference, City College of City University of New York, USA, April 2005 (2005)
- Y. Hassebo, Ravil Agishev, F. Moshary, S. Ahmed, Optimization of Biaxial Raman Lidar receivers to the overlap factor effect, in the Third Annual NOAA CREST Symposium Hampton Virginia, USA, April 2004 (2004)
- Y. Hassebo, presentation on, Novel Aperture Techniques in RAMAN Lidar, in NOAA CREST Day Conference, CCNY, New York, USA, March 2004 (2004)

Work Experience

Nov 99 – May 2000 **Projects Manager**, BIN HAM Technical Group, Al Ain**,** Abu Dhabi, **U.A.E.**

- Projects budget: $ 0.75 million
- Finished electrical, aluminum and carpentry constructions for forty villas and a school with the UAE ministry of buildings slandered approval
- Led a team of an engineer, three inspectors, and more than forty employees and coordinated their efforts
- Placed, followed and analyzed the work plan and the projects schedule
- Communicated, in official meetings, with the UAE government engineers
- Chosen and concluded contracts with subcontractors and main contractors

Yasser Hassebo
(917) 403-0512

Nov 98 – Nov 99 **Projects Engineer**, Modern Electro Mech. Engineering Co., Al Ain, **U.A.E.**

- Completed electrical constructions for 130 villas (Ministry of buildings, UAE).
- Project budget: $1.7 million.
- Supervised more than fifty employees as well as two engineers
- Developed electrical drawings and design based on the standard specifications
- Dealt with government and consulting engineers concerning technical problems
- Implemented a computer program to follow the work plan and schedule
- Arranged and calculated the monthly payments

May 97 – Sept. 98 **Electrical Engineer,** Technical Enterprises Co., Al Ain, Abu Dhabi, **U.A.E.**

- Gained a strong knowledge in import and export works
- Arranged estimations and offers with our five main agencies in Europe for our clients in UAE including the government departments
- Studied and analyzed the scientific specifications for electrical equipments
- Dealt with governmental and professional engineers to solve technical problems

Future Work

Teaching

- Establish a freshmen laboratory class for **digital clock design** which can count seconds, minutes and hours including PM and AM with alarm
- Create an environmental science program
- Assign students' projects in math and robotics
- Build up a control system laboratory
- Generate a **student group** of innovations and sciences

Research

- Develop a research center of remote sensing
- Recruiting students to join **NOAA**, and create a new students association
- Build and operate remote sensing technology such as Differential Optical Absorption Spectrometer (**DOAS**) to detect and measure different pollutants in any metropolitan area

Interests and Activities

- Member, Optical Society of America (OSA) since 2002
- Member, International Society for Optical Engineering (SPIE) since 2002
- Member, Institute of Electrical and Electronics Engineers (IEEE) since 1996
- Member, Egyptian Syndicate of Engineers(Ansmann), since 1995
- Member, American Association of Mathematics, since 2007
- Member, Engineering, Advisory, Curriculum, and Search committees, Lag./ CUNY

Status

- US Citizen

References

- Available upon request